
Numerical Methods in Non-Perturbative Quantum Field Theory

Paul Tognarelli



University of
Nottingham

UK | CHINA | MALAYSIA

Thesis submitted to the University of Nottingham
for the degree of Doctor of Philosophy

October 2017

Supervisors: Dr. Paul Saffin
Prof. Edmund Copeland

Examiners: Dr. Eugere Lim (King's College)
Dr. Anastasios Avgoustidis (University of Nottingham)

Submitted: 29 October 2017

*“Quantum physics is a lot like jazz:
you don’t know what you
might have until you observe it.”*

– **Mark Nightingale**
(no, the other one)

Abstract

This thesis applies techniques of non-perturbative quantum field theory for solving both bosonic and fermionic systems dynamically on a lattice.

The methods are first implemented in a bosonic system to examine the quantum decay of a scalar field oscillon in $2 + 1D$. These configurations are a class of very long-lived, quasi-periodic, non-topological soliton. Classically, they last much longer than the natural timescales in the system, but gradually emit energy to eventually decay. Taking the oscillon to be the inhomogeneous, (quantum) mean field of a self-interacting scalar field enables an examination of the changes to the classical evolution in the presence of quantum fluctuations. The evolution is implemented through applying the Hartree approximation to the quantum dynamics. A statistical ensemble of fields replaces the quantum mode functions to calculate the quantum correlators in the dynamics. This offers the possibility for a reduction in the computational resources required to numerically evolve the system. The application of this method in determining the oscillon lifetimes, though, provides only a negligible gain in computational efficiency: likely due to the lack of any space or time averaging in measuring the lifetimes, and the low dimensionality.

Evolving a Gaussian parameter-space of initial conditions enables comparing the classical and quantum evolution. The quantum fluctuations significantly reduce the lifetime compared to the classical case. Examining the evolution in the oscillatory frequency demonstrates the decay in the quantum system occurs gradually. This markedly contrasts the classical evolution where the oscillon fre-

quency has been demonstrated to evolve to a critical frequency when the structure abruptly collapses. Despite the distinctly different evolution and lifetime, a similar range of the Gaussian initial conditions in both cases generates oscillons. This indicates the classical effects dominate the early evolution, and the quantum fluctuations most significantly alter the later decay.

The methods are next implemented in a fermionic system to examine “tunnelling of the 3rd kind”. This phenomenon is examined in the case where a uniform magnetic field propagates through a classical barrier by pair creation of fermions: these cross unimpeded through the barrier and annihilate to (re-)create the magnetic field in the classically shielded region.

A statistical ensemble of fields, similarly to the oscillon simulations, is initially constructed for evaluating the fermionic contribution in the gauge field dynamics. This ensemble, importantly and in contrast to the bosonic case, involves two sets of fields to reproduce the anti-commuting nature of the fermion operator. The ensemble method, again, offers the possibility for a reduction in the computational resources required to evolve the system numerically. A test case indicates the method for the tunnelling system, though, requires impracticable computational resources.

Using the symmetries in the system to construct an ansatz for the fields provides an alternative method to evolve the dynamics on a lattice. This procedure effectively reduces the system to a $1 + 1$ dimensional problem with the fermion mode functions summed over the three-dimensional momentum space. The significant decrease in the real-time for the evolution (and quite attainable computational resources) on applying the ansatz provides a practical technique to examine the tunnelling.

Measuring the magnetic field in the classically shielded region confirms the analytic estimates. These (qualitatively) reproduced the exponential decrease estimated in the classical transmission on varying the interaction strength between the barrier and the magnetic field. The observed tunnelling signal, moreover,

matches the perturbative, analytic estimate within the expected correction in the lattice configuration.

These bosonic and fermionic quantum, dynamical simulations demonstrate limitations to the benefits in applying the ensemble method. The highly practical and successful tunnelling computations, in contrast, indicate the potential power of a suitable ansatz to significantly reduce the computational times in simulations on a lattice.

Acknowledgements

I am grateful to my PhD supervisor, Paul Saffin. His continual guidance throughout this long, part-time endeavour has been fundamental to the finished work. I am also greatly thankful to Anders Tranberg. Without his valuable insights, my efforts in quantum tunnelling especially would be much the poorer. My thanks also to Mou for many (many) valuable conversations on the many detailed aspects of numerical simulations.

This PhD research was kindly funded by the STFC. Numerical results presented for the oscillons were undertaken on the COSMOS Shared Memory system at DAMTP, University of Cambridge operated on behalf of the STFC DiRAC HPC Facility. The results presented for the tunnelling simulations were completed on the Abel Cluster, owned by the University of Oslo and the Norwegian metacenter for High Performance Computing (NOTUR), and operated by the Department for Research Computing at USIT, the University of Oslo IT-department. I am deeply grateful to have been spared the same work by hand.

Among the varied, non-technical help, a honourable mention is warranted for the diligent proofreading of Andrew, Susannah, my mum, brother, and Poppy. The prize for the most pages proofread though is (by a considerable margin) awarded to Matt Young. My thanks also for the experienced advice from my unofficial “third supervisor”, Zoltán, to Zann for all the tree planting to (re-)motivate the writing, and to the diverse residents of 3 Nazareth Road accommodating many hours of my writing, in their small zoo. Lastly, I would also add a special mention to the Nightingale clan: absolutely no thanks for all that jazz.

Contents

Abstract	iv
Acknowledgements	vii
Abstract	xii
1 Introduction: Oscillons	1
1.1 Overview of Solitons and Pseudo-Solitons	5
1.2 Oscillon Features	12
1.2.1 A Semi-Analytical Form	12
1.2.2 Lifetime and Decay	13
2 Quantum Oscillons: Dynamical Model	16
2.1 Classical System	16
2.1.1 Equation of Motion	16
2.1.2 The Scaled System	18
2.1.3 Initial Conditions	18
2.2 Quantum Dynamics	19
2.2.1 Applying the Hartree Approximation	19
2.2.2 Mode Expansion	22
2.2.3 The Scaled System	24
2.2.4 Initial Conditions	26
2.2.5 Lattice Site Quantity: Mode Functions	27

2.3	The Ensemble Method	27
2.3.1	Lattice Site Quantity: Ensemble Method	29
2.4	Discretized Dynamics	30
2.4.1	Derivatives	30
2.4.2	Classical Lattice-Dynamics	31
2.4.3	Quantum Lattice-Dynamics	32
3	Quantum Oscillons: Simulations	34
3.1	Parameter Choice for Numerical Simulations	34
3.2	Numerical Code	34
3.2.1	Ensemble Size	36
3.3	Choosing Initial Conditions	36
3.4	The Oscillon End-point	37
3.5	Typical Evolution Profiles	38
3.6	Evolution of the Oscillon Frequency	44
3.7	Determining Oscillon Lifetimes	48
3.8	Mapping the Attractor Basin	49
3.9	Conclusion	54
4	Introduction: Fermions	58
4.1	Solving Fermion Dynamics	59
4.2	Fermions on the Lattice	62
4.3	Quantum Tunnelling	66
5	Tunnelling of the 3rd Kind: Dynamical Setup	70
5.1	Continuum Dynamics	70
5.1.1	Action	70
5.1.2	Higgs-Field Configuration	72
5.1.3	Equations of Motion	74
5.2	Continuum Quantum-Dynamics	75

5.2.1	Quantized Equations of Motion	75
5.2.2	Mode Expansion	77
5.2.3	The Ensemble Approach	79
5.2.4	An Ansatz for the Fields	81
5.3	Tunnelling of the 3rd Kind: Simple Estimate	89
5.4	Discretized Dynamics	92
5.4.1	Action	92
5.4.2	Quantized Equations of Motion	97
5.4.3	Mode Expansion	99
5.4.4	Numerical Evolution: Mode Functions	102
5.4.5	The Ensemble Approach	104
5.4.6	Numerical Evolution: Ensemble Method	105
5.4.7	An Ansatz for the Fields	106
5.4.8	Numerical Evolution: Ansatz Case	113
5.5	Lattice Boundary Conditions	114
5.5.1	Periodic Boundaries	114
5.5.2	Neumann Boundaries	116
5.6	Initial Conditions	121
5.6.1	Fermion Field	121
5.6.2	Gauge Field, External Current and Higgs Phase	131
5.7	Generating the Uniform Magnetic-Field	133
5.7.1	External Current Configuration	133
5.7.2	Siting the External Current on the Lattice	135
5.7.3	Dissipating Generated Waves	136
6	Tunnelling of the 3rd Kind: Simulations	138
6.1	Parameter Choices for Numerical Simulations	138
6.2	Numerical Code	138
6.3	Computational Efficiency	140

6.3.1	Lattice-Site Quantity: Mode Functions	140
6.3.2	Lattice-Site Quantity: Ensemble Method	140
6.3.3	Lattice-Site Quantity: Ansatz Case	141
6.3.4	Measured Computational-Efficiencies	142
6.4	Renormalization	146
6.4.1	Numerical Renormalization Procedure	146
6.4.2	Evaluating the Renormalization	149
6.5	Tunnelling System on the Lattice	156
6.5.1	Wall Parameters	156
6.5.2	Lattice Parameters	157
6.5.3	Typical, Magnetic-Field Transmission	158
6.5.4	Tunnelling of the 3rd Kind: Detection	164
6.5.5	Conclusion	168
7	Summary and Outlook	172
A	Neumann Boundaries: Continuum	177
A.1	Solutions to the Neumann Constraint	179
A.2	Selecting the Fermion Boundary Condition	180
B	Neumann Boundaries: Discrete	184
B.1	Solutions to the Neumann Constraint	185
C	Functions of Pauli Matrices	187
	Bibliography	189

Publications

The majority of the work contained in the thesis has already been presented in two published works:

I. Chapters 2 and 3

Paul M. Saffin, **Paul M. Tognarelli**, and Anders Tranberg, “Oscillon Lifetime in the Presence of Quantum Fluctuations”, in: *Journal of High Energy Physics* 08 (2014), [arXiv: 1401.6168 [hep-ph]].

II. Chapters 5 and 6

Zong-Gang Mou, Paul M. Saffin, **Paul M. Tognarelli**, and Anders Tranberg, “Simulations of “Tunnelling of the 3rd Kind””, in: *Journal of High Energy Physics* 07 (2017), [arXiv: 1703.08375 [hep-ph]].

The work presented in the thesis was performed by the author, with advice from the paper coauthors listed above.

Chapter 1

Introduction: Oscillons

The fundamental nature of matter poses a widely intriguing subject. This topic provokes extensive scientific and philosophical concern, and engages popular interest. The universal nature of the issue for existence can produce the intertwining of the moral and the physical aspects of the topic [1], while the constant fascination about the topic evokes varied, artistic expressions (for instance, see [2, 3]).

Quantum field theory has proven to be a reliable basis for our scientific understanding of the topic. The standard model of particle physics forms a comprehensive framework to describe every known, elementary particle [4]. Measurements, in particular of dark matter and dark energy in the universe, provide tantalizing insight into exotic particle physics awaiting discovery [4].

A central component in the work of this thesis will involve the methodologies for practicably solving the inherently complex equations occurring within quantum field theories. The fundamental concern in deriving the physical properties generically reduces to the problem of evaluating non-linear correlators specifying the interactions in the theory. Perturbative expansions of the correlators provide the canonical method for obtaining the solution. This has proved highly effective for deriving varied properties observed within experiments (for a detailed overview, see for instance [5]). The perturbative approximations though limit

understanding to situations deviating from a limited number of analytic solutions. More importantly, these fail to examine the potentially rich non-linear effects possible within the system.

Expanding the quantum field operators into an orthogonal mode-basis satisfying the respective field dynamics provides the fundamental mechanism for determining the perturbative expansion.

A self-interacting scalar theory provides a definite and straightforward context to demonstrate the practicable methodologies. The non-linear terms occurring within the dynamics on quantization produce the correlator to solve. Evaluating the two point correlator in the mode function provides a ready expression for evaluating this correlator through the modes. Evaluating the higher-order correlators may be accomplished through reducing these to combinations of the two-point correlator. The resultant dynamics hence involve the effective contribution to the two-point interaction from the higher order operators and thus form a resummation of the non-linear interactions.

Asserting the full scalar-field to comprise a perturbation added to a background value provides a scenario where this simplification may be accomplished. The Hartree approximation imposes, additionally, that the mean value of these perturbations vanish, and thus the background value forms the quantum expectation [6–8]. This background may, accordingly, be treated classically, while the perturbations are expanded into the quantum modes. These modes, though, generate a back-reaction onto the mean field, through the quantum correlators in the dynamics; thus, the mode functions effectively encapsulate the quantum effects within the system. The Hartree approximation asserts the connected correlators higher than second order in the perturbation vanish. This importantly, hence, simplifies the dynamics to involve only the mean field and the connected two-point functions of the perturbations [6].

The large N approximation provides an alternative method for simplifying the dynamics on expansion into the mean field and perturbation. This procedure

involves N scalar-fields in the limit of large N , with the terms of $O(1/N)$ and smaller neglected [7]. The simplified correlators again involve only the mean field and the two-point functions throughout the dynamics.

Both the Hartree and large N approximation have proven highly effective for investigating a range of inherently non-perturbative scenarios. The Hartree approximation may, for instance, describe phase transitions within an inflationary context [9–11]; the $1/N$ approximation enables examining the potential for chiral condensates to form in heavy ion collisions [12]; and both methodologies have provided insight to particle production through the background field oscillations [7].

To implement the mode function method importantly involves an integration over the mode space; the discretization onto the lattice transforms this integral into a summation over the discrete mode space. On a d -dimensional lattice of N_L sites in each direction, the conjugate-momentum space comprises an identically sized lattice and hence the system entails evolving N_L^d values for each scalar field. This forms a readily tractable problem for $d = 1$; but can, for $d > 1$, involve increasingly extensive computational resources.

This numerical difficulty may be ameliorated through applying reasonable assumptions to constrain the modes computed. A standard regularization involves imposing a simple cut-off in the mode space; hence, where the physical constraints require this cut-off below the maximum momentum on the lattice, the regularization may limit the modes involved [11, 12]. If the dynamics determine that certain modes provide a divergent contribution to the correlators, these terms may dominate in the summation; and hence the relevant physics may be obtained through limiting the analysis to only these divergent modes [9, 10]. These methods both demonstrate cases where the physical properties of the system may limit the computational requirements as to produce a practicable simulation.

The Ensemble Method offers a related method to attempt alleviating the

sizeable field number in the mode function procedure. This alternative essentially replaces the quantum field operator and instead uses an ensemble of scalar fields [8, 13]. These fields are generated through an expansion equivalent to the mode expansion except a random number replaces the quantum ladder operators:

$$\begin{aligned}\hat{\phi}(t, \mathbf{x}) &= \int \frac{d^2\mathbf{k}}{(2\pi)^2} \left[\hat{a}_{\mathbf{k}} f_{\mathbf{k}}(t, \mathbf{x}) + \hat{a}_{\mathbf{k}}^\dagger f_{\mathbf{k}}^*(t, \mathbf{x}) \right] \\ \longrightarrow \varphi_n(t, \mathbf{x}) &= \int \frac{d^2\mathbf{k}}{(2\pi)^2} \left[c_{\mathbf{k},n} f_{\mathbf{k}}(t, \mathbf{x}) + c_{\mathbf{k},n}^* f_{\mathbf{k}}^*(t, \mathbf{x}) \right].\end{aligned}$$

The equivalent substitution, on discretization, likewise defines the ensemble on the lattice. A judicious choice of the random numbers hence enables the statistical properties of the ensemble to reproduce exactly the quantum correlators. Defining the random numbers in particular to form a Gaussian distribution with the statistical mean and variance equal to the quantum correlator value may reproduce the Hartree approximation (both in the continuum and lattice) for the scalar field¹. This distribution in principle assumes the random number from an infinite continuum-distribution and correspondingly the ensemble includes infinitely many fields. The ensemble method therefore initially seems only to complicate the analysis and, adversely, increase, rather than improve, the requirements for a computational analysis. In practice though, a finite number of fields may reproduce the quantum correlator to arbitrary accuracy; and if acceptable accuracy is obtained for the ensemble smaller than the mode space, the mode ensemble method therefore beneficially reduces the computational requirements to analyse the field.

This method has proven effective for examining the quantum effects in the highly non-perturbative scenarios of scalar-field solitons². The decay of a domain wall network, in particular, yielded a significant increase in the computational ef-

¹A detailed demonstration of this is provided in the quartic scalar theory examined subsequently (see Section 2.3)

²The application of the ensemble method also to fermionic systems is considered in the subsequent Chapters 4 - 6.

efficiency through the ensemble method [8]. These simulations, involving networks generated through random initial conditions, additionally required multiple simulations for averaging the resultant configurations. The cumulative increase in the overall efficiency for the multiple repetition thus demonstrates the especially significant gains in applying the ensemble method for multiple repetitions, each using different parameters. A significantly smaller ensemble size than the number of modes also provided sufficient accuracy for determining the lifetime of Q-Balls and related energies and charge [13]. The variation in charge notably included a prominent statistical noise resulting through the approximation in the finitely-sized ensemble. This demonstrates a limitation in the ensemble method for the practicable ensemble sizes to reproduce physical properties. The method, nonetheless, despite the noise, sufficiently determines the primary features in the evolution.

These successes in examining solitons have motivated the main work within the subsequent chapter to apply the Ensemble Method in examining the quantum effects on the lifetime of oscillons.

1.1 Overview of Solitons and Pseudo-Solitons

An assortment of field theories produce a variety of long-lived, non-perturbative field-configurations. The particular context and several important consequences of these phenomena will be examined in this section.

Formation of these spatio-temporal, ordered field-configurations is a phenomenon generic among non-linear systems. These structures occur within diverse contexts: ranging through hydrodynamics and networks of chemical reactions [14], within organisms [15], and in cosmological phase transitions [16–27]. This broad relevance emphasises the widespread significance of these field configurations.

Examining the non-linear regime in classical theories has yielded considerable

canonical results concerning in particular strictly time-invariant, localized configurations. An overview of these in several important cases and of their significant properties will presently provide the background for further examining the topic throughout this chapter.

The time-invariant configurations form a class of solutions termed solitons. Topological properties may in general support the localized configurations; and this distinguishes the important sub-class of “topological solitons” within the static field-configurations.

A symmetric, double-well potential in a scalar theory, for instance, includes two non-degenerate vacua; and in the simplest case forms a symmetric double-well. The symmetric case in $1 + 1$ D supports a static field configuration interpolating between the negative and positive vacuum state termed a “kink” [16]; the equivalent configuration simply interpolating between the vacua in reverse forms the anti-kink.

The Sine-Gordon potential similarly involves multiple vacua; and in $1 + 1$ D, a kink configuration exists interpolating between the vacua, with a corresponding anti-kink interpolating between the vacua in reverse [16, 28]. A simple Lorentz transform on the coordinates may also form a solution describing a propagating kink in the Sine-Gordon model. This thus demonstrates a further property typically ascribed to solitons: that of the field configuration comprising a wave packet travelling without any change in shape [28]. Solutions further describing a propagating kink and anti-kink and two kinks or two anti-kinks also exists in the Sine-Gordon model [28]. These enable examining the soliton interactions in collisions: demonstrating the configurations may collide and on separation their shape remains unaltered.

A class of structures analogous to the solitons though involving a time-dependent form may also be found in non-linear field theories. These related “pseudo-solitons” generically remain stable over periods much longer than the natural time-scale in the theory, but may vary semi-periodically and typically

unstable, they eventually decay.

The kink solutions in the 1 + 1D Sine-Gordon model notably may combine to form an oscillatory bound state termed a “breather” [16, 28]. This time-dependent but periodic structure thus results through the vacuum topology supporting the underlying soliton configurations.

Potentials with a discrete symmetry (for instance, a \mathbb{Z}_2 for a quartic scalar potential) similarly support domain walls [17]: a network of boundaries joining adjacent regions of the differing (discrete) vacua. These also provide a simplified analogue to the case where a continuous symmetry forms a continuum of vacuum states. This degeneracy in the vacuum, further, may generate vortices in 2 + 1D, and in 3 + 1D, equivalently, may yield networks of cosmic strings. The vortex configuration, essentially, involves a winding in the phase of a complex scalar at a single point, where the continuous variation of phase corresponds to the continuum of vacua; repeating this structure to define an extended, one-dimensional object in 3 + 1D forms the equivalent, cosmic string configuration [29]. Both the domain wall and string networks persist on cosmological timescales but the length per unit volume decreases according to scaling laws (for studies on domain wall decay-rates, see for example [8, 18] and for cosmic strings, see for example [30–32]).

Q-balls represent a further type of the pseudo-soliton configuration [33]. A conserved charge energetically favours the formation of these long-lived structures and likewise ensures their persistence. The Q-balls though may decay through disassociation into lower-energy Q-balls [34, 35] or into particle-like excitations [34].

Further to these familiar configurations, numerical studies have revealed a much lesser understood class of pseudo-solitons termed “oscillons” (see for instance [19–22, 36–57]). These structures form a localized, extended region substantially outside any vacuum. They characteristically oscillate quasi-periodically and persist for long periods compared to the natural time-scales of the system:

though may eventually decay into the surrounding vacuum-state. Unlike the conventional pseudo-solitons, their longevity results without any fundamental constraint – in particular neither through topology nor charge. This feature importantly distinguishes the oscillons.

They occur within numerous and varied systems in Minkowski spacetime. The most extensively examined case to generate oscillons involves a scalar field in a double-well, scalar potential. This system may form scalar-field oscillons significantly in $3 + 1\text{D}$ [36–42]; but also in two [40, 41], four and five [19, 20, 40–46] or also six spatial dimensions [42]. The Sine-Gordon potential likewise supports a scalar-field oscillon in $2 + 1\text{D}$ [43, 44]; the more physical Abelian-Higgs in $2 + 1\text{D}$ [47] and $3 + 1\text{D}$ [54], and $\text{SU}(2)$ -Higgs systems in $3 + 1\text{D}$ [54–58] also generate scalar field oscillons.

Oscillons may also form in an expanding spacetime. A quartic, scalar potential provides a generic approximation to the post-inflationary potential; and the evolution on the expanding background after inflation, in $3 + 1\text{D}$ enables the formation of oscillons [48]. These oscillons persist also where the inflaton couples to a massless scalar field. The ϕ^6 potential provides a further generic approximation to the post-inflationary potential and is also conducive to the formation of oscillons in $3 + 1\text{D}$ [49, 50]. A generic power law potential motivated through string and supergravity scenarios forms a realistic inflationary-potential; and the evolution in $2 + 1\text{D}$ indicates a further prospective context in the early universe for the formation of oscillons [51].

These varied field-structures and diverse contexts producing them demonstrate the broad relevance of the soliton and pseudo-soliton configurations. The subsequent discussion will presently examine the effect of the configurations in several significant cases.

Symmetry-breaking scenarios occur repeatedly throughout the early universe [16] and the potential for pseudo-solitons to form in the resultant contexts implies these configurations may affect the cosmological dynamics. The possibility, in

particular, for cosmic string formation has inspired extensive investigation into their cosmological impact and assessing their compatibility with astrophysical observations (see for instance [59–64]); the related domain-walls also provided insights into the nature of pseudo-solitons in the early universe (see for instance [16–18, 23]).

Q-Balls further may result through the various supersymmetry-breaking scenarios to potentially affect cosmological evolution. These structures may in particular contribute to dark matter [24, 25]; and may affect baryogenesis [26].

The instantaneous quench from a single-well potential to a double-well for a system initially in a thermal state similarly demonstrates the potential for the natural formation of oscillons. These result due to the parametric resonance over the range of modes corresponding to the oscillons. The linearized equations of motion immediately ensuing the phase transition [19, 20] form a Mathieu equation in wave-vector space [19–21]. This system (under the approximation also of a homogeneous potential) implies parametric resonance results for certain modes [19–22]. The range in wave-vector space where these resonances occur matches the modes comprising a typical oscillon [19–21]. This therefore implies the approximately homogeneous potential remaining after the quench produces parametric resonance in certain modes and accordingly forms the mechanism to generating copious oscillons in the phase-transition.

Examining the mode space also indicates the oscillon production crucially delays equilibrium after the quench to a symmetric double-well. The fraction of kinetic energy in each mode is concentrated in the low-momentum modes immediately subsequent to the quench and only transferred slowly to the higher-momenta [20]. This restriction of the energy to the low-momentum modes coincided with the formation of oscillons [19, 20]; while the majority of the energy corresponded almost exactly to the momenta typically comprising an oscillon [20]. The copious production of the oscillons after the quench therefore evidently restricts the energy to the low-momentum modes and thus hinders the eventual

thermalization [19, 20].

An instantaneous quench further to an asymmetric double-well where the field value is around the false vacuum will produce a subsequent decay to the global minimum. Oscillon formation further may affect this transition. The standard assumption where regions of the true vacuum are nucleated on a homogeneous background predicts the transition rate to the global minimum occurs exponentially suppressed [65, 66]. Those quenched states abundantly producing the oscillons may accelerate the transition to a power law rate [20–22]; while a reduction in the number of oscillons changes the exponent in the faster, power law to an increasingly negative value, tending towards the standard, exponentially-suppressed transition-rate [20, 21]. This therefore indicates the presence of oscillons alters the transition-rate from the homogeneous-nucleation case. The presence of oscillons evidently invalidates the homogeneous calculation [21]. These structures may, effectively, nucleate a region of the field in the global minimum, forming an additional contribution in the transition of the whole space to the true vacuum. Producing fewer oscillons, hence, decreases this enhanced contribution to the transition rate and, correspondingly may generate a smooth variation to the homogeneous transition-rate [20, 21].

Oscillons may also result in post inflationary scenarios where the perturbations within the inflationary field may source the formation [48–51]. The ϕ^6 potential, although an unrealistic inflationary potential, may provide a general approximation for the true inflationary field around the potential minimum after inflation [49–51]. This enables the abundant production of oscillons. With these lasting for periods much longer than the Hubble timescale, an oscillon-dominated period may consequently form [49, 50]. These abundant oscillons potentially may contain over seventy per cent of the total energy density in the post inflationary universe [49].

The power law potential, generically obtained through string and supergravity theories, thus, represents a general class of physically motivated inflationary

scenarios [51]. These more realistic potentials, likewise, may also support copious oscillon production, to form a post inflationary period where these structures dominate. The quartic potential provides a further approximation to the post inflationary potential generating the formation of oscillons [48]. This system significantly also on the coupling to a further massless scalar field still retains the copious oscillon production in the post-inflationary expansion. Both the coupled and uncoupled system may form an oscillon dominated period where these pseudo-solitons comprise initially between three and thirty per cent of the total energy density. This fraction decays while the expansion continues; but a significant fraction remain stable over cosmological timescales.

These extensive oscillon regions may source particle production in the early universe. The eventual decay generally results through energy transferred into particle production, and, hence, the copiously produced oscillons may contribute to baryogenesis. This oscillon formation in the post inflationary epoch may also generate primordial gravitational waves [67]. These form a distinctive power spectrum related to the dominant frequencies in the typical, quasi-periodic oscillons.

The varied contexts where soliton and pseudo-soliton structures exist demonstrates the broad applicability of examining these phenomena, while the very general formation-contexts imply a strong potential to generate the structures in reality. Those scenarios further where the configurations strongly affect the cosmological evolution indicate further the need for a quantum treatment to accurately examine their significance. The (generically created) oscillon configurations in particular provide a tantalizing form to potentially examine in the quantum regime. A scalar field oscillon further forms a convenient configuration to examine the effects such structures may generate – and may also apply directly to the inflaton evolution in the post-inflationary universe. Analytical approximation may provide insight into various aspects of the pseudo-soliton (see for instance [68–71]). Without an analytic expression for an oscillon though,

only a numerical examination can provide an accurate insight into the processes governing the phenomenon. The difficulties involved in solving a highly non-perturbative quantum system further determines that computation offers the most efficient method to examine quantum effects on the oscillon. To examine the evolution, and in particular to capture the decay inherently entails a real-time simulation. Implementing the real-time, quantum simulation techniques to determine the oscillon lifetimes will hence form the primary concern in examining the scalar field subsequently.

1.2 Oscillon Features

1.2.1 A Semi-Analytical Form

Neither solving the scalar field dynamics nor fitting to the observed profiles in simulations has yet determined a precise analytical form for oscillons. Semi-analytical approximations though enable categorizing the oscillons into several qualitative categories. The Gaussian approximation for the oscillon profile forms the most extensively applied ansatz to examine oscillons (for uses in analytical analyses see for instance [20, 36, 40, 45, 52, 67, 68], and in numerical simulations [36–46, 52, 55]). A true Gaussian-profile will initially radiate energy to transform into the semi-stable oscillon configuration [42, 43]. This loss indicates the Gaussian inaccurately matches the oscillon profile; but the generally small amount lost confirms the Gaussian may accurately approximate the oscillon. A further approximation to oscillons in $1 + 1\text{D}$ are in the “flat-topped” class of configurations [72]. These structures, unlike the peaked Gaussian profiles, form a plateaued maximum. Numerical simulations confirm the flat-topped configurations closely approximate oscillons formed in $1 + 1\text{D}$, while also comparable though more extensively extended structures occur [50]; and simulations confirm similarly flat-topped structures also form in $3 + 1\text{D}$ [49].

The Gaussian approximation ultimately will form the initial configuration

for generating oscillons in the subsequent numerical simulations. This profile explicitly satisfies

$$\Phi(t, r) = v_{\pm} \left(1 - A_0(t) \exp(-r^2/r_0^2) \right), \quad (1.1)$$

where the Gaussian form is superimposed on the (positive or negative) broken-phase vacuum v_{\pm} . The amplitude A_0 and radius r_0 parametrize the varied configurations.

Numerical simulations indicate that oscillons evolve on a unique trajectory [41, 42] and is an attractor in field space [42, 46, 53, 54, 69]. Initializing the field in the Gaussian approximation to the oscillons may therefore reliably evolve into the oscillon trajectory. The initial energy emission hence affects the transformation to a point in the oscillon evolution – the resultant structure then oscillating throughout the remaining stable-period in the trajectory before decaying. Determining in particular the initial radii and amplitudes generating oscillons may effectively delineate the basin of attraction within this Gaussian parameter-space.

1.2.2 Lifetime and Decay

The stability of scalar-field oscillons results through the particular frequencies forming the pseudo-oscillatory configuration (see for instance [41, 42, 44, 45, 69]). These configurations comprise oscillations, in natural units, primarily concentrated in a narrow range of frequencies centred around a value below the mass. The mass defines the intrinsic frequency of the system; while simulations demonstrate configurations above this frequency efficiently transfer energy to free-field excitations [41, 44, 45]. This concentration of the oscillon frequencies primarily below the radiative frequency, hence, classically, prevents the oscillon transferring energy into free waves.

Higher harmonics and equally the bandwidth around the dominant component, although of significantly lower amplitude than the primary frequency,

nonetheless exceed the radiative frequency. These therefore enable the oscillon to classically transfer energy, if only inefficiently, into free waves, and thus slowly decay [42, 44, 45, 69]. The dominant frequency, though, increases throughout the evolution [41, 42, 44]; the persistence of the oscillon structure further indicates the components around the main value also will change to maintain a similar distribution of frequencies around the dominant component. This gradually may increase both the range of frequencies above the radiation frequency and results in the progressively higher amplitude components, closer to the dominant value increasing to above of the radiation frequencies. The oscillon will transfer energy into free waves with increasing efficiency; and once the energy transfer grows sufficiently large, the oscillon abruptly collapses. Simulations demonstrate the collapse, in particular, results when the dominant frequency of the oscillon is still slightly below the radiative frequency [41, 42, 44]. This endpoint, in real space, occurs where the oscillon amplitude is slightly greater than the inflection-point of the potential [37, 44]. The dominant component in frequency of the field configuration at this stage changes abruptly to above the radiative frequency [41, 42]; and the oscillon amplitude rapidly decreases into the vacuum [44].

A quantum treatment enables accurately examining the energy transfer into particle production. The additional, distinctively quantum mechanisms may increase the energy loss compared to the classical limit of the system. This may accordingly quicken the decay and decrease the time until the oscillon entirely collapses; if the decay rate increases sufficiently, the particle production might also prevent the oscillons from forming. A perturbative (analytical) calculation indicates the quantum effects strongly alter the oscillon lifetime and even may dominate the decay rate [70].

Quantizing the system also modifies the effective scalar potential. This change for Q-Balls significantly changed the purely classical conditions on the configuration [13]. The modified potential created a lower limiting-frequency on the possible Q-balls: the effective quantum-potential at frequencies below this value

invalidating the (classical) conditions for the system to form a Q-ball. A change in the attractor basin may likewise result for oscillons on the modification to the potential. The change in potential may also alter the stage where the initial configuration commences on the unique oscillon trajectory or entirely alter this trajectory: consequently, in either case, significantly altering the consequent oscillon lifetimes. This in combination with the decay may substantially reduce the oscillon lifetimes, or even entirely prevent their formation.

The potentially significant quantum-effects thus pose an intriguing matter to investigate. Calculating the changes, in particular, to the oscillon basin of attraction in the Gaussian parameter-space of the equation (1.1) will form a definite context for examining this question presently.

Chapter 2

Quantum Oscillons: Dynamical Model

2.1 Classical System

2.1.1 Equation of Motion

We consider a single, classical scalar field now specifically in 2 + 1D, on a flat spacetime of positive signature $(-, +, +)$, evolving in a quartic potential (see figure 2.1):

$$S = -\frac{1}{c} \int c dt d^2 \bar{\mathbf{x}} \left[\frac{1}{2} \bar{\partial}_\mu \bar{\phi}(\bar{t}, \bar{\mathbf{x}}) \bar{\partial}^\mu \bar{\phi}(\bar{t}, \bar{\mathbf{x}}) - \frac{c^2 m^2}{2 \hbar^2} \bar{\phi}^2(\bar{t}, \bar{\mathbf{x}}) + \frac{\lambda}{4 \hbar^2} \bar{\phi}^4(\bar{t}, \bar{\mathbf{x}}) + \frac{c^4 m^4}{4 \hbar^2} \right]. \quad (2.1)$$

Setting $m \in \Re$ and $\lambda > 0$ creates a 'broken phase' potential comprised of two minima (see figure 2.1), defining the vacuum field values: $v^\pm = \pm \sqrt{c^2 m^2 / \lambda}$. This structure provides a potential known to support oscillons [8, 37, 38, 42, 43, 45, 46, 70].

Applying the variational principle to this action hence yields the equation of motion for the classical scalar field:

$$\left[\bar{\partial}_0 \bar{\partial}_0 - \sum_i \bar{\partial}_i \bar{\partial}_i - \frac{c^2 m^2}{\hbar^2} + \frac{\lambda}{\hbar^2} \bar{\phi}^2(\bar{t}, \bar{\mathbf{x}}) \right] \bar{\phi}(\bar{t}, \bar{\mathbf{x}}) = 0. \quad (2.2)$$

The Lagrangian density of the classical action notably also defines the stan-

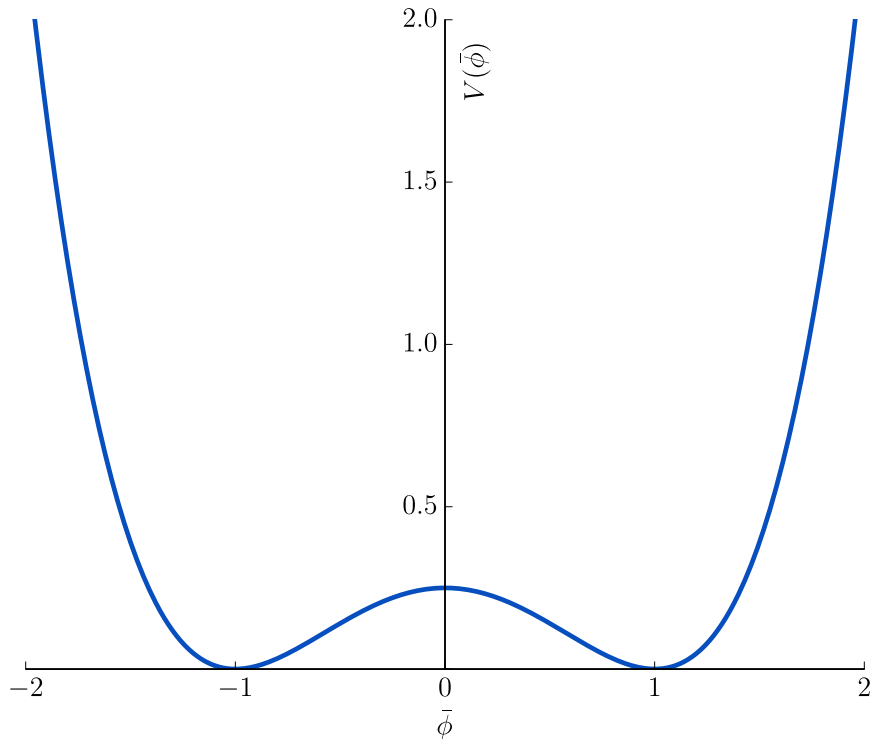


Figure 2.1: The typical, classical potential $V(\bar{\phi})$ of the system, shown for natural units with $m = \lambda = 1$. (These are essentially the parameters chosen in the subsequent classical dynamics: see equation (2.5) where the scaling essentially sets m and λ to unity in the dynamics; and see also Section 3.1 on the choice of natural units.) This potential illustrates the distinctive double-well structure known to generate oscillons.

ward, conjugate momentum:

$$\bar{\pi}(\bar{t}, \bar{\mathbf{x}}) = \bar{\partial}_0 \bar{\phi}(\bar{t}, \bar{\mathbf{x}}). \quad (2.3)$$

This will ultimately provide a useful variable for formulating the classical dynamics to evolve numerically; and will also form the basis for constructing the quantum equations of motion.

2.1.2 The Scaled System

Scaling the action under the transformation

$$\bar{x}^\mu \equiv |m|^{-1} x^\mu, \quad (2.4a)$$

$$\bar{\phi} \equiv \sqrt{\frac{m^2}{\lambda}} \phi \quad (2.4b)$$

specifies the system in entirely dimensionless quantities; and on applying the variational principle, yields dynamics for the scaled system without explicit mass or coupling parameter:

$$\left[\partial_0 \partial_0 - \sum_i \partial_i \partial_i - \frac{c^2}{\hbar^2} + \frac{1}{\hbar^2} \phi^2(t, \mathbf{x}) \right] \phi(t, \mathbf{x}) = 0. \quad (2.5)$$

This in effect has removed the parameter choice; and further ensures any results obtained for these dynamics are entirely general to any form of the quartic potential, the exact values only differing by the relevant scaling factors.

2.1.3 Initial Conditions

The (semi-analytical) Gaussian ansatz (1.1) on the positive vacuum v_+ will provide the initial configuration for evolving the scalar field. This structure importantly provides a configuration potentially within the attractor basin of the unique oscillon trajectory. Varying the amplitude A_0 and width r_0 of this initial configuration may, hence, determine the region of this Gaussian parameter space in the attractor basin.

Initialization further requires choosing the initial time-derivative of the scalar field. This variable notably is the conjugate momentum of the field. Setting the value to zero, hence, corresponds physically to creating an initially static field. The initial, Gaussian amplitude in this case consequently forms the maximum excursion from the vacuum; and hence, the initial amplitude (rather than a

subsequently, larger peak) specifies the effective Gaussian configuration evolving in the simulation.

Constructing the Gaussian field (1.1) for varying amplitude A_0 and width r_0 , with the momentum set to zero, therefore, provides the complete set of initial conditions chosen for the classical case.

2.2 Quantum Dynamics

2.2.1 Applying the Hartree Approximation

On quantization, the classical scalar field and the conjugate momentum are promoted to operators in the Heisenberg representation satisfying the equal time commutator relations

$$\left[\hat{\phi}(\bar{t}, \bar{\mathbf{x}}), \hat{\pi}(\bar{t}, \bar{\mathbf{y}}) \right] = i\hbar c (2\pi)^2 \delta^2(\bar{\mathbf{x}} - \bar{\mathbf{y}}). \quad (2.6)$$

Any operator \hat{O} in the Heisenberg representation satisfies the equation of motion

$$\bar{\partial}_0 \hat{O}(\bar{t}, \bar{\mathbf{x}}) = -\frac{i}{\hbar c} \left[\hat{O}(\bar{t}, \bar{\mathbf{x}}), \hat{H}(\bar{t}) \right], \quad (2.7)$$

where \hat{H} is the Hamiltonian operator formed on converting the fields in the classical Hamiltonian (expressed in terms of the conjugate momentum) to the corresponding quantum operators:

$$\hat{H}(\bar{t}) = \int d^2\bar{\mathbf{x}} \left[\frac{1}{2} \hat{\pi}^2(\bar{t}, \bar{\mathbf{x}}) + \frac{1}{2} \sum_i \left(\bar{\partial}_i \hat{\phi}(\bar{t}, \bar{\mathbf{x}}) \right)^2 - \frac{c^2 m^2}{2\hbar^2} \hat{\phi}^2(\bar{t}, \bar{\mathbf{x}}) + \frac{\lambda}{4\hbar^2} \hat{\phi}^4(\bar{t}, \bar{\mathbf{x}}) + \frac{c^4 m^4}{4\hbar^2} \right].$$

Substituting this operator into the equation of motion on setting $\hat{O} = \hat{\phi}$, and

applying the commutator relation (2.6) determines

$$\hat{\pi}(\bar{t}, \bar{\mathbf{x}}) = \bar{\partial}_0 \hat{\phi}(\bar{t}, \bar{\mathbf{x}}).$$

This result thus matches the classical conjugate momentum (2.3) except in operator form. Applying this procedure again on setting $\hat{O} = \hat{\pi}$ in the operator equation, and substituting the expression of the momentum operator into the result yields

$$\left[\bar{\partial}_0 \bar{\partial}_0 - \sum_i \bar{\partial}_i \bar{\partial}_i - \frac{c^2 m^2}{\hbar^2} + \frac{\lambda}{\hbar^2} \hat{\phi}^2(\bar{t}, \bar{\mathbf{x}}) \right] \hat{\phi}(\bar{t}, \bar{\mathbf{x}}) = 0. \quad (2.8)$$

This effectively recovers the classical equations of motion except converting the fields to the corresponding quantum operators.

The full quantum-operator may be divided into two components:

$$\hat{\phi}(\bar{t}, \bar{\mathbf{x}}) = \bar{\Phi}(\bar{t}, \bar{\mathbf{x}}) \hat{\mathbb{I}} + \delta \hat{\phi}(\bar{t}, \bar{\mathbf{x}}). \quad (2.9)$$

Setting the quantum expectation of $\delta \hat{\phi}$ to zero further determines $\langle \hat{\phi} \rangle = \bar{\Phi}$. The field $\bar{\Phi}$ thus forms the background mean-field with the $\delta \hat{\phi}$ representing fluctuations on this background. Enforcing the Gaussian Hartree approximation on the $\delta \hat{\phi}$ asserts that the quantum expectation of the connected correlators higher than second order in these fluctuations vanish. The $\delta \hat{\phi}$ in this sense form a perturbation to the background mean-field. Applying the approximation, moreover, re-expresses the expectation of the third and higher order correlators in terms of the two-point, connected pieces (for a detailed explanation, see for instance [6]). This, importantly, defines the quantum effects through the effective two-point interactions.

The Hartree approximation in particular implies the three-point correlator in

the dynamics may simplify to

$$\langle \hat{\phi}^3(\bar{t}, \bar{\mathbf{x}}) \rangle = \bar{\Phi}^3(\bar{t}, \bar{\mathbf{x}}) + 3\langle \delta\hat{\phi}(\bar{t}, \bar{\mathbf{x}})\delta\hat{\phi}(\bar{t}, \bar{\mathbf{x}}) \rangle \bar{\Phi}(\bar{t}, \bar{\mathbf{x}}).$$

Forming the expectation of the operator dynamics (2.8) and substituting this approximation into the dynamics hence yields

$$\left[\bar{\partial}_0 \bar{\partial}_0 - \sum_i \bar{\partial}_i \bar{\partial}_i - \frac{c^2 m^2}{\hbar^2} + \frac{\lambda}{\hbar^2} \left[\bar{\Phi}^2(\bar{t}, \bar{\mathbf{x}}) + 3\langle \delta\hat{\phi}(\bar{t}, \bar{\mathbf{x}})\delta\hat{\phi}(\bar{t}, \bar{\mathbf{x}}) \rangle \right] \right] \bar{\Phi}(\bar{t}, \bar{\mathbf{x}}) = 0. \quad (2.10)$$

This forms the dynamical equation specifying the evolution of the background mean-field. The dynamics are notably identical to the classical scalar-dynamics (2.2) except for the addition of the quantum, two-point correlator in the perturbations. This modification in effect forms a perturbative quantum-correction to the classical background¹. The correlator, in particular, affects the dynamics in a manner equivalent to the mass term and, thus, corresponds to a quantum correction of the scalar mass.

First multiplying the operator dynamics (2.8) by $\hat{\phi}(\bar{t}, \bar{\mathbf{y}})$ and then forming the expectation further yields,

$$\left[\bar{\partial}_{x,0} \bar{\partial}_{x,0} - \sum_i \bar{\partial}_{x,i} \bar{\partial}_{x,i} - \frac{c^2 m^2}{\hbar^2} \right] \langle \hat{\phi}(\bar{t}, \bar{\mathbf{x}})\hat{\phi}(\bar{t}, \bar{\mathbf{y}}) \rangle + \frac{\lambda}{\hbar^2} \langle \hat{\phi}^3(\bar{t}, \bar{\mathbf{x}})\hat{\phi}(\bar{t}, \bar{\mathbf{y}}) \rangle = 0,$$

where the x subscript expressly denotes the action of the partial derivative on only the site x , without affecting the y -coordinate. The Hartree approximation to the expectation of the resultant four-point correlator implies

$$\langle \hat{\phi}^3(\bar{t}, \bar{\mathbf{x}})\hat{\phi}(\bar{t}, \bar{\mathbf{y}}) \rangle = \bar{\Phi}^3(\bar{t}, \bar{\mathbf{x}})\bar{\Phi}(\bar{t}, \bar{\mathbf{y}}) + 3 \left(\bar{\Phi}^2(\bar{t}, \bar{\mathbf{x}}) + \langle \delta\hat{\phi}(\bar{t}, \bar{\mathbf{x}})\delta\hat{\phi}(\bar{t}, \bar{\mathbf{x}}) \rangle \right) \langle \delta\hat{\phi}(\bar{t}, \bar{\mathbf{x}})\delta\hat{\phi}(\bar{t}, \bar{\mathbf{y}}) \rangle.$$

¹This identification will later inform the choice for the initial conditions: the mean-field set identically to the classical scalar, and the perturbations to be vacuum quantum fluctuations.

Combining these results and applying the mean-field dynamics (2.10) yields the dynamical equation for the perturbation, two-point correlator:

$$\left[\bar{\partial}_{x,0} \bar{\partial}_{x,0} - \sum_i \bar{\partial}_{x,i} \bar{\partial}_{x,i} - \frac{c^2 m^2}{\hbar^2} + \frac{3\lambda}{\hbar^2} \left[\bar{\Phi}^2(\bar{t}, \bar{\mathbf{x}}) + \langle \delta \hat{\phi}(\bar{t}, \bar{\mathbf{x}}) \delta \hat{\phi}(\bar{t}, \bar{\mathbf{x}}) \rangle \right] \right] \langle \delta \hat{\phi}(\bar{t}, \bar{\mathbf{x}}) \delta \hat{\phi}(\bar{t}, \bar{\mathbf{y}}) \rangle = 0. \quad (2.11)$$

This result forms the basis to calculate the quantum back-reaction on the mean-field evolution 2.10. The procedure for obtaining the correlator back-reaction will be examined presently.

2.2.2 Mode Expansion

Expanding the perturbation field into a set of orthogonal mode functions $\bar{f}_{\bar{\mathbf{k}}}$ forms the standard method to evaluate the quantum correlators. The expansion is constructed to satisfy

$$\delta \hat{\phi}(\bar{t}, \bar{\mathbf{x}}) = \sqrt{\hbar c} \int \frac{d^2 \bar{\mathbf{k}}}{(2\pi)^2} \left[\hat{a}_{\bar{\mathbf{k}}} \bar{f}_{\bar{\mathbf{k}}}(\bar{t}, \bar{\mathbf{x}}) + \hat{a}_{\bar{\mathbf{k}}}^\dagger \bar{f}_{\bar{\mathbf{k}}}^*(\bar{t}, \bar{\mathbf{x}}) \right], \quad (2.12)$$

where the $\{\bar{f}_{\bar{\mathbf{k}}}\}$ comprise an orthonormal set, and the $\{\hat{a}_{\bar{\mathbf{k}}}^\dagger\}$ and $\{\hat{a}_{\bar{\mathbf{k}}}\}$ are respectively the creation and annihilation operators. These operators, further, are time-independent and asserted to satisfy

$$[\hat{a}_{\bar{\mathbf{k}}}, \hat{a}_{\bar{\mathbf{l}}}^\dagger] = (2\pi)^2 \delta^2(\bar{\mathbf{k}} - \bar{\mathbf{l}}). \quad (2.13)$$

This notably ensures that the mode expansion recovers the constraint on the full quantum-operator to satisfy the constraint canonical commutator (2.6)².

²The mode expansion may be determined to reproduce the canonical commutator most readily for the vacuum initial conditions (examined in Section 2.2.4); the conservation of the canonical commutator hence implies this constraint remains valid at later times. (This procedure is outlined in the particular case of fermions on the lattice in the subsequent Section 5.6.1.)

The annihilation operator also defines the vacuum state:

$$\hat{a}_{\bar{\mathbf{k}}} |0\rangle = 0.$$

This will provide the initial state of the system; and in the Heisenberg picture, this initial state-vector will remain the relevant state acted on at all subsequent times.

Substituting the expansion into the correlator $\langle \delta \hat{\phi}(\bar{t}, \bar{\mathbf{x}}) \delta \hat{\phi}(\bar{t}, \bar{\mathbf{y}}) \rangle$ and applying the definition of the vacuum state yields

$$\langle \delta \hat{\phi}(\bar{t}, \bar{\mathbf{x}}) \delta \hat{\phi}(\bar{t}, \bar{\mathbf{y}}) \rangle = \hbar c \int \frac{d^2 \bar{\mathbf{k}}}{(2\pi)^2} \bar{f}_{\bar{\mathbf{k}}}(\bar{t}, \bar{\mathbf{x}}) \bar{f}_{\bar{\mathbf{k}}}^*(\bar{t}, \bar{\mathbf{y}}).$$

This expression substituted into the correlator dynamics (2.11) hence determines

$$\left[\bar{\partial}_0 \bar{\partial}_0 - \sum_i \bar{\partial}_i \bar{\partial}_i - \frac{c^2 m^2}{\hbar^2} + \frac{3\lambda}{\hbar^2} \left[\bar{\Phi}^2(\bar{t}, \bar{\mathbf{x}}) + \langle \delta \hat{\phi}(\bar{t}, \bar{\mathbf{x}}) \delta \hat{\phi}(\bar{t}, \bar{\mathbf{x}}) \rangle \right] \right] \bar{f}_{\bar{\mathbf{k}}}(\bar{t}, \bar{\mathbf{x}}) = 0, \quad (2.14)$$

where the orthogonality of the modes and the action of the dynamics on only the x -coordinates (and not the y -coordinates) yields the linear expression in the mode function. Substituting the mode expansion (2.12) into the two-point correlator evaluated at identical coordinates further yields

$$\langle \delta \hat{\phi}(\bar{t}, \bar{\mathbf{x}}) \delta \hat{\phi}(\bar{t}, \bar{\mathbf{x}}) \rangle = \hbar c \int \frac{d^2 \bar{\mathbf{k}}}{(2\pi)^2} |\bar{f}_{\bar{\mathbf{k}}}|^2. \quad (2.15)$$

This result and the dynamical equation (2.14), together, determine the evolution of the mode functions. The correlator expression (2.15) at equal points, moreover, specifies the quantum back-reaction on the mean-field dynamics entirely in terms of the mode functions. These results thus determine the quantum evolution through the mode functions

The correlator (2.15) evaluated at equal coordinates, significantly, is divergent. Subtracting the initial ($\bar{t} = 0$) correlator though eliminates the constant,

infinite contribution to the correlator. This modification, in both the mean-field (2.10) and mode function (2.14) dynamics, generates a contribution to the equations of motion equivalent to a mass term. The subtraction, thus, corresponds to performing a standard, mass renormalization throughout the dynamics:

$$m^2 \rightarrow m^2 - \frac{3\lambda}{c^2} \langle \delta \hat{\phi}(0, \bar{\mathbf{x}}) \delta \hat{\phi}(0, \bar{\mathbf{x}}) \rangle.$$

2.2.3 The Scaled System

Performing the transformation to dimensionless variables (2.4), with the field scaling imposed on both the mean-field and perturbations yields

$$\left[\partial_0 \partial_0 - \sum_i \partial_i \partial_i - \frac{c^2}{\hbar^2} + \frac{1}{\hbar^2} \left[\Phi^2(t, \mathbf{x}) + 3 \langle \delta \hat{\phi}(t, \mathbf{x}) \delta \hat{\phi}(t, \mathbf{x}) \rangle \right] \right] \Phi(t, \mathbf{x}) = 0, \quad (2.16a)$$

$$\left[\partial_{x,0} \partial_{x,0} - \sum_i \partial_{x,i} \partial_{x,i} - \frac{c^2}{\hbar^2} + \frac{3}{\hbar^2} \left[\Phi^2(\bar{t}, \bar{\mathbf{x}}) + \langle \delta \hat{\phi}(t, \mathbf{x}) \delta \hat{\phi}(t, \mathbf{x}) \rangle \right] \right] \langle \delta \hat{\phi}(t, \mathbf{x}) \delta \hat{\phi}(t, \mathbf{y}) \rangle = 0. \quad (2.16b)$$

These notably exclude any explicit parameters in the potential.

Forming the mode expansion for this case yields

$$\delta \hat{\phi}(t, \mathbf{x}) = \sqrt{\hbar c} \int \frac{d^2 \mathbf{k}}{(2\pi)^2} \left[\hat{a}_{\mathbf{k}} f_{\mathbf{k}}(t, \mathbf{x}) + \hat{a}_{\mathbf{k}}^\dagger f_{\mathbf{k}}^*(t, \mathbf{x}) \right], \quad (2.17)$$

where each mode function independently satisfies the scaled, correlator dynamics (2.16b). The $\{\hat{a}_{\mathbf{k}}^\dagger\}$ and $\{\hat{a}_{\mathbf{k}}\}$ are respectively the creation and annihilation operators in the scaled system. These are time independent; and the requirement for them to reproduce the commutator (2.6) determines

$$[\hat{a}_{\mathbf{k}}, \hat{a}_{\mathbf{l}}^\dagger] = \frac{\lambda}{|m|} (2\pi)^2 \delta^2(\mathbf{k} - \mathbf{l}). \quad (2.18)$$

The coordinate scaling also implies

$$\bar{k} = |m| k, \quad (2.19)$$

and, hence, the ladder commutators in the scaled system (2.18) and the unscaled system (2.13) further determine that these operators transform under

$$\begin{aligned} \hat{a}_{\bar{\mathbf{k}}} &= \sqrt{\frac{\lambda}{|m|}} \hat{a}_{\mathbf{k}}, \\ \hat{a}_{\bar{\mathbf{k}}}^\dagger &= \sqrt{\frac{\lambda}{|m|}} \hat{a}_{\mathbf{k}}^\dagger. \end{aligned} \quad (2.20)$$

Equating the mode expansion in the scaled case (2.17) and the unscaled case (2.12) through the field scaling, on applying also the ladder scalings (2.20) and the wave-vector relation (2.19) hence determines

$$\bar{f}_{\bar{\mathbf{k}}} = \sqrt{|m|} f_{\mathbf{k}}. \quad (2.21)$$

This relation importantly will be necessary later to define the initial mode functions.

Lastly, substituting the mode expansion into the two-point correlator of the perturbation field yields

$$\langle \delta \hat{\phi}(t, \mathbf{x}) \delta \hat{\phi}(t, \mathbf{x}) \rangle = \hbar c \frac{\lambda}{|m|} \int \frac{d^2 \mathbf{k}}{(2\pi)^2} |f_{\mathbf{k}}|^2. \quad (2.22)$$

The resultant expression notably involves the mass and coupling only in the ratio $\lambda/|m|$. This ratio also notably performs an identical role in the correlator to the Planck's constant and thus setting the value of the ratio determines the scale of the quantum corrections on the mean-field dynamics.

The scaling importantly has eliminated the explicit mass and coupling parameters in the dynamics (2.16) with the parameters present only through the

correlator where they occur in the ratio $\lambda/|m|$. This importantly limits the parameter choice to simply choosing this ratio; and further implies that the results obtained for a particular choice are entirely general to any coupling and mass in that ratio.

2.2.4 Initial Conditions

Mean Field

Considering the previous identification of the analogy between the mean field and the classical scalar hence informs the initialization of the mean field to the Gaussian configuration (1.1); and the mean-field time derivative zero everywhere. This will enable examining the Gaussian attractor basin of the quantum oscillons directly in comparison to the classical case.

Quantum Perturbation

The expansion (2.12) defines the perturbation field in particular at initialization in terms of the initial mode functions; and further yields the perturbation time derivative specified through the mode functions in particular at the initial time. This fully specifies the independent, perturbative variables at initialization through the initial modes and their time derivatives.

From the assertion that the perturbation field is small, the initial mode functions in the unscaled system are chosen to yield the vacuum configuration of the perturbations where the two-point correlator of the field vanishes. This implies that the (unscaled) mode dynamics (2.14) reduce to the free ($\lambda = 0$) vacuum equations except with the mean-field term modifying the mass. The initial modes accordingly are the familiar, plane-wave configuration:

$$\bar{f}_{\bar{\mathbf{k}}}(0, \bar{\mathbf{x}}) = \frac{1}{\sqrt{2\omega_{\bar{\mathbf{k}}}}} \exp(i\bar{\mathbf{k}} \cdot \bar{\mathbf{x}}), \quad \bar{\partial}_0 \bar{f}_{\bar{\mathbf{k}}}(0, \bar{\mathbf{x}}) = i\sqrt{\frac{\omega_{\bar{\mathbf{k}}}}{2}} \exp(i\bar{\mathbf{k}} \cdot \bar{\mathbf{x}}), \quad (2.23)$$

where $\omega_{\bar{\mathbf{k}}} = (\bar{\mathbf{k}}^2 + c^2 m^2/\hbar^2 + 3\lambda\bar{\Phi}^2/\hbar^2)^{\frac{1}{2}}$ includes the mean field modification

to the mass term. Self-consistency with the vacuum mode-configuration requires that the background mean-field – determining the $\omega_{\bar{\mathbf{k}}}$ in each mode – occupies the classical-vacuum $\bar{\Phi}^2 = c^2 m^2 / \lambda$.

Applying the mode functions scaling (2.21) in particular, at the initial time yields our choice for the initial quantum-perturbation and its time derivative in the scaled system; the field-transformation (2.4b), also at the initial time yields the background-vacuum $\Phi^2 = c^2$ to fully specify the scaled, vacuum mode functions.

2.2.5 Lattice Site Quantity: Mode Functions

The quantum evolution may directly be computed from the equation (2.16a) and (2.16b) with the two-point correlators computed through the expansion in the scaled mode functions (2.22).

Discretizing the system onto a square lattice of N sites in each direction corresponds to forming a discrete momentum space of equally many sites; and accordingly, the mode expansion of the lattice field is reduced to the finite sum over the conjugate lattice. The numerical simulation thus entails N^2 modes and the one mean field, on a $N \times N$ lattice: for any reasonably large lattice ($N \gg 1$), the total number of sites scales as $\sim N^4$.

2.3 The Ensemble Method

An alternative method to evolve the quantum system eliminates all the perturbations from the dynamics, requiring instead an ensemble of M scalar fields $\{\varphi_n\}$. These fields are constructed to satisfy

$$\varphi_n(t, \mathbf{x}) = \sqrt{\hbar c} \int \frac{d^2 \mathbf{k}}{(2\pi)^2} [c_{\mathbf{k},n} f_{\mathbf{k}}(t, \mathbf{x}) + c_{\mathbf{k},n}^* f_{\mathbf{k}}^*(t, \mathbf{x})], \quad (2.24)$$

where the $f_{\mathbf{k}}$ are the quantum mode functions and $\{c_{\mathbf{k},n}\}$ are random, complex numbers.

Each of the ensemble fields effectively comprises a linear combination of the mode functions; the linearity of the mode dynamics (2.16b) hence implies these linear combinations each also satisfy this equation. Evolving an ensemble field under the mode dynamics thus effectively evolves all the mode functions simultaneously.

The random numbers for each \mathbf{k} , on averaging over the ensemble are chosen to satisfy a Gaussian form of mean zero and variance

$$\begin{aligned}\langle c_{\mathbf{k}}c_{\mathbf{l}}^* \rangle_E &= \frac{1}{2} \frac{\lambda}{|m|} (2\pi)^2 \delta^2(\mathbf{k} - \mathbf{l}), \\ \langle c_{\mathbf{k}}c_{\mathbf{l}} \rangle_E &= 0.\end{aligned}$$

This provides equality between the two-point correlator and the variance of the ensemble fields:

$$\langle \varphi(t, \mathbf{x})\varphi(t, \mathbf{x}) \rangle_E = \hbar c \frac{\lambda}{|m|} \int \frac{d^2\mathbf{k}}{(2\pi)^2} |f_{\mathbf{k}}|^2 = \langle \delta\hat{\phi}(t, \mathbf{x})\delta\hat{\phi}(t, \mathbf{x}) \rangle, \quad (2.25a)$$

$$\langle \partial_0\varphi(t, \mathbf{x})\partial_0\varphi(t, \mathbf{x}) \rangle_E = \hbar c \frac{\lambda}{|m|} \int \frac{d^2\mathbf{k}}{(2\pi)^2} |\partial_0 f_{\mathbf{k}}|^2 = \langle \partial_0\delta\hat{\phi}(t, \mathbf{x})\partial_0\delta\hat{\phi}(t, \mathbf{x}) \rangle. \quad (2.25b)$$

In particular, choosing the set of the real-part $A_{\mathbf{k},n}$ and of the imaginary-part $B_{\mathbf{k},n}$ of $c_{\mathbf{k},n}$ to both be independent, Gaussian distributions of mean zero and variance

$$\langle A_{\mathbf{k}}A_{\mathbf{l}} \rangle_E = \langle B_{\mathbf{k}}B_{\mathbf{l}} \rangle_E = \frac{1}{4} \frac{\lambda}{|m|} (2\pi)^2 \delta^2(\mathbf{k} - \mathbf{l})$$

may produce the Gaussian constraints on the complex, random numbers. These purely real numbers thus, in effect, replace the ladder operators in the quantum dynamics.

The equivalence (2.25) may be obtained expressly at the initial time for the vacuum mode functions (2.23 and 2.21). This, therefore, ensures the initial en-

semble variance matches the resultant quantum correlator for the choice of vacuum initial conditions. The effective evolution of all the mode functions in the ensemble dynamics hence implies that these modes forming each ensemble field at all times equal those evolved from the vacuum in the mode function method. This, therefore, crucially ensures the equivalence (2.25) remains valid throughout the evolution.

The quantum correlator can hence consistently be replaced everywhere in the dynamics with the ensemble variance:

$$\left[\partial_0 \partial_0 - \sum_i \partial_i \partial_i - \frac{c^2}{\hbar^2} + \frac{1}{\hbar^2} [\Phi^2(t, \mathbf{x}) + 3\langle \varphi(t, \mathbf{x}) \varphi(t, \mathbf{x}) \rangle_E] \right] \Phi(t, \mathbf{x}) = 0, \quad (2.26a)$$

$$\left[\partial_0 \partial_0 - \sum_i \partial_i \partial_i - \frac{c^2}{\hbar^2} + \frac{3}{\hbar^2} [\Phi^2(t, \mathbf{x}) + \langle \varphi(t, \mathbf{x}) \varphi(t, \mathbf{x}) \rangle_E] \right] \varphi_n(t, \mathbf{x}) = 0. \quad (2.26b)$$

This result thus specifies the quantum dynamics entirely in the mean-field and the ensemble.

2.3.1 Lattice Site Quantity: Ensemble Method

The quantum evolution may directly be computed from the equation (2.26a) and (2.26b) with the quantum back-reaction on the mean-field computed through the variance of the ensemble field (2.25a).

Numerical analysis on a square lattice of N sites per dimension entails discretizing both the mean-field and the M ensemble fields on this space: for any reasonably large lattice ($N \gg 1$), the total site number scales as $\sim MN^2$. The ensemble size (corresponding to the continuum of Gaussianly distributed $A_{\mathbf{k},n}$) in principle is infinite. In practice though, a finite number of fields is sufficient

for numerical convergence of the mean-field evolution to reasonable accuracy³. Notably, if $M < N^2$ at convergence, the system increases in size slower than the $\sim N^4$ scaling on explicitly computing the mode functions.

2.4 Discretized Dynamics

2.4.1 Derivatives

Discretizing the system at the level of the dynamics presently will yield the equations to evolve on the lattice⁴. Implementing this where the dynamics are first expressed in terms of the conjugate momentum will provide the basis to implement the evolution using a leap-frog algorithm.

The standard approximation of the differential with respect to x_μ , accurate to second order in Δx_μ , is explicitly

$$\partial_\mu f(x) \approx \frac{f(x + \mu) - f(x - \mu)}{\Delta x_\mu} + O((\Delta x_\mu)^2); \quad (2.27)$$

and likewise, the second-order approximation to the second derivative satisfies

$$\partial_\mu^2 f(x) \approx \frac{f(x + \mu) + f(x - \mu) - 2f(x)}{(\Delta x_\mu)^2} + O((\Delta x_\mu)^2).$$

These provide the essential relations for completing the discretization.

³For an infinite random ensemble, the imposed initial ensemble-variance exactly matches the initial, quantum, two-point correlator; while an analytic expression for the initial variance may provide an alternative method to accurately compute this quantity. In practice, for a finite ensemble-size, the variance differs from the full ensemble, and hence from the initial two-point correlator. Computing the difference between the analytic expression for the correlator and the ensemble variance, therefore, provides a measure of the precision of the finite ensemble in reproducing the quantum result.

⁴Constructing the discrete equivalent to the continuum action (2.1) and applying the variational principle may likewise yield the lattice dynamics. Forming the discrete equivalent of the continuum dynamics provides a simpler alternative. The results in both cases though are identical.

2.4.2 Classical Lattice-Dynamics

Constructing a scaled momentum satisfying

$$\pi(t, \mathbf{x}) = \partial_0 \phi(t, \mathbf{x}) \quad (2.28)$$

will provide a convenient variable to formulate the lattice dynamics. (This notably defines the scaled momentum analogously to the unscaled version (2.3) except $\bar{x}_0 \rightarrow x_0$ and $\bar{\phi} \rightarrow \phi$. The definition would also equate precisely to the conjugate momentum obtained on scaling the action.) Substituting this definition into the scaled, classical equations of motion (2.5) hence implies

$$\partial_0 \pi(t, \mathbf{x}) - \left[\sum_i \partial_i \partial_i + \frac{c^2}{\hbar^2} - \frac{1}{\hbar^2} \phi^2(t, \mathbf{x}) \right] \phi(t, \mathbf{x}) = 0.$$

Applying the approximation of the first and second derivative respectively to the momentum term and the spatial gradient and evaluating the equation only at the discrete coordinates X_i on the lattice and at the discrete time-step T yields the discretized version of the dynamics. The approximation of the first derivative applied to the scaled momentum (2.28) (and evaluating this only at the discretized spacetime coordinates) further defines the discrete momentum. Rearranging the resultant equations into an expressly iterative form hence specifies

$$\begin{aligned} \pi(T+0, X) &= \pi(T-0, X) \\ &+ \sum_i \frac{\Delta x_0}{(\Delta x_i)^2} [\phi(T, X+i) + \phi(T, X-i) - 2\phi(T, \mathbf{X})] \\ &+ \Delta x_0 \left[\frac{c^2}{\hbar^2} - \frac{1}{\hbar^2} \phi^2(T, \mathbf{X}) \right] \phi(T, \mathbf{X}), \end{aligned} \quad (2.29a)$$

$$\phi(T+0, X) = \phi(T-0, X) + \Delta x_0 \pi(T, \mathbf{X}). \quad (2.29b)$$

These relations form the basis to evolve the discrete system in a leap-frog algorithm. This procedure evaluates the momentum at a time $T + \Delta t$ using the

scalar field at time T in the former equation (2.29a). The discretized momentum (2.29b) consequently enables calculating the field values at $T + 2\Delta t$. This process may then be repeated to iteratively evolve the fields.

2.4.3 Quantum Lattice-Dynamics

The momentum of the scaled, mean-field may be construed analogously to the classical definition (2.28):

$$\Pi(t, \mathbf{x}) \equiv \partial_0 \Phi(t, \mathbf{x}). \quad (2.30)$$

(This notably equates precisely to the expectation value of the momentum obtained on quantizing the scaled action with the expectation of the (unscaled) perturbations vanishing.) Substituting this definition into the scaled, quantum, mean-field dynamics (2.26a), and evaluating the equation only at the discrete coordinates X_i on the lattice and at the discrete time-step T yields

$$\begin{aligned} \partial_0 \Pi(T, \mathbf{X}) - \left[\sum_i \partial_i \partial_i + \frac{c^2}{\hbar^2} \right. \\ \left. - \frac{1}{\hbar^2} [\Phi^2(T, \mathbf{X}) + 3\langle \varphi(T, \mathbf{X}) \varphi(T, \mathbf{X}) \rangle_E] \right] \Phi(T, \mathbf{X}) = 0. \end{aligned} \quad (2.31)$$

Applying the approximation of the first and second derivative respectively to the momentum term and the spatial gradient yields the discretized version of the dynamics; the approximation of the first derivative applied to the quantum momentum (2.30) further defines the discrete momentum. Rearranging the resulting

equations into an expressly iterative form specifies

$$\begin{aligned}
\Pi(T + 0, X) &= \Pi(T - 0, X) \\
&+ \sum_i \frac{\Delta x_0}{(\Delta x_i)^2} [\Phi(T, X + i) + \Phi(T, X - i) - 2\Phi(T, \mathbf{X})] \\
&+ \Delta x_0 \left[\frac{c^2}{\hbar^2} - \frac{1}{\hbar^2} [\Phi^2(T, \mathbf{X}) + 3\langle \varphi(T, \mathbf{X}) \varphi(T, \mathbf{X}) \rangle_E] \right] \Phi(T, \mathbf{X}), \\
\Phi(T + 0, X) &= \Phi(T - 0, X) + \Delta x_0 \Pi(T, \mathbf{X}).
\end{aligned} \tag{2.32}$$

These relations enable evolving the quantum mean fields in a leap-frog algorithm equivalently to the classical dynamics. The essential difference though is the requirement to also calculate the ensemble variance, modelling the quantum back-reaction, in the scalar field evolution.

Obtaining the iteration relations for the ensemble fields enables evaluating this variance at successive time steps in the simulations. Defining the momentum of the ensemble field

$$\pi_n(t, \mathbf{x}) = \partial_0 \varphi_n(t, \mathbf{x}),$$

analogously to the mean-field momentum (2.30) (and also the classical momentum (2.28)), enables discretizing the ensemble dynamics equivalently to the mean-field. The resultant equations in expressly iterative form thus specify:

$$\begin{aligned}
\pi_n(T + 0, X) &= \pi_n(T - 0, X) \\
&+ \sum_i \frac{\Delta x_0}{(\Delta x_i)^2} [\varphi_n(T, X + i) + \varphi_n(T, X - i) - 2\varphi_n(T, \mathbf{X})] \\
&+ \Delta x_0 \left[\frac{c^2}{\hbar^2} - \frac{3}{\hbar^2} [\Phi^2(T, \mathbf{X}) + \langle \varphi(T, \mathbf{X}) \varphi(T, \mathbf{X}) \rangle_E] \right] \varphi_n(T, \mathbf{X}), \\
\varphi_n(T + 0, X) &= \varphi_n(T - 0, X) + \Delta x_0 \pi_n(T, \mathbf{X}).
\end{aligned} \tag{2.33}$$

These determine that a leap-frog algorithm may likewise evolve the ensemble fields to hence obtain the quantum back-reaction at successive time-steps.

Chapter 3

Quantum Oscillons: Simulations

3.1 Parameter Choice for Numerical Simulations

Imposing throughout the dynamics natural units of $\hbar = c = 1$ simplified the numerical implementation. This fully sets the evolutionary scales in the transformed, classical system. The single ratio in the potential parameters remains to uniquely determine the perturbation scale (equivalent to \hbar ; see Section 2.2.3) in the transformed, quantum system. This ratio, for simplicity, is also asserted to satisfy $\lambda/m = 1$ throughout.

3.2 Numerical Code

Converting the iteration relations (2.29) for the classical field and the conjugate momentum into a C code provided the basis for evolving the classical system. The scalar field initialization simply involves setting the discretized field to the value of the Gaussian ansatz (1.1) evaluated at the relevant lattice sites. These values were computed using the standard library of C maths operations, with the amplitude and radius provided through user input on initialization. The initial conjugate momentum is likewise set simply to zero everywhere on the lattice. Computing the classical evolution was accomplished, conveniently, using only a

serial code.

Implementing the iteration relations (2.32) of the quantum mean-field and those of the ensemble field (2.33) also in a C code provided the basis for computing the quantum evolution. The code applies the Open MPI libraries to parallelize the evolution for the large number of ensemble fields. Each processor evolves the mean field and corresponding momentum to compute the ensemble evolution, with a subset of the ensemble fields and the corresponding momenta; an MPI reduce command calculates the summation over the ensemble variables to compute the ensemble variances in the dynamics.

The mean field initialization involved simply setting the values of the field and the conjugate momentum across the lattice, equivalently to the classical fields. Forming the discrete equivalent to the mode expansion of the ensemble fields (2.24) enabled constructing the initial configuration in wave-vector space. The standard vacuum solution chosen for the initial mode functions (see Section 2.2.4) determines the expansion at the initial time forms, simply, a Fourier Transform. This was computed efficiently using the FFTW routines. A standard numerical method generates the randomly distributed numbers for the coefficients in the expansion. This procedure employs a standard algorithm [73] to generate random numbers uniformly distributed in the interval $[0, 1)$. A further routine subsequently converts these to Gaussianly distributed variables, where the mean and variance for those coefficients of a single k -value are set to satisfy the constraints (see Section 2.3) on the ensemble. The effective independence of the random numbers in the initial stage ensures the variance for coefficients of differing wave-vectors vanish, to impose also the independence of the distinct k -components in the expansion (see again Section 2.3). A characteristic value in the initial stage, importantly, determines the pseudo-random numbers generated; hence, setting this distinctly on each processor ensures each processor contributes a distinct set of fields to the total ensemble.

3.2.1 Ensemble Size

The discretization of the system onto a square lattice of $N = 256$ ensured computations over practical durations. Choosing the lattice spacing $\Delta x_1 = \Delta x_2 = \Delta x_3 = 0.8$ and time-step $\Delta x_0 = 0.05$ provided convergence in the evolved fields. These intervals, in particular, eliminated the (evidently unphysical) regrowth of the field observed at larger values of these parameters for some of the initial conditions.

A very large number of realizations M was necessary in this inhomogeneous system: the results only converged around $M = 60000$ and above. For a lattice of $N = 256$, this is a very small gain in computational operations time compared to solving all the $N^2 = 65536$ mode functions. This demonstrates the considerable difficulty in computing the quantum effects on the oscillon dynamics

3.3 Choosing Initial Conditions

The space of the Gaussian initial profile (1.1) in the region $A_0 \in [-4, 4]$ and $r_0 \in [0, 4]$ covers the main boundaries of the classical-oscillon basin of attraction [42]. Each point in the region of negative, initial amplitude A_0 corresponds, in a non-trivial manner, to a point in the positive region. The initial configuration, in particular, evolves through half an oscillon to a maximum excursion, equivalent to an initial Gaussian configuration of opposite sign in the amplitude. This indicates that studying only the positive range of A_0 is sufficient to comprehensively examine the quantum system in contrast to the classical case. Excluding also low values of r_0 and A_0 where no oscillons are formed classically further constrains the parameter space to study, and correspondingly reduces the necessary computation time. The pairings (A_0, r_0) are thus chosen in the region $A_0 \in [0.25, 4]$ and $r_0 \in [1, 4]$. In particular, every pairing was constructed in this space, from the minimum value of each range and increasing at discrete intervals of 0.25 up to the maximum.

These initial configurations were then evolved on the square lattice of size $N = 256$ with a converged ensemble of size $M = 256^2 = N^2$. Selected parameter pairings were repeated on larger lattices of $N = 384$ and $N = 512$. The ensemble size was also increased to N^2 for each larger simulation, ensuring these maintained the condition obtained on the smallest lattice for the ensemble to converge. For fixed lattice spacing, the increasing lattice-size provided a test for finite volume effects; and for a decreasing lattice spacing to maintain fixed physical volume, the set of larger simulations provided checks on resolution effects.

3.4 The Oscillon End-point

A convenient definition for the endpoint of the oscillon will be when the envelope of the oscillations at the centre of the configuration first crosses the classical inflection-point in the scaled potential.

The abrupt change in the dominant frequency of oscillations from below to above the mass threshold provides a distinctive indication of the collapse of the classical oscillon. This equivalently occurs where the amplitude of the configuration is only slightly greater than the inflection-point in the (classical) potential, closest to the vacuum around which the field oscillates; then the amplitude rapidly decreases. (For the details on the eventual decay, see Section 1.2.2). Examining the field in real space provides a more convenient measure to determine the final collapse – without the need to complete a Fourier transform to examine the frequency components present. Where the envelope of the (scaled) field at the centre of the configuration first ceases to extend further than the inflection-point in the (scaled) classical potential, and closest to the vacuum around which the oscillations occur, will therefore provide a convenient definition for the endpoint of the oscillon.

Applying the field scaling (2.4b) to the classical potential in the (unscaled)

action (2.1) yields

$$V(\phi) \equiv -\frac{c^2 m^4}{2\hbar^2 \lambda} \phi^2(t, \mathbf{x}) + \frac{m^4}{4\hbar^2 \lambda} \phi^4(t, \mathbf{x}) + \frac{c^4 m^4}{4\hbar^2}.$$

The inflection-point ϕ_f of this potential in the scaled system may hence readily be determined:

$$\left. \frac{d^2}{d\phi^2} V(\phi) \right|_{\phi_f} = 0 \quad \Rightarrow \quad \phi_f = \pm \sqrt{\frac{c^2}{3}}.$$

This implies $\phi_f = \pm\sqrt{1/3}$ for the choice of natural units. For also the field configuration oscillating around the positive vacuum (see section 2.1.3), the positive value will form nearest the vacuum around which the configuration oscillates and thus define the endpoint of the oscillon.

3.5 Typical Evolution Profiles

A comparison of the core field-value from identical, Gaussian configurations (1.1) in both the classical and quantum case in figure 3.1 illustrates the typical evolution both inside (left) and outside (right) the basin of attraction.

The classical evolution inside the basin of attraction (top, left) settles into an oscillon lasting beyond the simulation time; while outside the basin (top right), the central value decays below the inflection-point of the potential in under two oscillations of the field.

In the quantum case, the initialization outside the basin of attraction evolves almost identically to the classical system: no oscillon forms and the field decays in only a few oscillations. The quantum back-reaction, thus, generates no significant effect outside the basin of attraction. Comparing the evolution within the basin of attraction, however, readily shows a distinctive change on including the quantum effects. The oscillations in the classical case remain fairly constant through the majority of the evolution and below the classical inflection-point; the quantum case, though, decays within a gently decreasing envelope until after

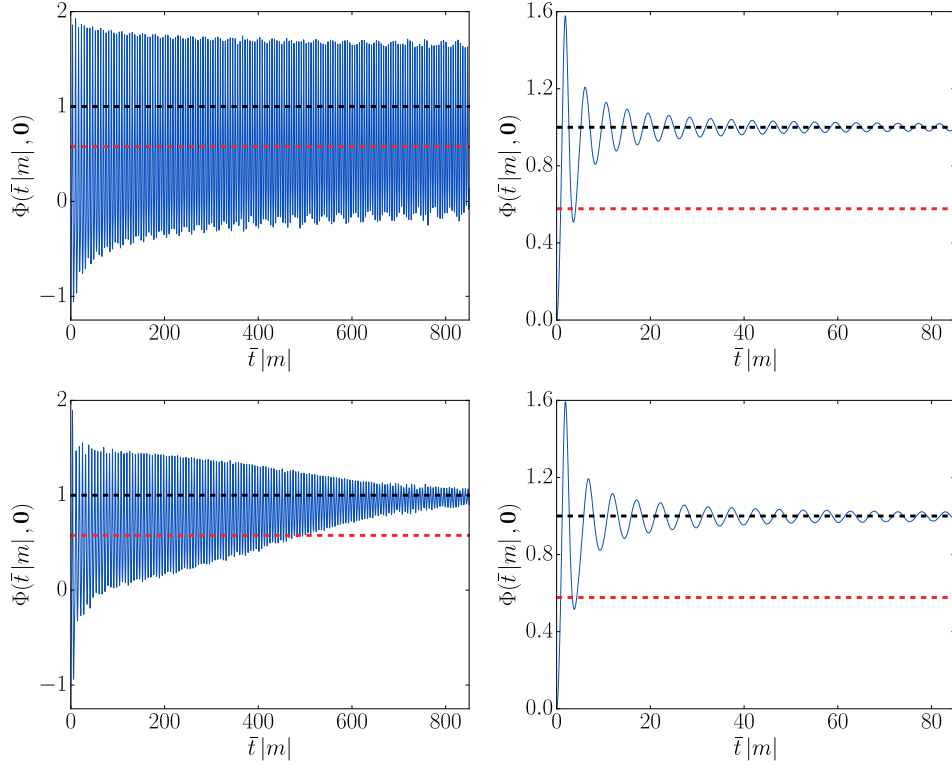


Figure 3.1: The time evolution of the centre of a configuration with an initial condition inside (left) and outside (right) the basin of attraction for the classical (top) and quantum (bottom) oscillon, where the field amplitude is in units of $\sqrt{m^2/\lambda}$. $(A_0, r_0) = (2.25, 2.5)$ and $(1.0, 1.5)$ respectively in the initial Gaussian configuration (1.1). The configurations oscillates around the positive vacuum (black, dashed), and the change in amplitude to above the inflection-point (red, dashed) of the classical potential defines the endpoint of the oscillon.

approximately one hundred periods, the amplitude ceases to extend below the classical inflection-point.

These cases, for the particular choice of initial Gaussian configuration, also demonstrate a much larger decrease in the amplitude within than first two oscillations in the quantum system, compared to the classical case. The Gaussian form, only an approximation to the oscillon configuration causes an initial transient, in both the classical and quantum system. This transient is relatively small in the

classical case illustrated; and, thus, confirms the highly accurate approximation of the Gaussian to the oscillon configuration in the classical system. The comparatively larger, initial decay in the quantum case simply illustrates the Gaussian configuration forms a poorer approximation to the true oscillon in the quantum system.

The quantum case, nonetheless, demonstrates that the effective Hartree approximation may yield long-lived, oscillon solutions. This confirms certain Gaussian configurations are sufficiently similar to these solutions to evolve into the true oscillon-configuration. The lifetimes of these oscillons are evidently much shorter than in the classical case. Further, the manner of the eventual decay by these quantum oscillons is distinctly different: while the classical configurations terminate in a sudden collapse (see Section 1.2.2 for a discussion), the quantum oscillations gradually decrease in amplitude. No significant change, in particular, occurs in the quantum evolution when the oscillation amplitude nears the classical inflection-point. This notably contrasts the collapse at this stage of the classical oscillon, indicating that this classical value has no relation to the shape of the effective, quantum potential.

The quantum oscillon also, notably decays towards the positive vacuum of the classical potential: verifying that the renormalization procedure, although only approximate, is adequate.

Several of the initial configurations in the quantum system generate an oscillatory envelope at a longer period, modulating the basic, underlying oscillations. Simulations at the higher resolutions for a selection of such cases eliminated the strong modulations (see figure 3.2, left for an illustrative case). These artefacts of the coarser lattice spacing (grey line, in the figure 3.2) essentially vanished on the increase in spatial resolution (blue line, in the figure 3.2), to generate purely oscillations around the positive vacuum (black, dashed line, in the figure 3.2) at an amplitude below the inflection-point (red, dashed line, in the figure 3.2) of the potential. This revealed the endpoint of these oscillatory configurations to have

clearly occurred around the time when the field in even the coarsest simulation first crossed the classical point of inflection. Any distinctive appearance of comparably strong beats further to those explicitly examined were hence disregarded as unphysical; and the end of oscillations considered to be where the field first crossed the inflection-point¹.

A beat-frequency of shorter period and smaller amplitude than the evidently unphysical instances also modulated the underlying oscillations in several instances (see figure 3.2, right for an illustrative case; the grey line shows the lower spatial resolution). Evolving a set of these instances at the higher spatial resolutions (blue line, in the figure 3.2) demonstrated the beat-frequencies remained. This type of beat-frequency notably also modulated the underlying oscillon in several classical cases.

Beating of this type has been observed in previous, detailed examinations of scalar field oscillons in similar contexts: formed in symmetric double-well potentials, from Gaussian initial conditions [37, 43]². A careful examination demonstrated certain values of the radius in the initial profile (1.1) produce a local resonance in the oscillon lifetime. Small deviations from such a resonant radius generates the type of beating observed in the present quantum-simulations [37].

This type of beating has also been found in the scalar field oscillons, evolved from Gaussian initial conditions in the sine-Gordon potential [43]. The oscillons forming in the SU(2)-gauged, Higgs system also demonstrate similar beating dependent on the particular initial conditions [55].

¹These strong beats arose at varied points in the parameter space of initial profiles. The stark emergence of the beat-frequency after initially evolving similarly to neighbouring points in parameter space, together with the peculiar nature of the beat-frequency in comparison to the evolution on the underlying oscillons was sufficient to distinguish the unphysical modulations. Completing the larger simulations to confirm the beat-frequencies to be unphysical in every such case was prohibitively time consuming.

²An investigation of oscillons in an anti-symmetric, double-welled potential has also noted the occurrence of these beat-frequencies [36].

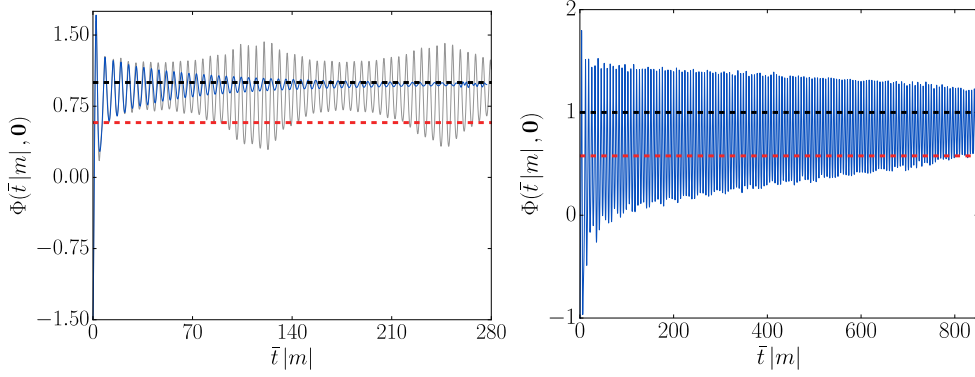


Figure 3.2: Initial conditions illustrating the two, distinct classes of beat-frequencies modulating the oscillon evolution where the field amplitude is in units of $\sqrt{m^2/\lambda}$. These oscillate around the positive vacuum-value (black, dashed) and when crossing the inflection-point (red, dashed), are considered to have decayed. The choice of $(A_0, r_0) = (2.5, 1.5)$ in the Gaussian initial condition (1.1) produces the large-amplitude modulations of the oscillon (grey) on the coarser lattice spacing. These entirely vanish (blue) for fixed volume, on reducing the lattice spacing. This determines the large-amplitude modulations are purely lattice spacing artefacts. The initial choice of $(A_0, r_0) = (2.5, 2.5)$ (right) demonstrates the smaller-amplitude and shorter-period modulations of the oscillon (blue) for the coarser lattice spacing. These remain qualitatively unchanged (although the frequency changes slightly) on reducing the lattice spacing, with the volume fixed. This type of beat-frequency also occurs in the classical evolution; this is illustrated in the oscillon configuration in figure 3.1 (top, left), where the beat-frequency is more pronounced than in the quantum illustration above. The examination of this type of modulations in various, more detailed studies implies these beat-frequencies are a physical, long-lived transient, resulting from the discrepancy in the initial conditions to the true oscillon structure. These modulations also include an unphysical component demonstrated in their change on reducing the lattice spacing. This may be neglected though in the measurement of the oscillon lifetime.

These studies thus demonstrate a physical type of beat-frequency, with the form depending on the initial conditions. This beating is hence likely a long-lived transient, occurring due to the discrepancy between the Gaussian initial conditions and the true oscillon³.

The similar nature of the modulations in this study and the persistence on the change in lattice resolution, therefore, confirms the physical nature of these small-amplitude modulations in the current simulations. Their changing amplitude and frequency on the change in resolution implies an unphysical component also in their behaviour. This therefore indicates the lattice spacing simply provides insufficient resolution to accurately study these physical beat-frequencies. Examining this feature, though, is not the subject of the present study. Accurately determining the beat-frequencies is also not required to detect the existence of the underlying oscillon, nor is the overall decay of the oscillon substantially altered through the details of the beating frequencies (see also Section 3.7 subsequently). Setting the resolution to accurately reproduce these beat-frequencies therefore may reasonably be neglected to examine the oscillon lifetimes.

Any similar, comparably weak beat-frequencies, further to the sample examined, were therefore considered to represent a physical modulation (if not of accurate amplitude and frequency) without simulations at a higher lattice-resolution. The oscillons modulated by these beat-frequencies likewise were regarded to be physical, with their decay obtained to sufficient accuracy.

³This is analogous to evolving a ‘kink and anti-kink’ configuration from imprecise initial conditions. The system rapidly sheds energy to form the combined kink and anti-kink but with oscillations superimposed on this soliton configuration. (See [37] for a more detailed comparison between the oscillon and kink cases.)

3.6 Evolution of the Oscillon Frequency

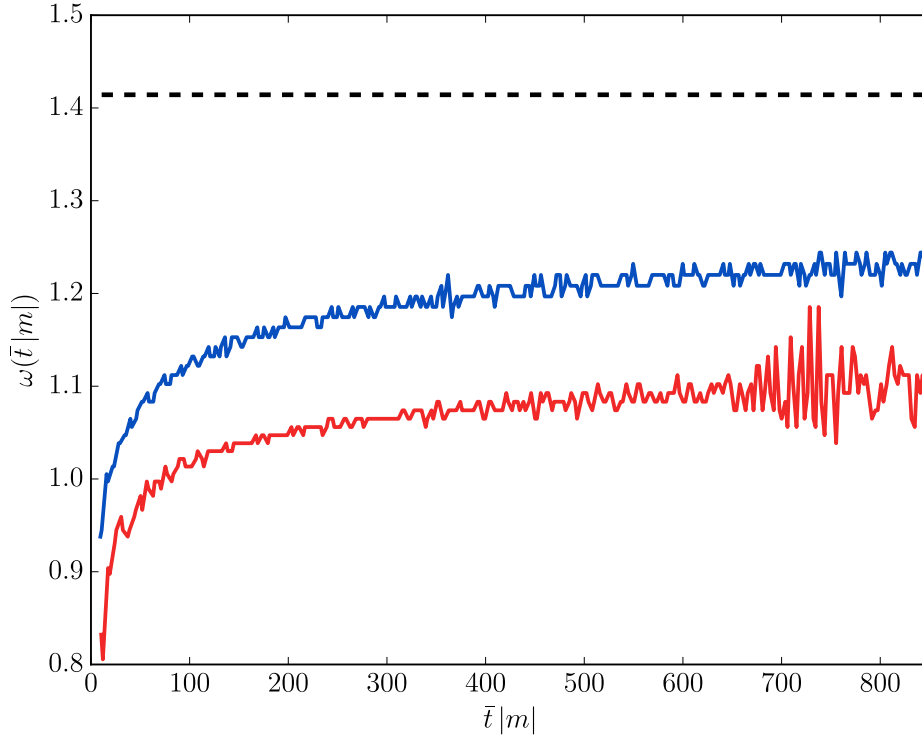


Figure 3.3: The frequency (in units of $|m|$) for a classical (blue) and the corresponding quantum (red) oscillon where $(A_0, r_0) = (2.25, 2.5)$ in the Gaussian initial condition (1.1), with also the natural frequency (black, dashed) equal to the particle mass of $\sqrt{2}$ (in units of $|m|$) in the classical system.

An illustration of the oscillation frequency in figure 3.3 contrasts the typical oscillon evolution from a particular, Gaussian initial condition (1.1) in both the classical (blue) and quantum (red) case.

This classical configuration evolves to a slowly increasing oscillation-frequency with the oscillon persisting throughout the simulated period. The mass of the particle-like excitation for the classical system importantly determines the natural frequency. This equals to $\sqrt{2}|m|$ (figure 3.3, black line) for the chosen quartic potential (see the equation (2.1)). The classical frequency notably re-

mains smaller than this natural frequency throughout the entire period. This case, thus, demonstrates the behaviour typical of the stable phase in the classical evolution (see Section 1.2.2 for details).

In the quantum case, the oscillon similarly evolves to a slowly increasing frequency (again smaller than the classical, particle-like mass), although the exact value is lower than the classical oscillations. The natural frequency of the oscillon subject to the quantum perturbations is uncertain. Nonetheless for the perturbation correlator almost equal to the vacuum value at the end of the simulation and with the application of the renormalization scheme, the mass of the particle excitation in the quantum case will approximately equal the classical mass. Thus, the threshold at the classical particle-mass of $\sqrt{2}$ (figure 3.3, black line) is likewise a significant bound in the quantum case, bounding the frequency of the oscillon.

The stage shortly before the classical oscillon decays through the inflection-point in the potential accompanies an abrupt change from below to above the radiation frequency (see Section 1.2.2) – for the current system, the frequency would expectedly increase rapidly from less to more than the particle-like mass of $\sqrt{2}$. This forms a distinctive endpoint to the classical configuration. In contrast, the quantum case shown in the figure 3.3 passes through the classical inflection-point when $\bar{t} \approx 460 |m|^{-1}$. Examining the frequency around this time reveals no dramatic transition. The frequency continues in the gradual increase below the particle mass with this increase only changing to be slightly more irregular when $\bar{t} \approx 600 |m|^{-1}$.

This change occurs around a duration equal to the crossing time ($\bar{t}_c = 204.8 |m|^{-1}$) of the lattice and after the oscillon is expected to have decayed. The increased irregularity, therefore, likely corresponds to the radiation produced on the collapse of the oscillon, having crossed the periodic boundaries and reached the former centre of the oscillon.

Examining the oscillation evolution over the entire lattice-plane confirmed

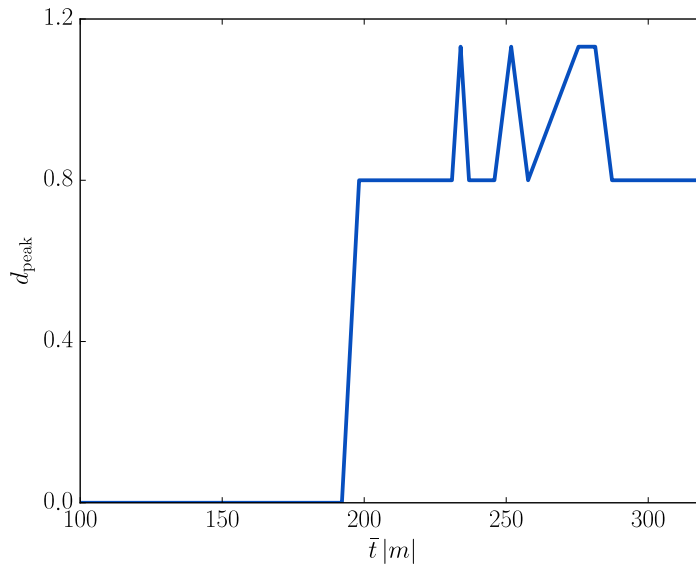


Figure 3.4: The distance d_{peak} (in the scaled coordinates) from the origin to the extrema of the oscillon evolution, evaluated when the core value $\Phi(t, \mathbf{0})$ is also an extremum. This stage in the core evolution provides the time expectedly corresponding to a (global) extrema of the oscillon configuration. The extrema of the oscillon are shown throughout the main evolution of the configuration, during the time $\bar{t} = 100 |m|^{-1}$ to $\bar{t} = 320 |m|^{-1}$ for the quantum case examined in frequency space – evolving the Gaussian initial condition (1.1) where $(A_0, r_0) = (2.25, 2.5)$. This confirms the oscillon remains relative static near to the origin on the lattice compared to the initial, characteristic width of the profile.

that the change in the amplitude at the origin occurred in the peak value of the oscillon. The figure 3.4 shows the distance (in the scaled coordinates) from the origin to the extrema in the oscillon, when the core-value $\Phi(t, \mathbf{0})$ is an extremum. For a pure oscillon configuration around the origin, the extrema of the core values may precisely determine when the oscillatory configuration also forms a global extremum. The radiation (generated through the decay of the configuration), though, complicates the oscillon evolution on the periodic lattice. This radiation expectedly contain much less energy than the oscillon throughout the main

evolution of the oscillations and, hence, are expected to only negligibly alter the extrema of the oscillations. The waves, further, only infrequently cross the core of the oscillon, on travelling through the periodic volume. This implies the radiation may only infrequently alter the oscillon extrema, and likewise infrequently may disrupt the correspondence between the core and global extrema⁴.) The extrema of core value therefore provide a reasonable estimate of when the extrema in the oscillations occur. Measuring the length from the origin to the extremum of the oscillon in these instances thus determines any change in the central position of the configuration. This, importantly, involves no gradual shift, which could potentially generate the gradual decrease noted in the core value throughout the evolution. The position of the oscillation extrema, moreover, confirm the central extremum of the oscillon remains close to the origin on the lattice, compared to the initial, characteristic width of the profile. This, hence, confirms the core field values ($\Phi(t, \mathbf{0})$) provides a reasonable indication of the evolution of the oscillon amplitude.

The continual increase in frequency at the origin (before the later irregularities), therefore, genuinely characterizes the oscillon amplitude. This gradual change without any distinctive indicator when the oscillon decays notably matches the ambiguity in the endpoint defined through the field amplitude. The oscillation envelope therefore provides a measure, equally suitable to any measure involving the frequency, for defining the decay of the quantum oscillon.

⁴The radiative waves superimposed on the oscillon profile may alter the resultant extrema of the oscillations, and also disrupt the correspondence between the core extrema and the oscillon extrema. This radiation will begin to affect central region of the oscillon profile around the origin after approximately the lattice crossing time. The seeming peaks in the distance (d_{peak}) to the extrema, after this time likely correspond simply to waves crossing the oscillon and consequently shifting where the peak in the oscillon configuration occurs. While the energy in the radiation is much less than the energy in the oscillon, the wave amplitude correspondingly will be much smaller than the oscillon amplitude. This, therefore, assures the neglect of the waves provides a reasonable approximation throughout the majority of the oscillon evolution. The much larger size of the lattice compared to the oscillon radius, also, indicates the radiation will cross the oscillon only infrequently. This further validates the neglect of the waves on the extrema of the oscillations. The low crossing frequency likewise implies the waves only infrequently alter the core value and hence assures the infrequent disruption of the correspondence between the core and the global extrema of the configuration.

3.7 Determining Oscillon Lifetimes

The categorization of the evolution types and the definition of the oscillon endpoint allow a consistent determination of the oscillon lifetimes over both the classical and quantum initialization space.

An illustration of a classical oscillon in figure 3.1 (top, left) shows the typical stability of the oscillations around the positive (broken-phase) minimum over the simulation. The envelope never decreases below or nears the inflection-point; and hence a slight modification in the precise definition of the endpoint creates no change in the detection of the oscillon.

The characteristic quantum-oscillon in figure 3.1 (bottom, left) shows the gradual decay in amplitude. This implies the precise lifetime will depend on the defined field-value for the endpoint. Nonetheless, a slight shift in the value defining the decay point only slightly alters the lifetime due to the gradual decrease of the envelope. The altered endpoint would, further, produce a change to the lifetime similarly in each case. This hence assures the differences between the lifetimes would remain largely unaltered.

The definition of the oscillon endpoint is thus robust for both the classical and quantum systems.

Additionally, the distinctive variants in the quantum system demonstrated (in the previous section) that the strong beat-frequency distinguishes that the oscillations have decayed in actuality when the envelope first crosses below the classical point of inflection. This endpoint importantly is largely unchanged (figure 3.2, left) in the high-resolution simulations eliminating the unphysical modulation. The first modulated oscillation at an amplitude below the classical point of inflection thus provides a reliable definition of the endpoint in such cases.

Those cases where a small, physical beat-frequency modulates the oscillations equally signify the decay to arise when the envelope first decreases below the classical inflection-point (figure 3.2, right). Again, the position where the net,

modulated field-amplitude first decreases below this threshold suitably defines the endpoint.

These definitions, notably, in the case of beat-frequencies involve the net, modulated field, although the instant where the envelope decreases below the inflection may define an equally valid endpoint. This poses an ambiguity in the oscillon lifetimes evaluated through the alternative methods. These variable definitions (in each case) though involved only minor differences compared to the computed lifetimes.

The changing in the beat-frequency on varying the lattice spacing also may alter the instant when the net, modulated-field amplitude decreases below the inflection point. These differences in each cases examined at differing lattice spacings, though, were negligible compared to the oscillon lifetime.

This consistency in the obtained values (at differing lattice spacings and for distinct definitions) therefore ensures the choice to examine the net, modulated field forms a robust quantity to determine the lifetime.

These small-amplitude beat-frequencies further generate oscillations of the net field around the inflection classical point over a period. This creates an ambiguity in precisely defining the endpoint of the oscillon. The choice to define the first instant when the oscillation amplitude decreases below the inflection-point to be the endpoint thus creates a systematic error compared to the alternative crossings of either the net field or the envelope. Nonetheless, the chosen crossing provides consistency in the definition over the entire parameter-space, and the variation from choosing the alternative points for the cases examined (compared to the calculated lifetime) were minor.

3.8 Mapping the Attractor Basin

Applying the defined endpoint to the oscillons over the parameter space of Gaussian initial conditions (1.1) reveals the classical (figure 3.5) and quantum (figure

3.7) basin of attraction.

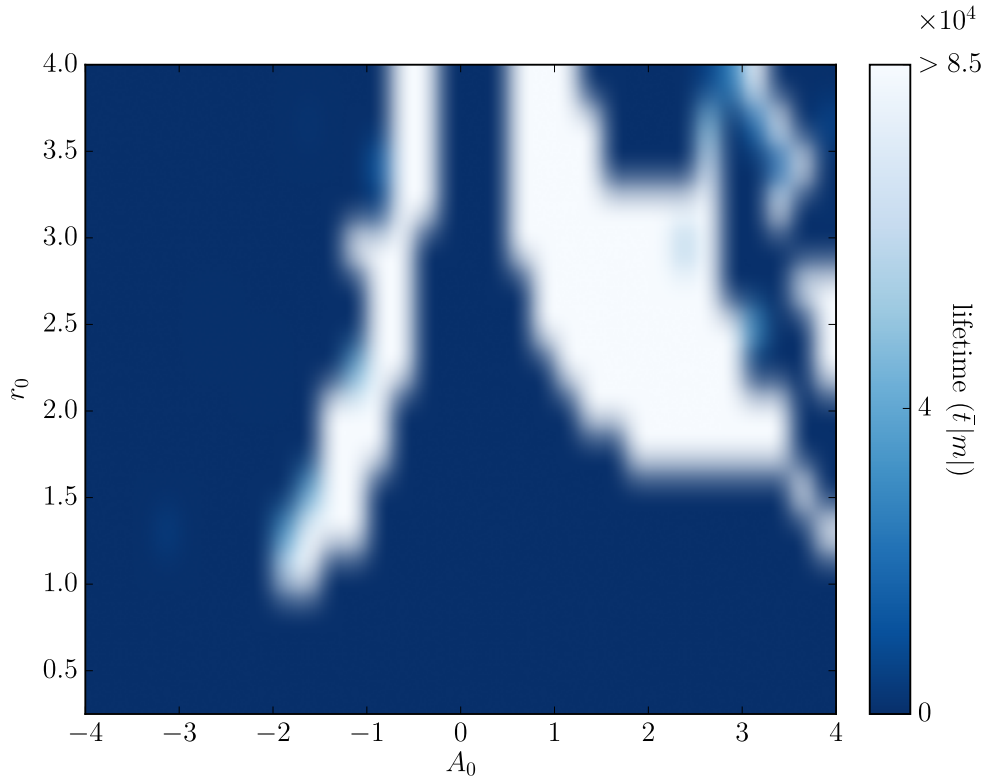


Figure 3.5: The lifetime of classical oscillons projected onto the parameter space of Gaussian initial conditions (1.1).

The classical case shows oscillons arise from the Gaussian initial conditions in two main regions: over a broad section of the positive-amplitude configurations and in a narrower range of the negative amplitudes. These are separated by a band of instability failing to generate oscillons around a zero amplitude. A minimum initial width, thus, bounds these regions, defining the minimum size (and corresponding minimum-energy) necessary for generating an oscillon.

These classical oscillons last at least $\mathcal{O}(10^4 |m|^{-1})$ and have not decayed before the end of the simulation, confirming previous observations [42–44, 46, 52].

This bifurcated attractor basin presents a potentially misleading illustration. In actuality, the oscillons of a positive initial amplitude oscillate to values above

the vacuum, corresponding to a negative-amplitude initialization (see Section 2.1.3); and vice-versa. The initial configurations in the positive and negative regions thus form – although in a non-trivial manner – related pairings.

Examining the energy of the Gaussian configurations, at least in the classical case, offers a method to establish an approximate relation between the positive and negative-amplitude initial conditions. Constructing the classical Hamiltonian of the action (2.1) and applying the field scaling (2.4) yields

$$H(t) = \frac{m^2}{\lambda} \int d^2\mathbf{x} \left[\frac{1}{2} \sum_{\mu} (\partial_{\mu}\phi(t, \mathbf{x}))^2 - \frac{c^2}{2\hbar^2} \phi^2(t, \mathbf{x}) + \frac{1}{4\hbar^2} \phi^4(t, \mathbf{x}) + \frac{c^4}{\hbar^2} \right]. \quad (3.1)$$

Substituting the initial, Gaussian configuration (1.1) and the choice of zero momentum into the classical Hamiltonian and evaluating the integral hence determines

$$H = \frac{1}{2} A_0^2 r_0^2 - \frac{1}{3} A_0^3 r_0^3 + \frac{1}{16} A_0^4 r_0^4. \quad (3.2)$$

This provides a precise expression of the initial energy for the classical configuration. The reasonably accurate approximation of the Gaussian to the true oscillon configuration (see Section 1.2.1 and 3.5) implies that this expression also remains a close approximation to the energy of the subsequently evolving oscillon at the maxima of the amplitude, where the field momentum again equals zero. Only a small change in the radius of the oscillons typically occurs throughout their evolution [36, 42]. This therefore indicates configurations of a positive, initial amplitude A_0 may oscillate to an approximately Gaussian configuration of an identical radius but a negative A_0 at the maximum of the oscillation, where the maximum amplitude corresponds to a configuration of equal energy to the initial Gaussian. The configurations of a negative initial amplitude may, likewise, evolve to a minimum amplitude of equal energy to the initial configuration. This, thus, indicates an equivalence in the classical evolution of the positive and negative initial amplitudes.

Examining the contours of equal energy in the parameter space of the Gaus-

sian configurations (figure 3.6) demonstrates that large ranges of positive amplitudes match to much smaller ranges of negative amplitudes, and the equal ranges gradually change to more negative amplitudes at smaller radii. The range of positive and negative initial-amplitudes at a fixed radius, generating classical oscillons (figure 3.5) closely matches these energy contours. This confirms the set of positive amplitudes generating oscillons closely corresponds to the negative-amplitude configurations of an equal radius and initial energy.

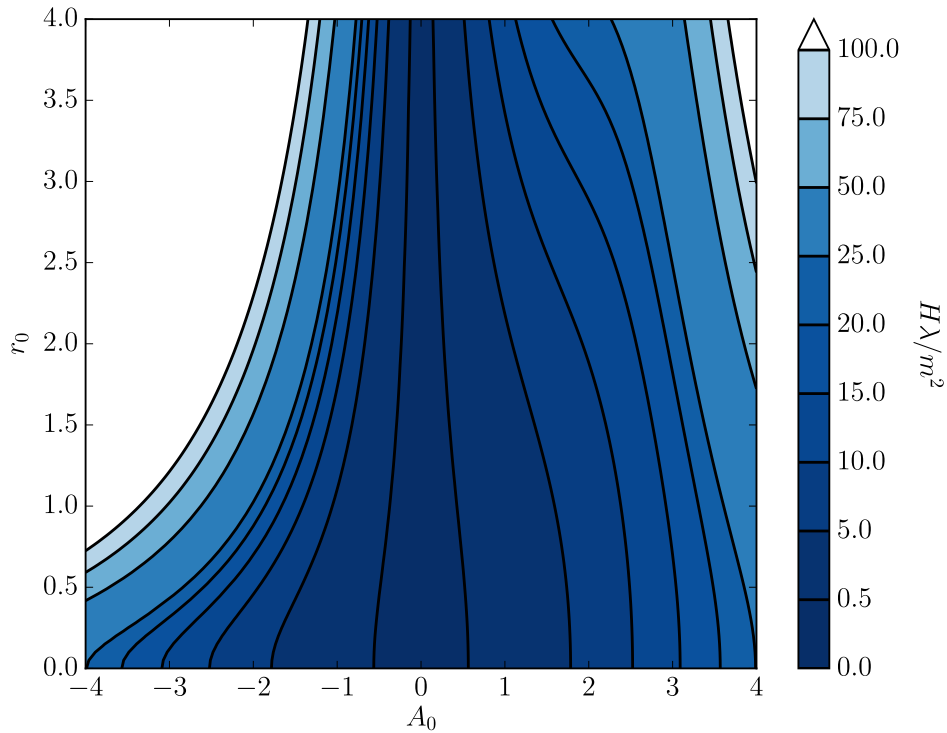


Figure 3.6: The contours of equal energy for the Gaussian initial conditions (1.1) with zero momentum. This illustrates the highly similar structure in the range of the positive and negative, initial amplitudes (A_0) at fixed radius (r_0), to generate classical oscillons (figure 3.5).

Quantizing the Hamiltonian (3.1) in the Hartree approximation yields quantum corrections to the classical expression. These modifications equal zero in the vacuum state and, thus, the classical result for the energy (3.2) remains valid at

the initial time in the quantum case. The quantum corrections in the subsequent evolution, in general, though are non-zero, and thus the classical result is invalidated at later times. (Calculating the corrections would involve obtaining the correlators of the quantum perturbation and hence poses an equivalent difficulty to the challenge of solving the quantum dynamics. Neither is a suitable analytic approximation readily attainable to examine the quantum corrections.) This purely quantum modification, thus, eliminates the simple, classical equivalence of each initial, positive-amplitude configuration to the Gaussian of corresponding negative amplitude but equal energy, and vice versa. The stronger difference between the Gaussian and the true oscillon configuration (Section 3.5) in the quantum case, further, indicates that the energy evaluated for the Gaussian field configuration (1.1) provides a poorer estimate of the actual energy on the evolving quantum oscillon. This again invalidates the simple, classical equivalence between the evolution of the positive and negative amplitudes. The positive, initial amplitudes generating oscillons, nonetheless, evolve to a state of amplitude above the vacuum, equal to a negative, initial amplitude (see Section 2.1.3), and vice versa. A careful examination of the initial maximum and minimum (immediately subsequent to the initial transient) might enable more precisely matching the positive and negative initial amplitudes evolving to equivalent configurations. This is unnecessary though for examining the quantum effects on the oscillon lifetime. The assured equivalence in the evolution of the positive and negative initial amplitudes implies that the positive initial conditions, thus, incorporate the entirety of quantum oscillon-evolution. Examining the positive region, therefore, provides a sufficient range of amplitude to fully assess the quantum effects on the oscillon lifetime.

The figure 3.7 illustrates the quantum equivalent to the classical evolution in the figure 3.5, except across the restricted range in Gaussian initial conditions. Oscillons in the quantum case arise over a largely similar region of the Gaussian parameter space to those in the classical case (white lines, 3.7). In particular,

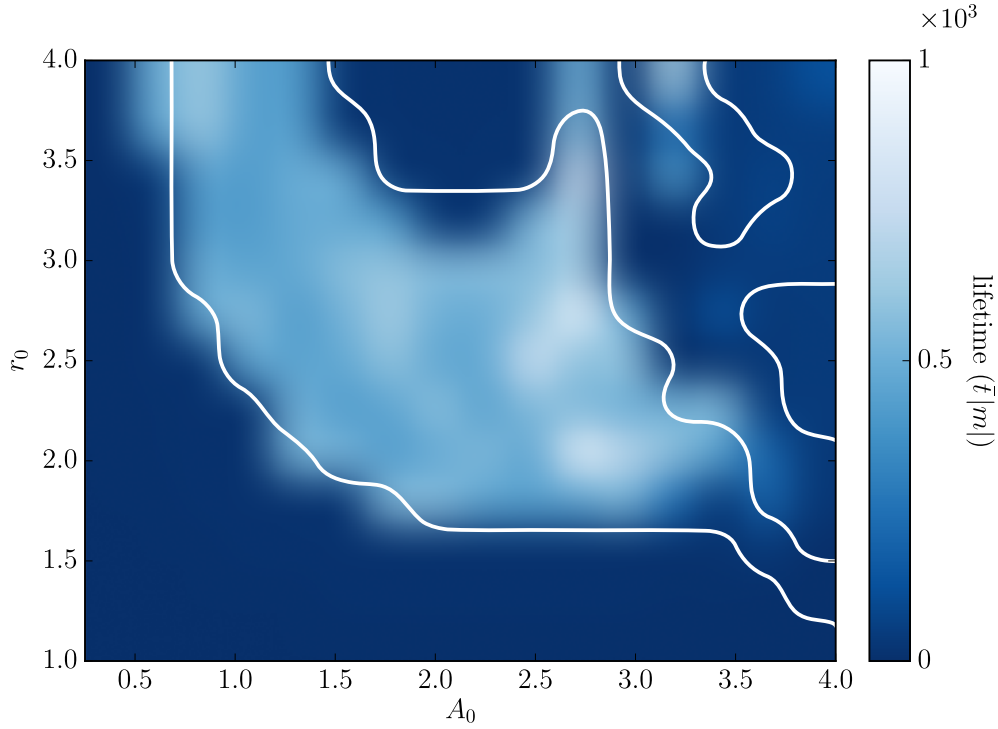


Figure 3.7: The lifetime of quantum oscillons projected onto the parameter space of Gaussian initial profiles (1.1). The white contours indicate the classical basin.

a band for amplitudes below a value around the inflection-point generates no oscillons; and a minimum radius also bounds the attractor-basin threshold. The quantum perturbations, though, alter the precise bounds of the attractor basin from the classical case. Most significantly also, these oscillons, subject to the quantum fluctuations, persist for considerably less time than the classical counterparts: typically ending before $\mathcal{O}(10^3 |m|^{-1})$.

3.9 Conclusion

These results have shown the first quantum, dynamical simulations of oscillons. These demonstrated that (with $\hbar = c = \lambda/m = 1$) the quantum fluctuations significantly reduced oscillon lifetimes compared to the classical case. Further, the decay under the quantum evolution occurs gradually, without distinctive

change in either the oscillation amplitude or frequency. This markedly contrasts the classical oscillons. The detailed decay-process, though, remains unclear.

Conducting the comparison of the Gaussian attractor basin (for positive, initial amplitudes) showed that both the classical and quantum oscillons result in a similar region of the parameter space – despite the distinctly differing evolution and lifetimes. This indicates that, at least initially, the purely classical terms in the potential – the terms present in both cases – dominate the formation of oscillons. The stronger, initial decay in the amplitude of the quantum oscillons, in contrast to the classical case, implied that the quantum back-reaction alters the oscillon configuration. Those configurations creating an oscillon, thus, react to the quantum fluctuations. The progression after the initial transient to a comparatively stable phase, similar to the classical case, indicates that the classical components of the potential dominate during this early phase of the evolution; and the quantum fluctuations predominantly alter the later decay.

These quantum, dynamical simulations have been accomplished through applying the inhomogeneous Hartree approximation to solve the equations of motion on a two-dimensional lattice. The construction of a statistical ensemble of fields was used to approximate the quantum correlators. These fields are of the form

$$\varphi_n(t, \mathbf{x}) = \int \frac{d^2\mathbf{k}}{(2\pi)^2} [c_{\mathbf{k},n} f_{\mathbf{k}}(t, \mathbf{x}) + c_{\mathbf{k},n}^* f_{\mathbf{k}}^*(t, \mathbf{x})], \quad (3.3)$$

where the random numbers $c_{\mathbf{k},n}$ are chosen to reproduce the ladder-operator correlators. The statistical mean of these ordinary numbers in effect replaces the quantum average of the operators in the system. This hence determines the variance of the ensemble fields may replace the quantum correlators in the dynamics:

$$\langle \varphi_n(t, \mathbf{x}) \varphi_n(t, \mathbf{x}) \rangle_E \longrightarrow \langle \delta \hat{\phi}(t, \mathbf{x}) \delta \hat{\phi}(t, \mathbf{x}) \rangle. \quad (3.4)$$

Requiring each ensemble field to satisfy the mode dynamics (2.14) implies that the constructed equation effectively evolves all the mode functions simultaneously

within the ensemble field. This ensures the variance of the ensemble fields (with the correct choice of the random numbers) corresponds to the quantum correlator at all times. Establishing this equivalence, thus, forms the basis to examine the quantized dynamics through the ensemble fields.

The ensemble method, in principle, involves infinitely many fields for a precise equivalence between the quantum correlator and the statistical variance. In practice, the use of a finite ensemble size to accurately approximate the exact quantum value offered the possibility to reduce the computational requirements compared to evolving the mode functions. This method, though, for the quantum dynamical simulations of the oscillon provided negligible computational benefit. The tests demonstrated the need for an ensemble size of $M = 60000$ to obtain sufficient convergence in the fields. On the square lattice of $N = 256$ point, this was only marginally fewer fields than the $N^2 = 65536$ modes required in the mode function method.

This result contrasts the use of the ensemble method in the quantum, dynamical simulations of Q-Balls [13] in $3 + 1D$. These only required an ensemble size less than one tenth of the total modes on the lattice. The oscillon case likewise contrasts the $2 + 1D$ simulations of domain walls [8]. These also required a consistently smaller ensemble size compared to the mode functions. This discrepancy demonstrates the exceptionally difficult nature of examining oscillons in the quantum regime. The strongly inhomogeneous nature of the oscillon likely creates the need for a large ensemble to accurately examine the quantum dynamics of the (highly non-perturbative) configuration. Obtaining the oscillon lifetimes also involved the examination of the field evolution directly, without any averaging – unlike in the domain wall case – to potentially help reduce any statistical fluctuations. This might necessitate considerable accuracy in the approximation of the ensemble to the quantum correlators, and accordingly requires a large ensemble size.

The comparable size of the ensemble to the number of modes notably matches

the results in $1 + 1$ D simulations applying a statistical ensemble to compute the quantum, fermion correlators [74]. This may indicate that the low dimensionality of the oscillon simulations also results in the inefficiency of the ensemble method for examining the quantum scalar-field. Implementing the ensemble method might therefore provide a significant increase in the computational efficiency for similar investigations in three and higher dimensions.

Chapter 4

Introduction: Fermions

The preceding discussion and the detailed investigation into oscillons have primarily concerned bosonic fields. A comprehensive understanding of quantum fields though must also incorporate fermionic degrees of freedom.

Their inherently quantum nature prevents any classical approximation providing an accurate treatment, and accordingly analysing fermions is problematic. Perturbation theory provides a powerful technique for understanding fermionic fields and ultimately establishing their central role within the Standard Model of particle physics: Quantum Electrodynamics provides a principal component in the current, foremost theory for explaining fundamental physics [75].

Various contexts of potentially fascinating and relevant consequence involve fermions in an inherently non-perturbative regime. The consequent effects in several important cases will be examined in this chapter, where the discussion will consider the results in relation to the methods for solving the systems. Incorporating both the quantum and the non-perturbative nature in the analysis poses a considerable challenge. The examined applications of these methods though demonstrate the importance of solving such difficult systems, to obtain a comprehensive and accurate understanding. An overview of the techniques for examining fermionic systems will presently form the introductory discussion to the various applications. These methods, in particular, will ultimately be

exploited for analysing quantum tunnelling in an idealized laboratory scenario.

4.1 Solving Fermion Dynamics

The Dirac equation provides the basis for understanding fermions:

$$\left(\gamma^\mu D_\mu + \frac{mc}{\hbar}\right)\Psi(x) = 0. \quad (4.1)$$

This strikingly simple equation, remarkably, determines various important features of fermions [76]. The equation may be constructed essentially on attempting to obtain field dynamics also satisfying relativistic, Lorentz invariance [75, 77]. This condition producing the Dirac equation inherently determines the spin-half nature of fermions [77]. The equation, importantly, also implies the existence of the negative-energy, anti-particle positrons [78].

Adding a fermion-gauge interaction through

$$i\frac{g}{\hbar}\bar{\Psi}(x)\gamma^\mu A_\mu(x)\Psi(x)$$

into the action for the Dirac equation, together with the terms for classical electromagnetism, produces the standard, quantum electrodynamics Lagrangian. This equally forms a remarkably simple basis for the analytical power to describe nearly all phenomena across macroscopic scales to 10^{-3}cm [75]. The (three-point) gauge-fermion interaction yields an inherently two-point correlator in the equations of motion and correspondingly the mode function method offers a convenient method to evaluate this contribution [75, 79]. This procedure (in contrast to the bosonic case) enables accurate evaluation of the fermionic effects without further approximation.

Implementing the mode expansion on the lattice, equivalently to the bosonic case, involves a summation over the discrete mode space. This process likewise for the fermions, on a d -dimensional lattice of N_L sites in each direction, entails

evaluating the functions for each of the N_L^d mode values in the summation. The problem is also moderately worsened in the fermionic case since the fermionic field comprises a four component spinor and the modes include both the particle and anti-particle contributions: creating a factor of eight in the total field components required for evolution. This N_L^d scaling equivalently to the bosonic case therefore implies that any case with $d > 1$ requires increasingly extensive computational resources.

Canonical quantization imposes an anti-commutation relation on the fermion fields. The ladder operators, on forming the mode expansion subsequently, encapsulate the anti-commutation structure; and, hence, the mode analysis to evaluate the correlators intrinsically also incorporates the anti-commuting properties. Simply substituting a single ensemble for the fermionic operator equivalent to the bosonic case, consequently, fails to reproduce the fermionic correlator. This single ensemble crucially involves only ordinary, commuting numbers excluding the possibility to represent the anti-commuting nature. Creating a second ensemble may resolve this problem [74, 80, 81]. The fields explicitly satisfy

$$\begin{aligned}\Psi_{M,c}(x) &= \sqrt{\frac{\hbar c}{2}} V_x \sum_s \int \frac{d^3 \mathbf{k}}{(2\pi)^3} \left(\xi_{\mathbf{k},s,c} \psi_{\mathbf{k},s}^{(U)}(x) + \zeta_{\mathbf{k},s,c} \psi_{\mathbf{k},s}^{(V)}(x) \right), \\ \Psi_{F,c}(x) &= \sqrt{\frac{\hbar c}{2}} V_x \sum_s \int \frac{d^3 \mathbf{k}}{(2\pi)^3} \left(\xi_{\mathbf{k},s,c} \psi_{\mathbf{k},s}^{(U)}(x) - \zeta_{\mathbf{k},s,c} \psi_{\mathbf{k},s}^{(V)}(x) \right),\end{aligned}$$

where $\{\psi_{\mathbf{k},s}^{(U)}\}$ and $\{\psi_{\mathbf{k},s}^{(V)}\}$ are the modes with $\{\xi_{\mathbf{k},s,c}\}$ and $\{\zeta_{\mathbf{k},s,c}\}$ independent sets of (complex) random numbers, and V_x is the total, real-space volume. These integrands, importantly, differ only in the plus or minus sign; these very similar counterparts are termed the “male” and “female” fields. The plus and minus signs ensure computing combinations of both the male and female fields may yield an integrand involving a sign difference between the term in the $\psi_{\mathbf{k},s}^{(U)}$ and that in the $\psi_{\mathbf{k},s}^{(V)}$ for a fixed wavevector. This, importantly, reproduces the structures resulting on applying the anti-commutator relation of the ladder-operators,

unattainable if only using a single ensemble.

A judicious choice of the random numbers (as in the bosonic case) may, hence, ensure these combinations of male and female fields precisely reproduce the quantum correlator. Choosing the random numbers in particular to form a Gaussian random distribution proportional to the ladder anti-commutators [74, 80, 81] implies

$$\langle T\hat{\Psi}(x)\hat{O}\hat{\Psi}(x) \rangle = -\langle \bar{\Psi}_M(x)\hat{O}\Psi_F(x) \rangle_E = -\langle \bar{\Psi}_F(x)\hat{O}\Psi_M(x) \rangle_E,$$

for \hat{O} an arbitrary operator. (The male and female fields thus notably perform an interchangeable role, and in practice the quantum correlator may be constructed through the average of these symmetric expectations.) These Gaussian distributions create the evident difficulty, also present in the bosonic case, of requiring an infinite ensemble; and this problem is worsened in the fermionic case through the additional requirement to evolve two ensembles, both infinite. The method in practice, though, equivalently to the bosonic case, might reproduce the correlators to a sufficient accuracy when the total number of both the male and female fields is smaller than the mode space: thus, reducing the computational requirements required, compared to the standard, mode evolution.

This ensemble method for fermions has demonstrated an exceptional effectiveness in examining the fermionic back-reaction on classical, scalar-field oscillons [80]. The computations uncovered an exponential decay in the total oscillon-number starkly contrasting the slow, power law decay in the absence of fermions for the ensemble size only around one hundredth of the total lattice sites.

A 1 + 1D system to examine charge-parity (CP) violation within an Abelian-Higgs model carefully determined the variation in ensemble size to produce convergence in the results only for an ensemble larger than the total lattice-sites [81]. This analysis though proved the reliability of the method for examining CP

violation – the fermion number accurately approximating the dynamical Chern-Simons number characterizing the gauge fields and thus satisfying the theoretical expectation. A further study examined CP-violation in a 3 + 1D system for the SU(2)-Higgs fields [74]. The ensemble method provided sufficient accuracy to examine the particle production for the ensemble sizes typically around a third to a tenth of the total sites (N_L^3) on the lattice.

These systems thus demonstrate the potential for the ensemble method for fermionic fields to detriment computational efficiency in 1 + 1D but provide a benefit in 3 + 1D. The significant enhancement for the case involving fermionic back-reaction onto oscillons further examined a 2 + 1D space. This thus further supports the ensemble method for fermions provides benefit only in higher than 1 + 1D.

4.2 Fermions on the Lattice

Naively discretizing the fermion dynamics onto the lattice creates the familiar “doubler problem”. This phenomenon involves $2^4 = 16$ fermion species – each with two charges and two spin states – occurring on the lattice and these unphysical particles potentially contributing pronounced lattice-artefacts. A variety of methods may help to alleviate the spatial doublers including most notably Wilson fermions [82] and also staggered fermions [83, 84] or Ginsparg-Wilson fermions [85]. The Wilson Fermion methodology may, equivalently, ameliorate the temporal doublers; a judicious choice of the initial conditions with a sufficiently small time-step, alternatively, may suppress the presence of temporal doublers [82, 86].

This problem of doublers on the lattice results, essentially, through the fermion evolution involving the solutions to a first-order differential equation. The basic origin of the doublers may be most readily examined on considering a homogeneous, first-order differential equation of a one-dimensional function:

$$\partial_{x_1} f(x_1) = 0.$$

Each component of the fermionic spinor notably satisfies (dependently) an equation of this type on applying the Dirac equation (4.1) for massless fermions ($m = 0$) in either a homogeneous system or, equivalently, in the static state of a 1 + 1D system.

This first-order equation, in the continuum, implies only a single, possible solution, where f equals a constant. Forming the standard, symmetric¹ discretization of the first-order derivative (see equation 2.27) yields

$$\frac{f(X_1 + 1) - f(X_1 - 1)}{\Delta x_1} = 0.$$

This forms the equivalent field equation on the lattice to the continuum, first-order equation. The lattice expression, importantly, involves the field evaluated, rather than at consecutive intervals, two intervals apart. This, hence, implies the even intervals may satisfy one solution, $f(2n_1\Delta x_1) = C_1$ and the odd sites may satisfy an independent solution $f((2n_1 + 1)\Delta x_1) = C_2$, for integers n_1 and where C_1 and C_2 are constants. The solution matching the continuum result, thus, reproduces the continuum dynamics on the lattice, while the alternative solution forms a solution unique to the lattice. This result, an artefact of the discretization, thus, encapsulates the origins of the doubler in the fermionic system.

Examining the fermionic propagator and the corresponding excitation-energy spectrum, more formally, demonstrates the existence of these doublers on the lattice in 3 + 1D (for a detailed discussion see for instance [86]). Forming the naive discretization of the Dirac equation (4.1) on the lattice may yield the free-

¹An asymmetric approximation to the first derivative may also be formed, involving function the field at the chosen point $f(X_1)$ and either of the consecutive intervals: $f(X_1+1)$ or $f(X_1-1)$. Using this asymmetric form would, importantly, invalidate the basic explanation for doublers. The symmetric derivative, though, provides both the more accurate discretization on the lattice and also retains the isotropic nature of derivative through not incorporating any directional preference. This therefore forms the more desirable choice of discretization on the lattice. The examination of the symmetric form, moreover, provides an intuitive insight the basic structures in the lattice theory generating the doublers. Examining the fermionic propagator, may more rigorously, demonstrate the existence of the doublers – this process is outlined, subsequently, in the case of fermions in 3 + 1D.

fermion propagator in wave-vector space:

$$S(K) = \frac{\frac{mc}{\hbar} - i \sum_{\mu} \frac{1}{\Delta x_{\mu}} \gamma^{\mu} \sin(K_{\mu} \Delta x_{\mu})}{\left(\frac{mc}{\hbar}\right)^2 + \sum_{\mu} \frac{1}{(\Delta x_{\mu})^2} \sin^2(K_{\mu} \Delta x_{\mu})}, \quad (4.2)$$

for the fermion mass m and the wavevector K (with components K_{μ}) on the lattice. Subsequently integrating the temporal wave-vector component explicitly yields the time dependency of the propagator. The resultant expression includes two terms: both the usual time-evolution factor in the continuum and a further term involving a rapidly oscillating factor $(-1)^t$. This indicates the presence of the second temporal-species on the lattice and the corresponding rapid-oscillations in time. These oscillations in practice are typically evident in the physical variables oscillating between extrema on successive timesteps – and superimposed on the physical variation corresponding to the continuum evolution.

Setting the initial conditions to purely the discrete equivalent of the continuum configuration ensures initially only the physical particles are present. Ultimately, energy transfer may create the temporal doublers in system. Typically though for sufficiently small lattice-spacings, this doubler production is heavily suppressed throughout the simulation and hence prevents the distinctive oscillatory disturbance. This method, accordingly, will provide the mechanism to prevent the temporal doublers within the subsequent computations.

The integration of the propagator (4.2), further, determines the energy spectrum of the naively discretized Dirac equation:

$$\sinh\left(\frac{\omega \Delta x_0}{c}\right) = \Delta x_0 \sqrt{\left(\frac{mc}{\hbar}\right)^2 + \sum_i \sin^2(K_i \Delta x_i)}.$$

A particle state corresponds to a local minimum in the energy surface. The spectrum, hence, implies that the naively discretized system involves 2^3 fermion species. These further subdivide into those corresponding to the usual time

variation in the continuum and the temporal-doublers. This, hence, amounts to the final count of 2^4 fermion species in the naively discretized system. The 2^3 spatial variants, significantly, include both particles with a mass corresponding to those particles in the continuum theory but also additional particles, forming the spatial-doublers in the naive discretization.

Implementing instead the Wilson fermions on the lattice will provide the method to eliminate the spatial doublers in the subsequent simulations. This procedure involves adding a Wilson term to the action:

$$\frac{1}{c} \int c dt d^3 \mathbf{x} \frac{r_w}{2} \sum_i \Delta x_i \bar{\Psi}(x) D_i D_i \Psi(x),$$

where $D_i \Psi(x) = (\partial_i - (iq/\hbar) A_i(x)) \Psi(x)$. This additional term notably reduces to zero in the continuum limit to recover precisely the Dirac fermions; but on the lattice, the term importantly modifies the energy spectrum. Setting the Wilson parameter $r_W = 1$ essentially modifies the higher momentum modes to entirely remove the energy degeneracy and produces a single energy-minimum corresponding to the continuum particle state. Choosing the Wilson parameter $r_W < 1$ may still create doublers corresponding to local energy minima (for a detailed examination in $1 + 1$ see also [76]); but if the modification to the energy spectrum increases the energies to high values this may help prevent exciting these unphysical particles.

The spatial doublers equivalently to the temporal doublers generate spatial oscillations in the physical observables on the lattice-spacing scales. Selecting the Wilson parameter to adequately limit these oscillations in practice provides a sufficient method to choose the parameter value. The absence of the characteristic spatial oscillations therefore will sufficiently validate the chosen $r_W < 1$ in the subsequent simulations.

4.3 Quantum Tunnelling

Examining the potential for quantum interactions to generate tunnelling of a particle through a potential barrier will form the essential context for implementing numerical simulations of fermions in the subsequent sections. Tunnelling through a potential barrier, in general, is a distinctly quantum phenomenon. The paradigmatic case occurs in quantum mechanics, for a particle classically confined by a potential barrier of finite strength [87]. Where the energy of the particle is less than the potential barrier, the particle classically is unable to move through the barrier. In quantum mechanics though, the location of the particle is determined through a wavefunction satisfying the Schrödinger equation. The wavefunction decays through the barrier but is non-zero, implying a finite probability for the particle to traverse the barrier. Continuity at the boundaries further constrains the wavefunction in the free space, outside the classically allowed region to be finite. The result hence implies a finite probability to observe the particle within the classically forbidden region. This process occurs also in accordance with the Heisenberg Uncertainty Principle [87]. The constraint on the uncertainty in measuring both the position and the momentum of the particle precludes a zero probability to detect the particle; and thus determines the quantum system to involve this finite probability for observing the particle to have tunneled through the barrier. This phenomenon historically has explained radioactive decay [88, 89]; while also being applied practically in scanning tunnelling microscopes [90] and for everyday use in solid state memory [91].

Quantum field theory enables a second type of tunnelling. The quantum interaction between different particle species may enable the one kind to transmute into the second in an oscillatory species-mixing. A barrier may form a classically impenetrable obstruction to the original species while the second species may freely travel through this region. The generated particle having traversed the barrier may revert to the original species through the continuing quantum os-

cillations, and thus produce the tunnelling into the classically forbidden region. This process forms the basis of the standard “light shining through a wall experiments” typically proposed to detect either axions [92, 93] or similar light particles within the laboratory [94, 95].

The quantum field theory interactions enable a further mechanism for the particles to tunnel through a barrier. This generalization to the preceding mechanism involves the original species transforming through pair-creation into a second species able to travel through the barrier. These pair-created particles, on passing through the barrier, subsequently annihilate to (re-)create the original species. This “tunnelling of the 3rd kind” thus forms a distinct and purely quantum mechanism for particles to traverse a barrier [96–98].

The process may occur in a (generic) non-local, effective theory, where the tunnelling predictions hence form a test of the model. This may be the case, in particular [96], where an electromagnetic field traps a particle in a particular state, but an excited state of the atom may freely traverse the field.

Tunnelling of the 3rd kind also provides an alternative mechanism for the standard “light shining through a wall experiments” [97, 98]. The photons may encounter an opaque surface where they split into mini-charged fermions. For the charge sufficiently small, the fermionic particles only weakly interact with the opaque material. This essentially enables their free propagation through the barrier. The fermion particles and anti-particle pairs subsequently annihilating to photons again after traversing the barrier, thus, completes the tunnelling process. Where this process occurs within a uniform magnetic field, the transmission signal may be significantly enhanced to detect the signal within a laboratory setup [97]. This offers a practical method to test the mini-charged particle extensions to standard particle physics.

A uniform magnetic field external to an enclosed superconducting region forms a variant to the standard light experiment for testing the existence of mini-charged particles [98]. The magnetic field converting into the mini-charged

fermions generates the tunnelling mechanism; while the superconductor although enabling transmission, nonetheless strongly suppresses the classical magnetic field within the barrier. This system thus provides the potential to test fundamental physics in the laboratory. The detection of the tunnelled particles may confirm the existence of mini-charged particles; or measurements may at least place constraints on these extensions to the standard model. Determining the size of the expected transmission and determining the regime where a distinctive tunnelling signal may be detected therefore poses an interesting topic for consideration. This process involves an inherently quantum interaction in an entirely non-perturbative system, and thus forms a suitable case to examine through quantum simulation on the lattice.

Examining the magnetic-tunnelling process within an idealized laboratory scenario will form the central aim in the technical developments following. The basic arrangement will involve two infinite, planar sheets positioned parallel and separated a short distance. These superconducting sheets thus divide the three-dimensional space into three regions: the enclosed space between the sheets and an external region to either side. The superconductors form the classical barrier to the uniform magnetic field in the external regions, while a classical, planar current within each external region (and parallel to the barriers) sources the external field.

A classical Higgs-field may model the superconducting barriers (see for instance [99]). Coupling the gauge field to this classical scalar generates a photon mass dependent on the scalar. Constructing the scalar to involve a large, localized field value may hence impede the photon propagation within this restricted region. The scalar field thus effectively forms a barrier to the magnetic transmission. Excluding also a direct coupling between the Higgs field and the fermion essentially enables the fermions to propagate through the barrier without a direct interaction. The resultant magnetic transmission into the enclosed region – comprising both the classically transmitted magnetic field and the tunnelled

particles – may hence determine the magnetic tunnelling.

This system further forms a suitable context for applying the simulation techniques devised for fermions. These will importantly provide the method for the non-perturbative examination in the full QED theory for the idealized laboratory scenario.

Chapter 5

Tunnelling of the 3rd Kind: Dynamical Setup

5.1 Continuum Dynamics

5.1.1 Action

We consider a fermionic field and Higgs field coupled to a $U(1)$ gauge field in 3+1 dimensions, Minkowski spacetime of positive signature:

$$S(x) = \frac{1}{c} \int c dt d^3\mathbf{x} \left[-\frac{1}{4\mu_0} F_{\mu\nu}(x) F^{\mu\nu}(x) - j_\mu(x) A^\mu(x) - \bar{\Psi}(x) \gamma^\mu D_\mu \Psi(x) - \frac{mc}{\hbar} \bar{\Psi}(x) \Psi(x) - \frac{1}{2} D_\mu \phi^\dagger(x) D^\mu \phi(x) \right],$$

with $\bar{\Psi} \equiv i\Psi^\dagger \gamma^0$, and where the coupling occurs through the covariant derivatives

$$\begin{aligned} D_\mu \phi(x) &= \left(\partial_\mu - i \frac{e}{\hbar} A_\mu(x) \right) \phi(x), \\ D_\mu \phi^\dagger(x) &= \left(\partial_\mu + i \frac{e}{\hbar} A_\mu(x) \right) \phi^\dagger(x), \\ D_\mu \Psi(x) &= \left(\partial_\mu - i \frac{q}{\hbar} A_\mu(x) \right) \Psi(x). \end{aligned}$$

The electromagnetic field tensor incorporates the standard (free) electric and magnetic fields while the second term in the action adds an external current into the dynamics for generating the electromagnetic fields. Massive fermions are incorporated in the fourth and fifth terms of the action, where the parameter m specifies the mass. The Higgs field, for modelling the barrier to the electromagnetic field, is included in the final term. This scalar and the fermion each interact with the gauge field through the couplings in the covariant derivative; though the action notably excludes a direct interaction between the Higgs and fermion field. The parameter e in the Higgs coupling specifies the Higgs charge; and likewise, q in the fermion coupling specifies the fermion charge.

This action, further, is invariant under the gauge transformation

$$\tilde{A}_\mu(x) = A_\mu(x) + \partial_\mu \lambda(x), \quad (5.1a)$$

$$\tilde{\Psi}(x) = \exp\left(i\frac{q}{\hbar}\lambda(x)\right) \Psi(x), \quad (5.1b)$$

$$\tilde{\phi}(x) = \exp\left(i\frac{e}{\hbar}\lambda(x)\right) \phi(x), \quad (5.1c)$$

thus forming a gauge freedom in the system.

For definitiveness, we employ the Weyl representation in the fermion algebra:

$$\gamma^0 = \begin{pmatrix} 0 & i\mathbb{I}_2 \\ i\mathbb{I}_2 & 0 \end{pmatrix}, \quad \gamma^j = \begin{pmatrix} 0 & i\sigma^j \\ -i\sigma^j & 0 \end{pmatrix}, \quad (5.2)$$

satisfying the anticommutator-relation

$$\{\gamma^\mu, \gamma^\nu\} = 2\eta^{\mu\nu}\mathbb{I}_4.$$

These imply, further,

$$\begin{aligned}\gamma_5 &= -i\gamma^0\gamma^1\gamma^2\gamma^3, \\ &= \begin{pmatrix} \mathbb{I}_2 & 0 \\ 0 & -\mathbb{I}_2 \end{pmatrix}.\end{aligned}$$

The fermion mass m will define the unit of mass in the subsequent simulations and likewise the Higgs-charge e will define the unit of mass. Both parameters will in practice, ultimately, therefore, be set to unity in the equations of motion, with the further physical variables implicitly expressed in relation to these quantities.

5.1.2 Higgs-Field Configuration

Expressing the Higgs field in exponent form

$$\phi = \rho(x) \exp(i\theta(x))$$

separates the field into its phase θ and modulus ρ and may reframe the Higgs term in the action into the form

$$\begin{aligned}-\frac{1}{2}D_\mu\phi^\dagger(x)D^\mu\phi(x) &= \\ &= -\frac{1}{2}\partial_\mu\rho(x)\partial^\mu\rho(x) - \frac{1}{2}\rho^2(x)\left(\partial_\mu\theta(x) - \frac{e}{\hbar}A_\mu\right)\left(\partial^\mu\theta(x) - \frac{e}{\hbar}A^\mu\right).\end{aligned}$$

The gradient of the modulus entirely decouples in this expression from the phase and the additional fields in the system. This enables either added source terms in the action or equivalently a Lagrangian multiplier to fix the modulus to be static and without these constraints otherwise contributing to the dynamics; these additional terms may further cancel the static gradients. Thus for simplicity, the modulus may validly be considered static and the gradient-term neglected in the

dynamics, without examining the source terms imposing the constraints:

$$S = \int c dt d^3\mathbf{x} \left[-\frac{1}{4\mu_0} F_{\mu\nu}(x) F^{\mu\nu}(x) - j_\mu(x) A^\mu(x) - \bar{\Psi}(x) \gamma^\mu D_\mu \Psi(x) - \frac{mc}{\hbar} \bar{\Psi}(x) \Psi(x) - \frac{1}{2} \rho^2(x) D_\mu \theta(x) D^\mu \theta(x) \right]. \quad (5.3)$$

with $D_\mu \theta \equiv \partial_\mu \theta(x) - (e/\hbar) A_\mu$.

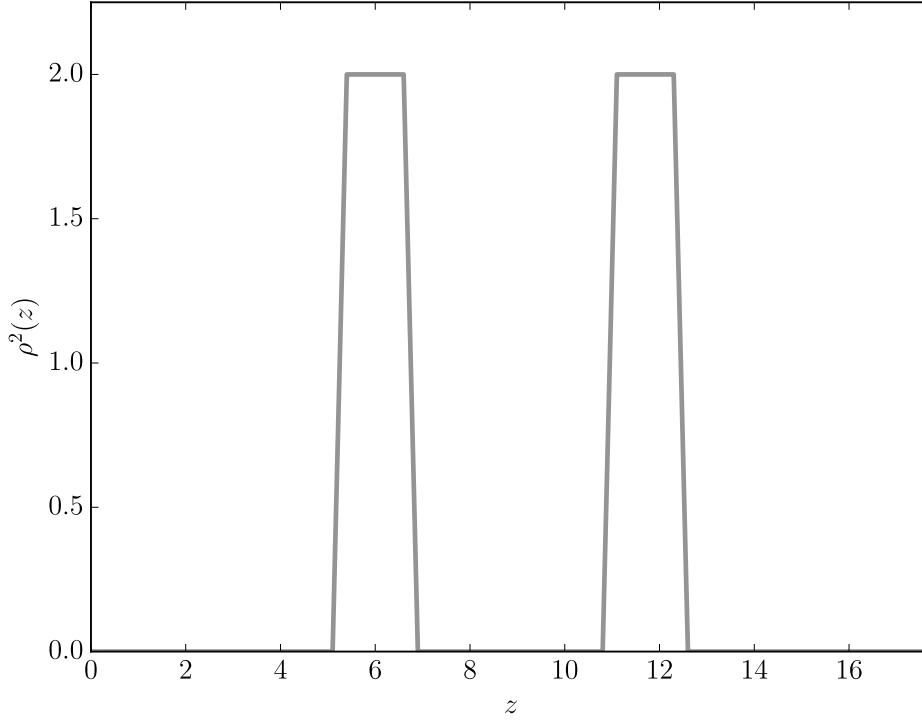


Figure 5.1: The typical form of the imposed Higgs modulus (5.4) for the structural parameters used in the subsequent simulations, where $S = 5.7$ and $d = 1.5$ with also $\delta < \Delta 3 = 0.3$ and $M = L_z/2 = 9$ determined on the choice of lattice size and spacing applied in the subsequent tunnelling simulations (see Section 6.5.1 and Section 6.5.2). This plots shows the field value in particular for $\eta = 1$.

Choosing the form of the static Higgs-modulus, ultimately, sets the position of the super-conducting barrier. The explicit form of the modulus imposed in

the simulations is

$$\begin{aligned} \rho^2(x) = \rho^2(x_3) \equiv & 2\eta^2 \\ & - \eta^2 \left[\tanh\left(\frac{x_3 + S/2 + d/2 - M}{\delta}\right) \tanh\left(\frac{x_3 + S/2 - d/2 - M}{\delta}\right) \right. \\ & \left. + \tanh\left(\frac{x_3 - S/2 + d/2 - M}{\delta}\right) \tanh\left(\frac{x_3 - S/2 - d/2 - M}{\delta}\right) \right]. \end{aligned} \quad (5.4)$$

This creates two sheets aligned perpendicular to the z -direction (figure 5.1). The sheets are separated a distance S on the z -axis and equidistant from the coordinate M along this direction. Each barrier extends a finite width d in the z -direction and throughout the entire perpendicular plane. The barriers each increase to a maximum amplitude of $\rho^2(x_3) = 2\eta^2$, with the parameter δ defining the skin-width of the tanh function, in increasing from zero to the maximum barrier strength.

5.1.3 Equations of Motion

Implementing the variational principle on the action (5.3) and choosing the temporal gauge $A_0 \equiv 0$ within the gauge freedom yields the dynamical equations:

$$\frac{1}{\mu_0 c} \Sigma_i \partial_i E_i(x) - i \frac{q}{\hbar} \bar{\Psi}(x) \gamma^0 \Psi(x) + \frac{e}{\hbar} \rho^2(x) D_0 \theta(x) - j_0(x) = 0, \quad (5.5a)$$

$$\begin{aligned} \frac{1}{\mu_0 c} \partial_0 E_i(x) + \frac{1}{\mu_0} \Sigma_j \partial_j F_{ji}(x) + i \frac{q}{\hbar} \bar{\Psi}(x) \gamma^i \Psi(x) \\ + \frac{e}{\hbar} \rho^2(x) D_i \theta(x) - j_i(x) = 0, \end{aligned} \quad (5.5b)$$

$$\left(\gamma^\mu D_\mu + \frac{mc}{\hbar} \right) \Psi(x) = 0, \quad (5.5c)$$

$$\partial_\mu (\rho^2(x) D^\mu \theta(x)) = 0, \quad (5.5d)$$

with the temporal gauge on the chosen flat-space metric implying

$$E_i(x) = -c\partial_0 A_i(x); \quad (5.6)$$

the gauge field similarly determines the magnetic field through

$$B_a(x) = \sum_{b,c} \epsilon_{abc} \partial_b A_c. \quad (5.7)$$

These equations comprise the classical dynamics in the unconstrained, $3 + 1$ dimensional system without imposing in particular any symmetry assumptions on the field evolution. The electromagnetic fields thus evolve coupled to the superconducting barrier and the fermionic interaction, in the presence also of the external current. Both the fermionic and the Higgs back-reaction onto the gauge field contribute to the evolution in an analogous manner to this external current: in effect, forming respectively a fermionic and Higgs current contribution to the net current and likewise a fermion and Higgs charge contributing to the total electric charge.

5.2 Continuum Quantum-Dynamics

5.2.1 Quantized Equations of Motion

The fermions require a quantum analysis to examine these intrinsically-quantum particles. Contrastingly, the gauge field will form a sizeable magnetic field (and ideally no electric field); hence, the gauge field corresponds to large occupation numbers and, thus, occupies the classical regime. The Higgs field, modelling the superconducting sheets, represents a classical barrier to a magnetic field, and hence, may also reasonably be assumed to effectively occupy the classical regime. A semi-classical analysis therefore, is employed to examine the system: a classical treatment determines both the gauge and Higgs field dynamics, with the fermions

in the quantum regime.

Completing this (limited) quantization promotes the fermionic field and the conjugate momentum to an operator in the Heisenberg representation and imposes the canonical commutation relations on these operators:

$$\{\hat{\Psi}_a(t, \mathbf{x}), \hat{\Psi}_b^\dagger(t, \mathbf{y})\} = \hbar c (2\pi)^3 \delta^3(\mathbf{x} - \mathbf{y}) \delta_{ab}. \quad (5.8)$$

Applying the Heisenberg equation of motion (2.7) to these fields, equivalently to the scalar field for the oscillon, yields the quantum dynamics of the fermions. These, in effect, simply convert the field in the classical equation (5.5c) to the corresponding Heisenberg operator. Applying the Heisenberg equations to the gauge field in a complete quantization of the system would, likewise in effect, reproduce the classical equation of motion for the gauge field, except converting the gauge, electric and fermion fields to operators. The quantum dynamics for the gauge field, where this field is to be treated classically, may therefore simply be obtained on converting the fermion field to an operator in the classical dynamics (5.5a) and (5.5b).

Forming, lastly, the quantum expectation of these gauge-field operator equations yields the semi-quantized dynamics of the system:

$$\frac{1}{\mu_0 c} \Sigma_i \partial_i E_i(x) - i \frac{q}{\hbar} \langle T \hat{\Psi}(x) \gamma^0 \hat{\Psi}(x) \rangle + \frac{e}{\hbar} \rho^2(x) D_0 \theta(x) - j_0(x) = 0, \quad (5.9a)$$

$$\begin{aligned} \frac{1}{\mu_0 c} \partial_0 E_i(x) + \frac{1}{\mu_0} \Sigma_j \partial_j F_{ji}(x) + i \frac{q}{\hbar} \langle T \hat{\Psi}(x) \gamma^i \hat{\Psi}(x) \rangle \\ + \frac{e}{\hbar} \rho^2(x) D_i \theta(x) - j_i(x) = 0, \end{aligned} \quad (5.9b)$$

$$\left(\gamma^\mu D_\mu + \frac{mc}{\hbar} \right) \hat{\Psi}(x) = 0, \quad (5.9c)$$

$$\partial_\mu (\rho^2(x) D^\mu \theta(x)) = 0. \quad (5.9d)$$

The quantized fermions, thus, evolve under the equation (5.9c) in a background of

classical electromagnetic fields and a superconducting barrier. This fermion field back-reacts through the fermionic current in the equation (5.9b), onto the gauge-field evolution. The quantum dynamics notably match the classical dynamics, except the fermion dynamics now determine the behaviour of the operator field and, most importantly, the gauge equations evolve the quantum, two-point correlators of the fermion field. These importantly result on a precise quantum treatment, in the limit where the gauge and Higgs field behave classically; and, thus, the fermion correlators comprehensively encapsulate the quantum evolution (both on- and off-shell) to examine the consequent tunnelling effects.

5.2.2 Mode Expansion

An expression of the fermionic-field operator in the mode-space may provide the basis to evaluate the fermion correlators determining the dynamics. The mode expansion in particular may be constructed to satisfy

$$\hat{\Psi}(x) = \sqrt{\hbar c} V_x \sum_s \int \frac{d^3\mathbf{k}}{(2\pi)^3} \left(\hat{b}_{\mathbf{k},s} \psi_{\mathbf{k},s}^{(U)}(x) + \hat{d}_{\mathbf{k},s}^\dagger \psi_{\mathbf{k},s}^{(V)}(x) \right), \quad (5.10)$$

where V_x is the total, real-space volume. Each of $\{\psi_{\mathbf{k},s}^{(U)}\}$ and $\{\psi_{\mathbf{k},s}^{(V)}\}$ comprises an orthonormal set with these mode functions independently satisfying the fermion equation of motion (5.5c):

$$(\gamma^\mu D_\mu + m) \psi_{\mathbf{k},s}^{(A)}(x) = 0. \quad (5.11)$$

The $\{\hat{b}_{\mathbf{k},s}^\dagger\}$ $\{\hat{b}_{\mathbf{k},s}\}$ are respectively the creation and annihilation operators for the fermionic particle and $\{\hat{d}_{\mathbf{k},s}^\dagger\}$ $\{\hat{d}_{\mathbf{k},s}\}$ are respectively the creation and annihilation operators for the anti-particle. These are time-independent and

asserted to satisfy¹

$$\begin{aligned}
\{\hat{b}_{\mathbf{k},s}, \hat{d}_{\mathbf{l},r}\} &= 0, \\
\{\hat{b}_{\mathbf{k},s}^\dagger, \hat{d}_{\mathbf{l},r}\} &= 0; \\
\{\hat{b}_{\mathbf{k},s}, \hat{b}_{\mathbf{l},r}^\dagger\} &= V_x^{-2} (2\pi)^3 \delta^3(\mathbf{k} - \mathbf{l}) \delta_{sr}, \\
\{\hat{d}_{\mathbf{k},s}, \hat{d}_{\mathbf{l},r}^\dagger\} &= V_x^{-2} (2\pi)^3 \delta^3(\mathbf{k} - \mathbf{l}) \delta_{sr}.
\end{aligned} \tag{5.12}$$

The annihilation operators conjointly also define the vacuum state:

$$\begin{aligned}
\hat{b}_{\mathbf{k},s} |0\rangle &= 0, \\
\hat{d}_{\mathbf{k},s} |0\rangle &= 0 \quad \forall \mathbf{k}, s.
\end{aligned} \tag{5.13}$$

This provides a standard, initial state of the system; and in the Heisenberg picture, remains the state vector acted on at later times.

Substituting therefore the mode expansion (5.10) into the correlators forming the fermionic currents, applying the definition of the vacuum state and also the

¹ The choice of the ladder anti-commutators imposes a standard configuration to satisfy the constraint for the mode expansion (5.10) to reproduce the canonical field-commutator (5.8).

Validating the ladder commutator-structure in general may result on specifying the mode functions at a particular time and enforcing the consistency constraint. The time invariance of the field commutator hence ensures the determined constraint remains valid throughout the evolution; and the time invariance of the ladder operators likewise imply the asserted commutator structure remains unaltered.

This procedure may most readily be accomplished in the particular case of the vacuum mode functions satisfying the imposed boundary conditions on the space. The vacuum modes comprise the initial modes (see also Section 5.6.1), and therefore confirming the ladder commutators reproduce the canonical field-commutator for these modes may validate the choice of the asserted structure of anti-commutators. The process, also, is expressly demonstrated, subsequently, in the non-standard case of the ansatz mode-expansion with Neumann boundaries on the lattice in the Section 5.6.1.

The necessary condition on the ladder operators enables further considerable variation in the potential anti-commutator structures. This choice of the $V_x^{-2} (2\pi)^3$ factors in the relations implies the dimensionality of the ladder operators equals the inverse square-root of volume; and hence the number operators $\hat{b}_{\mathbf{k},s}^\dagger \hat{b}_{\mathbf{k},s}$ and $\hat{d}_{\mathbf{k},s}^\dagger \hat{d}_{\mathbf{k},s}$ corresponding to the ladder operators form variables of dimensionality equal to the inverse volume. The eigenvalues of the number operators therefore for this choice of the anti-commutators might be associated directly to the number density of the fermion particles in the mode k .

ladder commutators (5.12) yields

$$\langle T\hat{\Psi}(x)\gamma^\mu\hat{\Psi}(x)\rangle = \frac{\hbar c}{2} \sum_s \int \frac{d^3\mathbf{k}}{(2\pi)^3} \left(\bar{\psi}_{\mathbf{k},s}^{(V)}(x)\gamma^\mu\psi_{\mathbf{k},s}^{(V)}(x) - \bar{\psi}_{\mathbf{k},s}^{(U)}(x)\gamma^\mu\psi_{\mathbf{k},s}^{(U)}(x) \right), \quad (5.14)$$

with $\bar{\psi}_{\mathbf{k},s}^{(A)} \equiv i\psi_{\mathbf{k},s}^{(A)\dagger}\gamma^0$. This expression of the correlator in the modes, thus notably incorporates the quantum structure, implicitly, through the application of the ladder commutators in obtaining the final expression.

The correlator expansion substituted into both the electric field equations (5.9b) and (5.9a) and the mode dynamics (5.11), together with the expression of the electric field in the temporal gauge (5.6) and the Higgs dynamics (5.5d), therefore, fully define the evolution of the quantized system.

5.2.3 The Ensemble Approach

An ensemble of fields, analogously to the Ensemble Method in the bosonic case (Section 2.3), may consistently replace the fermionic operator throughout the gauge-field system to determine these semi-quantized dynamics. This method in the fermionic case involves two sets of fields to reproduce the correlator structure of the fermions. These fields in the respective sets are labelled ‘male’, $\Psi_{M,c}$ and ‘female’, $\Psi_{F,c}$ conventionally, where the second index denotes the distinct element within the set. The male and female fields respectively are constructed according to

$$\Psi_{M,c}(x) = \sqrt{\frac{\hbar c}{2}} V_x \sum_s \int \frac{d^3\mathbf{k}}{(2\pi)^3} \left(\xi_{\mathbf{k},s,c}\psi_{\mathbf{k},s}^{(U)}(x) + \zeta_{\mathbf{k},s,c}\psi_{\mathbf{k},s}^{(V)}(x) \right),$$

$$\Psi_{F,c}(x) = \sqrt{\frac{\hbar c}{2}} V_x \sum_s \int \frac{d^3\mathbf{k}}{(2\pi)^3} \left(\xi_{\mathbf{k},s,c}\psi_{\mathbf{k},s}^{(U)}(x) - \zeta_{\mathbf{k},s,c}\psi_{\mathbf{k},s}^{(V)}(x) \right),$$

where $\{\psi_{\mathbf{k},s}^{(U)}\}$ and $\{\psi_{\mathbf{k},s}^{(V)}\}$ are exactly the previous, fermionic modes with $\{\xi_{\mathbf{k},s,c}\}$ and $\{\zeta_{\mathbf{k},s,c}\}$ each comprising a set of complex, random numbers. A statistical average $\langle \cdot \rangle_E$ over the ensemble may specify the random numbers and hence fields

forming the system.

The two sets of random numbers at each wave-vector are asserted to be independent both from one another and likewise from the distributions at a different wave-vector. Each set further is chosen in the limit of an infinite ensemble size to form a Gaussian distribution of mean zero and variance

$$\langle \xi_{\mathbf{k},s} \xi_{\mathbf{l},r}^* \rangle_E = \langle \zeta_{\mathbf{k},s} \zeta_{\mathbf{l},r}^* \rangle_E = V_x^{-2} (2\pi)^3 \delta^3(\mathbf{k} - \mathbf{l}) \delta_{sr},$$

where the variables in this limit denote a frequency density and, accordingly, the statistical average involves an integration over the variable space.

This, on applying the definition of the vacuum state (5.13) provides direct equality between the renormalized correlators forming the fermionic current and the variance of the male and female fields at a particular instant:

$$\langle T \hat{\Psi}(x) \gamma^\mu \hat{\Psi}(x) \rangle = -\frac{1}{2} (\langle \bar{\Psi}_M(x) \gamma^\mu \Psi_F(x) \rangle_E + \langle \bar{\Psi}_F(x) \gamma^\mu \Psi_M(x) \rangle_E). \quad (5.15)$$

In particular, we may choose the set of the real-part $W_{\mathbf{k},s,c}$ and imaginary-part $X_{\mathbf{k},s,c}$ of the $\xi_{\mathbf{k},s,c}$, and likewise the real-part $Y_{\mathbf{k},s,c}$ and imaginary-part $Z_{\mathbf{k},s,c}$ of the $\zeta_{\mathbf{k},s,c}$ each form an independent, Gaussian distribution of mean zero and ensemble-variance

$$\frac{1}{2} V_x^{-2} (2\pi)^3 \delta^3(\mathbf{k} - \mathbf{l}) \delta_{sr},$$

to generate the Gaussian constraint on the complex random-numbers. These constraints on the random numbers hence may yield the equivalence of the ensemble variance to the fermionic correlator and thus an alternative method to evaluate the fermionic currents at a particular instant.

The ensemble fields further each comprise a distinct linear-combination of the modes; and hence the linearity of the mode equation (5.9c) implies the male and female fields individually satisfy the mode dynamics. Evolving the ensemble thus in effect evaluates the evolution of every mode function simultaneously according

to the mode dynamics:

$$(\gamma^\mu D_\mu + m) \Psi_{M/F,c}(x) = 0. \quad (5.16)$$

This moreover ensures that if the equality (5.15) holds at any instant, the result remains valid throughout the subsequent evolution. Establishing this relation in particular at the initial time therefore determines the evolved ensemble-fields yield the quantum correlators at subsequent times. The fermionic correlator, thus, may be consistently replaced by the ensemble variance in the electric field equations (5.9a) and (5.9b) to incorporate the quantum effects within the system.

Equal sample sizes of the random sets in practice may define the ensemble, and accordingly the statistical properties entail the discrete average over the N_E sample-size. These reduced sets approximate the Gaussian distribution and hence yield a variance closely approximating the fermionic correlators at any instant. This finite set might therefore highly accurately determine the electric field evolution.

These equations formed on constructing the finite, statistical variances, and the ensemble-field dynamics (5.16) (replacing the equivalent mode function equation), together with the electric field expression in the temporal gauge (5.6) and the Higgs dynamics (5.5d) thus provide an alternative method to fully determine the evolution of the quantum system.

5.2.4 An Ansatz for the Fields

The structure of the superconducting sheets, defined through the Higgs field, imposes an intrinsic symmetry in the system that may simplify the dynamics.

Orientating both sheets in the x - y plane, with the two uniform and infinite in the x - y direction and separated a finite distance in the z -direction constrains the variation in the superconductor to solely along the z -axis, while the x and y directions are physically identical. The Higgs modulus (5.4) representing this

positioning hence involves purely a z -dependence.

For the electromagnetic fields, likewise, generated homogeneously over the x - y plane and with the fermion current evolving from a uniform configuration in this background, the symmetries suggest that the gauge and Higgs field both reduce to a 1 + 1D problem:

$$\theta(x) = \theta(t, x_3), \quad (5.17a)$$

$$A_i(x) = A_i(t, x_3), \quad (5.17b)$$

where gauge indices include the spatial components with $A_0 \equiv 0$ already set in the choice of the temporal gauge.

To achieve this homogeneity in the electromagnetic fields requires that the external current generating the electromagnetic field also involves only a z -dependence:

$$j_\mu(x) = j_\mu(t, x_3).$$

The homogeneity of this configuration over the x - y plane further implies the electromagnetic fields can be aligned in a particular direction without any physically distinct consequences. To orientate the electric field along the x -direction, in the absence of the fermions and the Higgs field, would result from aligning the external current also in this direction:

$$j_i(x) = \begin{cases} j_1(t, x_3), & i = 1 \\ 0, & i = 2, 3. \end{cases} \quad (5.18)$$

This configuration thus provides the form for the external current satisfying the symmetry constraints.

The currents of the Higgs-field and fermions forming in reaction to the produced gauge fields may reasonably be assumed to match the orientation of the source generating the electromagnetic fields: the resulting Higgs and fermionic

currents in the gauge electric field dynamics aligning in the direction of the external current. For the currents, thus, orientated entirely along the x -axis, the resultant magnetic field aligns entirely along the y -axis. A consistent choice of the gauge fields for this configuration is obtained in the simple formulation

$$A_i(x) = \begin{cases} A_1(t, x_3), & i = 1 \\ 0, & i = 2, 3. \end{cases} \quad (5.19)$$

The homogeneity perpendicular to the z -direction might naively indicate that the fermion modes likewise satisfy an equation of the form:

$$\psi_{\mathbf{k},s}^{(A)}(x) = \psi_{\mathbf{k},s}^{(A)}(t, x_3).$$

Considering the inherently quantum nature of the fermions in the vacuum, though, indicates this simplification is insufficient. The free fermion-modes (through effectively setting the gauge field to zero in the interacting case (5.11)) satisfy

$$(\gamma^\mu \partial_\mu + m) \psi_{\mathbf{k},s}^{(A)}(x) = 0.$$

This system is solved by respectively the standard positive- and negative-energy configuration

$$\begin{aligned} \psi_{\mathbf{k},s}^{(+)} &= e^{ik \cdot x} U_{\mathbf{k},s}, \\ \psi_{\mathbf{k},s}^{(-)} &= e^{-ik \cdot x} V_{\mathbf{k},s}, \end{aligned} \quad (5.20)$$

where $U_{\mathbf{k},s}$ and $V_{\mathbf{k},s}$ specify the constant, four-component spinors satisfying the resultant equations on substituting the respective configurations into the vacuum dynamics. These configurations notably incorporate a dependence on each spatial coordinate even in the entirely isotropic vacuum.

This indicates that any ansatz for the fermion modes must incorporate this

dependence on every spatial direction; moreover, the assertion (in deriving the fermionic correlator (5.14)) that the system evolves from the vacuum state implies that the standard result may exactly specify the initial configuration of the ansatz in the case where these solutions also satisfy the boundary conditions. The application of Neumann boundary conditions in the z -direction expectedly will alter the initial condition²; the separation of the spatial coordinates into distinct factors in the original solution further indicates that the change to the boundary conditions in only the z -direction will alter only the factor including the z -component. Hence, the fields corresponding respectively to the positive and negative energy solutions at the initial time may reasonably be asserted to satisfy

$$\begin{aligned}\psi_{(k_1, k_2, \lambda, s)}^{(U)}(0, \mathbf{x}) &= e^{ik_1 x_1} e^{ik_2 x_2} \chi_{(k_1, k_2, \lambda, s)}^{(U)}(0, x_3), \\ \psi_{(-k_1, -k_2, -\lambda, s)}^{(V)}(0, \mathbf{x}) &= e^{-ik_1 x_1} e^{-ik_2 x_2} \chi_{(-k_1, -k_2, -\lambda, s)}^{(V)}(0, x_3),\end{aligned}$$

where the variable λ labels each element in a complete and orthonormal set of field-configurations³.

²The precise vacuum state for the Neumann boundaries is obtained on the lattice subsequently in Section 5.6.1 where the detailed form is explicitly distinct from the standard, continuum expression simply discretized onto the lattice.

³The operator $\hat{p}_i = -i\hbar\partial_i$ may define the momentum in the i th direction with the eigenvalues correspondingly specifying the momentum of the fermion particles in this direction. Acting this operator on the fermion vacuum-solutions (5.20), hence, readily determines the values $\pm\hbar k_i$ form the momentum of the fermion in the i th direction, and the variable $\pm k_i$, correspondingly, specifies the wave-vector in the i th direction.

This analysis remains valid in the x_1 and x_2 directions for the fermion ansatz, and thus the wavevector k_1 and k_2 remain the relevant variables labelling these directions. Contrastingly, the $\chi_{(k_1, k_2, \lambda, s)}^{(A)}$ in the ansatz for the fermion modes are not necessarily eigenfunctions of the momentum operators and, hence, the variable λ may not necessarily correspond to the particle momentum.

The choice of the initial modes in the ansatz, subsequently (Section 5.6.1), incorporate a linear combination of the standard vacuum solutions. This therefore implies the wave-vector k_3 distinguishes the initial modes and thus, forms the particular value of λ , labelling each mode, at the initial time. The $\chi_{(k_1, k_2, \lambda, s)}^{(A)}$ in the modes though, are each subsequently evolved according to the coupled, semi-quantized dynamics of the system (5.28). These at later times, therefore, will not necessarily form functions involving a linear combination of the vacuum modes nor otherwise necessarily, remain an eigenfunction of the momentum operator. The wave-vector k_3 will, therefore, not necessarily remain the relevant variable to label these functions throughout the evolution; while the more general variable λ may denote the element in the (complete and

While the electric and magnetic fields break the identical state of the x - y directions in the presence only of the superconductor, the fermions interact – rather than with the physical, electromagnetic fields – directly with the gauge field that, under the simplifying symmetry assumption, depends only on the z -coordinate and is homogeneous over the x - y plane. The fermion dynamics thus exclude any source of potential variation in these directions and hence the initial configuration in these dimensions might reasonably remain unaltered in the ansatz at all times with the time dependence solely in the z -dependent factor. This permanent identicality of the x and the y -directions further consistently matches the asserted, constant homogeneity of the interactions affecting the fermion evolution. The ansatz for the fermions incorporating the semi-quantum dynamics thus reasonably imposes

$$\begin{aligned}\psi_{(k_1, k_2, \lambda, s)}^{(U)}(x) &= e^{ik_1 x_1} e^{ik_2 x_2} \chi_{(k_1, k_2, \lambda, s)}^{(U)}(t, x_3), \\ \psi_{(-k_1, -k_2, -\lambda, s)}^{(V)}(x) &= e^{-ik_1 x_1} e^{-ik_2 x_2} \chi_{(-k_1, -k_2, -\lambda, s)}^{(V)}(t, x_3),\end{aligned}$$

where the variable λ label the elements in the complete and orthonormal set of modes to form the expansion of the fermion field.

Substituting this form into the mode expansion (5.10) and accordingly switching the z -integral to vary over the ansatz-label λ in the modified direction⁴ therefore yields the expansion in the mode ansatz; with the ladder operators likewise relabelled to denote association to this alternative variable:

$$\begin{aligned}\hat{\Psi}(x) &= \sqrt{\hbar c V_x} \sum_s \int \frac{dk_1}{(2\pi)} \frac{dk_2}{(2\pi)} \frac{d\lambda}{(2\pi)} \left[\hat{b}_{(k_1, k_2, \lambda, s)} e^{ik_1 x_1} e^{ik_2 x_2} \chi_{(k_1, k_2, \lambda, s)}^{(U)}(t, x_3) \right. \\ &\quad \left. + \hat{d}_{(k_1, k_2, \lambda, s)}^\dagger e^{-ik_1 x_1} e^{-ik_2 x_2} \chi_{(-k_1, -k_2, -\lambda, s)}^{(V)}(t, x_3) \right].\end{aligned}$$

orthonormal) set of field configurations throughout the evolution.

⁴The explicit form of the integration-weighting $d\lambda/(2\pi)$ might be determined through the relation of the mode functions to the fermionic anti-commutator – equivalently to the discrete analogue $\Delta\lambda/(2\pi)$ (see Section 5.6.1).

The ladder-operator anti-commutators correspondingly are asserted to satisfy

$$\begin{aligned}
\{\hat{b}_{(k_1, k_2, \lambda, s)}, \hat{d}_{(l_1, l_2, v, r)}\} &= 0, \\
\{\hat{b}_{(k_1, k_2, \lambda, s)}^\dagger, \hat{d}_{(l_1, l_2, v, r)}\} &= 0; \\
\{\hat{b}_{(k_1, k_2, \lambda, s)}, \hat{b}_{(l_1, l_2, v, r)}^\dagger\} &= V_x^{-2} (2\pi)^3 \delta(k_1 - l_1) \delta(k_2 - l_2) \delta(\lambda - v) \delta_{sr}, \\
\{\hat{d}_{(k_1, k_2, \lambda, s)}, \hat{d}_{(l_1, l_2, v, r)}^\dagger\} &= V_x^{-2} (2\pi)^3 \delta(k_1 - l_1) \delta(k_2 - l_2) \delta(\lambda - v) \delta_{sr}, \quad (5.21)
\end{aligned}$$

where notably, the ansatz-label λ replaces the wave-vector in the delta function compared to the operator relations (5.12) in the standard expansion⁵.

Implementing the transformation $k_{1,2} \rightarrow -k_{1,2}$, $\lambda \rightarrow -\lambda$ on the second term of the ansatz expansion yields the expression

$$\begin{aligned}
\hat{\Psi}(x) = \sqrt{\hbar c} V_x \sum_s \int \frac{dk_1}{(2\pi)} \frac{dk_2}{(2\pi)} \frac{d\lambda}{(2\pi)} & \left[\hat{b}_{(k_1, k_2, \lambda, s)} e^{ik_1 x_1} e^{ik_2 x_2} \chi_{(k_1, k_2, \lambda, s)}^{(U)}(t, x_3) \right. \\
& \left. + \hat{d}_{(-k_1, -k_2, -\lambda, s)}^\dagger e^{ik_1 x_1} e^{ik_2 x_2} \chi_{(k_1, k_2, \lambda, s)}^{(V)}(t, x_3) \right]; \quad (5.22)
\end{aligned}$$

both the positive- and the negative-energy ansatz in the expansion thereby reduce to the identical, general form

$$\psi_{(k_1, k_2, \lambda, s)}^{(A)}(x) = e^{ik_1 x_1} e^{ik_2 x_2} \chi_{(k_1, k_2, \lambda, s)}^{(A)}(t, x_3),$$

thus simplifying the fermion ansatz.

This form for the fermion modes together with the selected, spatial gauge-configuration (5.19) and the Higgs phase (5.17a) provide the ansatz for the field evolution under the choice of the temporal gauge, in the presence of the specified

⁵The structure of the ladder anti-commutators may ultimately be validated through their use to generate the field commutator (5.8), equivalently to the ladder commutators in the mode function case (see footnote 1).

This procedure will be demonstrated subsequently in the ansatz-case on the lattice with Neumann boundaries (Section 5.6.1).

external current (5.18) and the chosen structure of the Higgs modulus (5.4).

Substituting the gauge and Higgs-phase ansatz into the electric field evolution (5.9a) and (5.9b) and the Higgs dynamics (5.9d) with the modulus structure (5.4) and imposed external-current (5.18) yields

$$i\frac{q}{\hbar}\langle T\hat{\Psi}(x)\gamma^0\hat{\Psi}(x)\rangle - \frac{e}{\hbar}\rho^2(x_3)\partial_0\theta(t, x_3) + j_0(t, x_3) = 0, \quad (5.23)$$

$$i\frac{q}{\hbar}\langle T\hat{\Psi}(x)\gamma^{2,3}\hat{\Psi}(x)\rangle + \frac{e}{\hbar}\rho^2(x_3)\partial_0\theta(t, x_3) = 0, \quad (5.24)$$

$$\begin{aligned} \frac{1}{\mu_0 c}\partial_0 E_1(t, x_3) + \frac{1}{\mu_0}\partial_3^2 A_1(t, x_3) + i\frac{q}{\hbar}\langle T\hat{\Psi}(x)\gamma^1\hat{\Psi}(x)\rangle \\ - \left(\frac{e}{\hbar}\right)^2 \rho^2(x_3)A_1(t, x_3) - j_1(t, x_3) = 0, \end{aligned} \quad (5.25)$$

$$(\rho^2(x_3) [\partial_0^2 - \partial_3^2] - 2\rho(x_3)\partial_3\rho(x_3)\partial_3)\theta(t, x_3) = 0; \quad (5.26)$$

where

$$E_1(t, x_3) = -c\partial_0 A_1(t, x_3) \quad (5.27)$$

results on applying the gauge ansatz to the electric field expression (5.6). Likewise, the gauge, Higgs-phase and mode ansatz substituted into the mode function dynamics (5.11) with the modulus structure (5.4) determines

$$\left(\gamma^0\partial_0 + i\left[k_1 - i\frac{q}{\hbar}A_1(t, x_3)\right]\gamma^1 + ik_2\gamma^2 + \gamma^3\partial_3 + \frac{mc}{\hbar}\right)\chi_{(k_1, k_2, \lambda, s)}^{(A)}(t, x_3) = 0. \quad (5.28)$$

Substituting the ansatz-expansion (5.22) also into the fermionic-correlator, on applying the ladder anti-commutator (5.21) and vacuum-state definition (5.13)

yields

$$\begin{aligned} \langle T\hat{\Psi}(x)\gamma^\mu\hat{\Psi}(x) \rangle = & \\ & \frac{\hbar c}{2} \sum_s \int \frac{dk_1}{(2\pi)} \frac{dk_2}{(2\pi)} \frac{d\lambda}{(2\pi)} \left(\bar{\chi}_{(k_1, k_2, \lambda, s)}^{(V)}(t, x_3) \gamma^\mu \chi_{(k_1, k_2, \lambda, s)}^{(V)}(t, x_3) \right. \\ & \left. - \bar{\chi}_{(k_1, k_2, \lambda, s)}^{(U)}(t, x_3) \gamma^\mu \chi_{(k_1, k_2, \lambda, s)}^{(U)}(t, x_3) \right), \quad (5.29) \end{aligned}$$

with $\bar{\chi}_{(k_1, k_2, \lambda, s)}^{(A)} \equiv i\chi_{(k_1, k_2, \lambda, s)}^{(A)\dagger} \gamma^0$. This expansion in the mode ansatz (equivalently to the standard mode expansion, Section 5.2.2), thus, implicitly incorporates the quantum structure through the application of the ladder commutators. These results for the ansatz, importantly therefore, simplify the quantum dynamics to a one-dimensional system varying only over the z -direction in coordinate space, with the correlator involving a summation over a three-dimensional mode-space.

The Higgs-field phase entirely decouples from the gauge and fermionic fields, and thus has no effect on the electromagnetic fields interacting with the barrier, with or without fermions present. Hence, we may for simplicity neglect the phase throughout the evolution – in effect choosing $\theta(t, x_3) = 0$ to satisfy the evolution equation (5.5d) – without constraint on the interactions of principal interest.

This assertion therefore eliminates the phase evolution from the dynamics; and further determines the gauge constraints (5.23) and (5.24) in the ansatz satisfy

$$\begin{aligned} i\frac{q}{\hbar} \langle T\hat{\Psi}(x)\gamma^0\hat{\Psi}(x) \rangle + j_0(t, x_3) &= 0, \\ i\frac{q}{\hbar} \langle T\hat{\Psi}(x)\gamma^2\hat{\Psi}(x) \rangle &= 0, \\ i\frac{q}{\hbar} \langle T\hat{\Psi}(x)\gamma^3\hat{\Psi}(x) \rangle &= 0. \end{aligned}$$

These results thus specify the constraints on the gauge field in the ansatz case; while the electric field dynamics (5.25) and mode function ansatz-equation (5.28), together with the corresponding correlator expansion (5.29) and the expression of

the electric field (5.27) in the ansatz may fully determine the quantized evolution under the inherent symmetries of the system.

5.3 Tunnelling of the 3rd Kind: Simple Estimate

An effective one-loop action provides the basis in perturbative expressions obtained for tunnelling of the 3rd kind (see [98] for details). These calculations in a comparable system to the present configuration but involving only a single barrier imply the constant, external field B_{ext} induces a field B_{int} having crossed the barrier through the tunnelling process. The transmission asymptotically far from the barrier results proportionately to the external field, in the ratio

$$\frac{|B_{\text{int}}|}{|B_{\text{ext}}|} = \frac{q^2}{48\pi^2} \int_1^\infty \frac{d\tau}{\tau^4} \sqrt{\tau^2 - 1} (1 + 2\tau^2) \exp(-2m d \tau), \quad (5.30)$$

for the fermion mass m and charge q through the barrier of thickness d , with the result obtained in natural units – matching, importantly, the analysis in the subsequent tunnelling simulations. This integral is to be evaluated analytically, and for $m = 1$, $q = 0.3$, $e = 1$ and $d = 1.5$, chosen in the ensuing simulations (Section 6.1 and 6.5.1), hence yields $|B_{\text{int}}|/|B_{\text{ext}}| = 3.4 \cdot 10^{-6}$. The present configuration in contrast to the analytic case involves two barriers and encloses the tunnelled field within a finite distance from the barriers. This therefore indicates the true result in the simulated case involves a multiplicative correction between one and two to the analytic estimate.

A superconducting barrier experimentally would induce the distinctive exponential decay in the magnetic field; and the Higgs-field model likewise can reproduce this characteristic decay. Solving the continuum dynamics excluding the fermions can, therefore, provide an estimate for the classical field decay through the barrier. Adding this to the tunnelling result hence forms a reasonable estimate for the observed transmission. The classical solution further enables distinguishing the contrastive tunnelling effects.

Establishing the constant magnetic field outside the superconducting enclosure essentially produces a static, final state for measuring the transmission. Accordingly setting the gauge fields constant in the electric field dynamics (5.25) (incorporating the symmetries) outside the external current and for the fermions omitted hence implies

$$\partial_3^2 A_1(t, x_3) = -e^2 \rho^2(x_3) A_1,$$

on also imposing natural units to match the tunnelling case – and the subsequent simulations. A step-function of the maximum barrier amplitude $2\eta^2$ provides an accurate and simple approximation to the barrier configuration in the limiting case where the modulus function rises steeply – on setting δ sufficiently small. This provides a readily tractable system; the classical solutions in this case simply satisfy

$$A_1(t, x_3) = A_{1,\text{ext}} \exp\left(-\sqrt{2}e\eta\right),$$

where imposing continuity at the exterior boundary to the barrier further determines $A_{1,\text{ext}}$ equals the gauge field adjoining this boundary. The gauge-field relation to the magnetic field (5.7) hence readily determines the magnetic field $B_{2,\text{int}}$ inside the enclosure satisfies

$$B_{2,\text{int}}(t, x_3) = B_{2,\text{ext}} \exp\left(-\sqrt{2}e\eta\right), \quad (5.31)$$

where again the continuity at the boundary implies $B_{2,\text{ext}}$, equals the (uniform) external value. This accordingly provides the estimate to add to the tunnelling contribution and for contrasting the classical and quantum cases.

The figure 5.2 shows the constant tunnelling contribution and the varying transmission on changing the wall thickness for $e = 1$ and $d = 1.5$ in the case without fermions and, additionally, $q = 0.3$ and $m = 1$ with the fermions – notably, matching the parameter choice in the subsequent simulations. The tun-

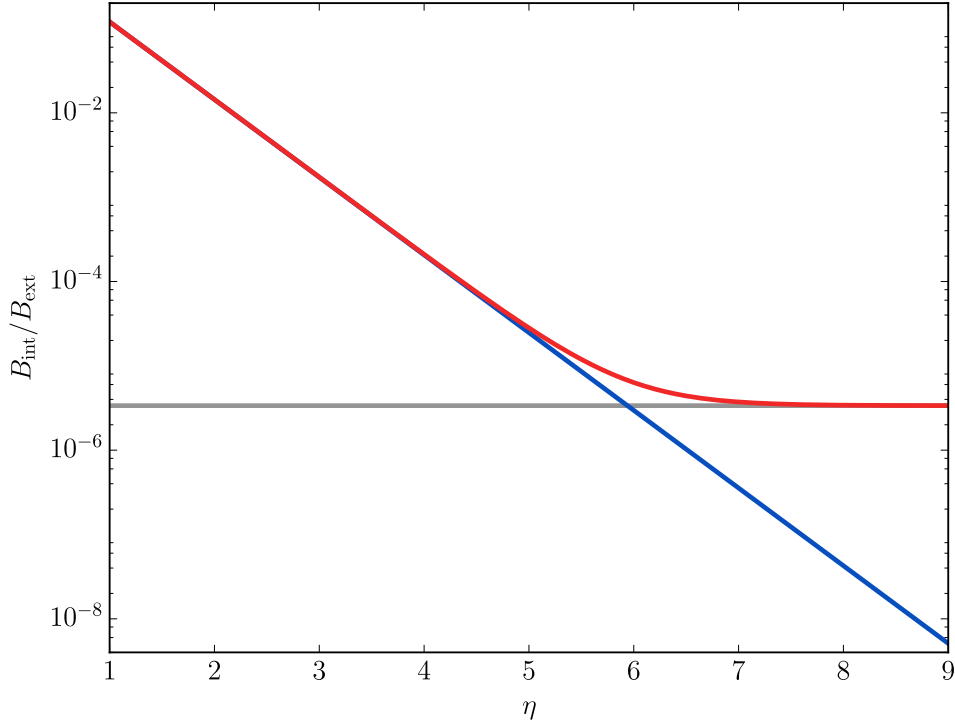


Figure 5.2: The (constant) analytic estimate for tunnelling of the 3rd kind (grey) obtained through the equation (5.30) where $m = 1$, $q = 0.3$, $e = 1$ and $d = 1.5$; the simplified estimate of the classical transmission (blue) through the superconducting barrier (equation 5.31) on varying the wall strength for the chosen values of e and d ; the combined classical and tunnelling contributions (red) to estimate the quantum magnetic-transmission. These indicate the tunnelling generates a distinctive signal where $\eta \gtrsim 6$.

nelling fermions notably form the main contribution where $\eta \gtrsim 6$ while for the weaker barrier strengths, the classical contribution dominates the transmission. Deviations in the numerical results compared to the simplistic estimates would likely result through forming the magnetic field, in practice, using the boundary current, and also with the damping terms present (to produce the static, final state); the approximation to the barrier configuration for deriving the estimate would expectedly also contribute to the discrepancy. The analytic calculations,

though, usefully indicate the approximate tunnelling contribution. This hence will enable evaluating whether the perturbative (one-loop) approximations for the tunnelling accurately describe the resultant signal. These estimates moreover indicate the regime where the signal deviates from the classical case; and thus, usefully, indicates the barrier strengths to examine for detecting this tunnelling signal.

5.4 Discretized Dynamics

5.4.1 Action

We discretize the system onto a lattice through the action while retaining the $U(1)$ symmetry (5.1) through the application of a link-function to incorporate both the gauge fields and the Higgs phase:

$$\begin{aligned}
S(X) = & \\
& \frac{1}{c} \Delta V \left[\sum_i \frac{\hbar^2}{2q\mu_0(\Delta x_i)^2(\Delta x_0)^2} (2 - U_{i0}(X) - U_{0i}(X)) \right. \\
& - \sum_{ij} \frac{\hbar^2}{4q^2\mu_0(\Delta x_i)^2(\Delta x_j)^2} (2 - U_{ij}(X) - U_{ji}(X)) \\
& - \sum_{\mu} \frac{1}{2\Delta x_{\mu}} \bar{\Psi}(X) \gamma^{\mu} \left(U_{\mu}(X) \Psi(X + \mu) - U_{\mu}^{\dagger}(X - \mu) \Psi(X - \mu) \right) \\
& + \frac{mc}{\hbar} \bar{\Psi}(X) \Psi(X) \\
& + \frac{\rho^2(X)}{2(\Delta x_0)^2} \left(2 - \Theta^{\dagger}(X) U_0^{e/q}(X) \Theta(X + 0) - \Theta^{\dagger}(X + 0) U_0^{(e/q)\dagger}(X) \Theta(X) \right) \\
& \left. - \sum_i \frac{\rho^2(X)}{2(\Delta x_i)^2} \left(2 - \Theta^{\dagger}(X) U_i^{e/q}(X) \Theta(X + i) - \Theta^{\dagger}(X + i) U_i^{(e/q)\dagger}(X) \Theta(X) \right) \right], \tag{5.32}
\end{aligned}$$

with $\Delta V \equiv \Delta x_0 \Delta x_1 \Delta x_2 \Delta x_3 = c \Delta t \Delta x_1 \Delta x_2 \Delta x_3$, and where the lattice-links are defined through

$$U_\mu(X) \equiv \exp\left(-i \frac{q}{\hbar} \Delta x_\mu A_\mu(X)\right), \quad (5.33a)$$

$$U_{\mu\nu}(X) \equiv U_\mu(X) U_\nu(X + \mu) U_\mu^\dagger(X + \mu) U_\nu^\dagger(X), \quad (5.33b)$$

$$\Theta(X) \equiv \exp(i\theta(X)). \quad (5.33c)$$

To alleviate the issue of (the unphysical) fermion spatial-doublers on the lattice, a Wilson term is added to the lattice action:

$$\frac{1}{c} \Delta V \sum_i r_w \frac{1}{2\Delta x_i} \bar{\Psi}(X) (U_i(X) \Psi(X + i) - 2\Psi(X) + U_i(X - i) \Psi(X - i)).$$

(The addition notably vanishes in the limit of small coordinate-spacings, and the action hence reduces to precisely the continuum action (5.3) in the limit of small-spatial and -temporal divisions.)

Applying the variational principle that $\delta S = 0$ to the discretized action for each field and imposing the temporal gauge yields the gauge-invariant dynamics

for the discrete system:

$$\begin{aligned} & \sum_i \frac{1}{(\Delta x_i)^2 (\Delta x_0)^2} \frac{\hbar^2}{2q^2 \mu_0} ([U_{0i}(X) - U_{i0}(X)] - [U_{0i}(X-i) - U_{i0}(X-i)]) \\ & + \frac{i}{\Delta x_0} \text{Im} \{ \bar{\Psi}(X) \gamma^0 \Psi(X+0) \} \\ & + \frac{i}{(\Delta x_0)^2} \frac{e}{q} \rho^2(X) \text{Im} \{ \Theta^\dagger(X) \Theta(X+0) \} = 0, \end{aligned} \quad (5.34a)$$

$$\begin{aligned} & \frac{1}{(\Delta x_i)^2 (\Delta x_0)^2} \frac{\hbar^2}{2q^2 \mu_0} ([U_{0i}(X) - U_{i0}(X)] - [U_{0i}(X-0) - U_{i0}(X-0)]) \\ & + \sum_j \frac{i}{(\Delta x_i)^2 (\Delta x_j)^2} \frac{\hbar^2}{q^2 \mu_0} \text{Im} \{ U_{ij}(X) - U_{ji}(X-j) \} \\ & - \frac{i}{\Delta x_i} \text{Im} \{ \bar{\Psi}(X) \gamma^i U_i(X) \Psi(X+i) \} + \frac{i}{\Delta x_i} r_w \text{Im} \{ \bar{\Psi}(X) U_i(X) \Psi(X+i) \} \\ & + \frac{i}{(\Delta x_i)^2} \frac{e}{q} \rho^2(X) \text{Im} \{ \Theta^\dagger(X) U_i^{e/q} \Theta(X+i) \} = 0, \end{aligned} \quad (5.34b)$$

$$\begin{aligned} & \frac{1}{2\Delta x_0} \gamma^0 (\Psi(X+0) - \Psi(X-0)) \\ & + \sum_i \frac{1}{2\Delta x_i} \gamma^i (U_i(X) \Psi(X+i) - U_i^\dagger(X-i) \Psi(X-i)) + \frac{mc}{\hbar} \Psi(X) \\ & - \sum_i \frac{1}{\Delta x_i} \frac{r_w}{2} (U_i(X) \Psi(X+i) \\ & - 2\Psi(X) + U_i^\dagger(X-i) \Psi(X-i)) = 0, \end{aligned} \quad (5.34c)$$

$$\begin{aligned} & \frac{1}{\Delta x_0} \rho^2(X) (S(X) - S(X-0)) \\ & - \sum_i \frac{1}{(\Delta x_i)^2} \left(\rho^2(X) \text{Im} \{ \Theta^\dagger(X) U_i^{e/q}(X) \Theta(X+i) \} \right. \\ & \left. - \rho^2(X-i) \text{Im} \{ \Theta^\dagger(X-i) U_i^{e/q}(X-i) \Theta(X) \} \right) = 0, \end{aligned} \quad (5.34d)$$

where the evolution of the phase link in the dynamics is expressed in the final

equation through⁶

$$S(X) \equiv \frac{1}{2i\Delta x_0} \left(\Theta^\dagger(X)\Theta(X+0) - \Theta^\dagger(X+0)\Theta(X) \right). \quad (5.35)$$

The electric field in the discretized system, corresponding in the limit of small lattice-spacing to the continuum form of the electric field (5.6) may be defined in relation to the gauge links by

$$E_i(X) = \frac{-i}{\Delta x_0 \Delta x_i} \frac{\hbar c}{2q} (U_{0i}(X) - U_{i0}(X)). \quad (5.36)$$

This definition substituted into the discretized gauge-dynamics (5.34a) and (5.34b) hence determine respectively that the electric field on the lattice satisfies

$$\begin{aligned} & \sum_i \frac{1}{\Delta x_i} \frac{1}{\mu_0 c} (E_i(X) - E_i(X-i)) \\ & + \frac{1}{\Delta x_0} \text{Im} \{ \bar{\Psi}(X) \gamma^0 \Psi(X+0) \} \\ & + \frac{1}{\Delta x_0} \frac{e}{\hbar} \rho^2(X) \text{Im} \{ \Theta^\dagger(X) \Theta(X+0) \} = 0, \end{aligned} \quad (5.37a)$$

$$\begin{aligned} & \frac{1}{\Delta x_0} \frac{1}{\mu_0 c} (E_i(X) - E_i(X-0)) \\ & + \sum_j \frac{1}{\Delta x_i (\Delta x_j)^2} \frac{\hbar}{q \mu_0} \text{Im} \{ U_{ij}(X) - U_{ji}(X-j) \} \\ & - \frac{q}{\hbar} \text{Im} \{ \bar{\Psi}(X) \gamma^i U_i(X) \Psi(X+i) \} + \frac{q}{\hbar} r_w \text{Im} \{ \bar{\Psi}(X) U_i(X) \Psi(X+i) \} \\ & + \frac{1}{\Delta x_i} \frac{e}{\hbar} \rho^2(X) \text{Im} \{ \Theta^\dagger(X) U_i^{e/q} \Theta(X+i) \} = 0. \end{aligned} \quad (5.37b)$$

A discrete approximation of the magnetic field in the continuum further may

⁶This definition of $S(X)$ in the Higgs dynamics (5.34d) simplifies the relation of the phase at differing times – subsumed into the constructed variable – to the spatial summation over components at a single instant. (Ultimately, this enables evolving the phase through iterating the $S(X)$ according to the equation (5.34d) then applying this constructed definition to compute the successive $\Theta(X)$ (see also Section 5.4.4).

define the equivalent field on the lattice:

$$B_a(X) = \sum_{b,c} \epsilon_{abc} \left(\frac{A_c(X+b) - A_c(X-b)}{2\Delta x_b} \right). \quad (5.38)$$

These equations specify the discretized electric field dynamics determined on varying the action. Both the Higgs field and the fermion term without the Wilson parameter, equivalently to the continuum, each contribute, in effect, a current to electric field dynamics and an additional charge in the total electric charge. The inclusion of the Wilson term in the action also generates similar terms in the lattice equations: likewise, in effect, forming an additional Wilson-contribution in the electric field dynamics, and a Wilson component in the total electric charge. These additional terms, in the continuum limit, notably reduce to zero; and thus, ensures the Wilson terms in the action, to eliminate the unphysical doublers in the discrete system, produces an effect distinctively on the lattice. The lattice electromagnetic-dynamics, therefore, form the discrete analogue to the continuum gauge-field dynamics (5.5), except, notably, omitting the external current.

Simply subtracting the term $j_\mu(X)$ consistently – to match the free-indices – in the lattice equations may provide discrete form of the continuum external current. This suitably both reproduces the external current in the continuum on reducing the lattice spacings to zero while the gauge-invariance of the external current under gauge transformations ensures the dynamics retain the overall gauge symmetry.

(Comparing both the Higgs and the fermion current on the lattice to the continuum dynamics demonstrates that the discrete form for these continuum currents involves the field values at both X and $X + \mu$. The Wilson current similarly involves the fermion field evaluated at both X and $X + \mu$. This indicates the discrete analogue to the external current likewise involves values evaluated at adjacent sites. The single term $j_\mu(X)$ though in practice may define the effective

current at any site: incorporating the adjacent values.)

Implementing this modification to the gauge dynamics on the lattice yields:

$$\begin{aligned}
& \sum_i \frac{1}{\Delta x_i} \frac{1}{\mu_0 c} (E_i(X) - E_i(X - i)) \\
& + \frac{q}{\hbar} \text{Im} \{ \bar{\Psi}(X) \gamma^0 \Psi(X + 0) \} \\
& + \frac{1}{\Delta x_0} \frac{e}{\hbar} \rho^2(X) \text{Im} \{ \Theta^\dagger(X) \Theta(X + 0) \} - j_0(X) = 0, \\
\\
& \frac{1}{\Delta x_0} \frac{1}{\mu_0 c} (E_i(X) - E_i(X - 0)) + \sum_j \frac{1}{\Delta x_i (\Delta x_j)^2} \frac{\hbar}{q \mu_0} \text{Im} \{ U_{ij}(X) - U_{ji}(X - j) \} \\
& - \frac{q}{\hbar} \text{Im} \{ \bar{\Psi}(X) \gamma^i U_i(X) \Psi(X + i) \} + \frac{q}{\hbar} r_w \text{Im} \{ \bar{\Psi}(X) U_i(X) \Psi(X + i) \} \\
& + \frac{1}{\Delta x_i} \frac{e}{\hbar} \rho^2(X) \text{Im} \{ \Theta^\dagger(X) U_i^{e/q} \Theta(X + i) \} - j_i(X) = 0.
\end{aligned}$$

This result, together with the Higgs-phase and fermionic equations on the lattice form the discretized analogue to the continuum system (5.5) in 3 + 1-dimensions without symmetry assumptions. These dynamics, accordingly, with the Higgs -variable (5.35) to express the phase evolution, and also the electric and magnetic field definitions on the lattice fully specify the evolution of the discrete system.

5.4.2 Quantized Equations of Motion

Implementing the semi-quantization, as in the continuum case, promotes solely the fermionic field and conjugate momentum to an operator in the Heisenberg representation and imposes the canonical commutation relations on these fields, though in the discrete functions:

$$\{ \hat{\Psi}_a(T, \mathbf{X}), \hat{\Psi}_b^\dagger(T, \mathbf{Y}) \} = \hbar c \frac{\delta_{\mathbf{X}\mathbf{Y}}^3}{\Delta x_1 \Delta x_2 \Delta x_3} \delta_{ab}, \quad (5.39)$$

where the $\delta_{\mathbf{X}\mathbf{Y}}^3 / (\Delta x_1 \Delta x_2 \Delta x_3)$ has replaced the continuum Dirac-delta.

The quantum dynamics in the discrete system may be obtained equivalently

to those in the continuum on applying the Heisenberg equation of motion. This again, in effect, simply converts the fermion field in the classical equations to the corresponding Heisenberg operator. Forming the expectation of the operator equations hence yields the semi-quantized dynamics of the system:

$$\begin{aligned} & \sum_i \frac{1}{\Delta x_i} \frac{1}{\mu_0 c} (E_i(X) - E_i(X - i)) \\ & + \frac{q}{\hbar} \text{Im} \{ \langle T \hat{\Psi}(X) \gamma^0 \hat{\Psi}(X + 0) \rangle \} \\ & + \frac{1}{\Delta x_0} \frac{e}{\hbar} \rho^2(X) \text{Im} \{ \Theta^\dagger(X) \Theta(X + 0) \} - j_0(X) = 0, \end{aligned} \quad (5.40a)$$

$$\begin{aligned} & \frac{1}{\Delta x_0} \frac{1}{\mu_0 c} (E_i(X) - E_i(X - 0)) \\ & + \sum_j \frac{1}{\Delta x_i (\Delta x_j)^2} \frac{\hbar}{q \mu_0} \text{Im} \{ U_{ij}(X) - U_{ji}(X - j) \} \\ & - \frac{q}{\hbar} \text{Im} \left\{ \langle T \hat{\Psi}(X) \gamma^i U_i(X) \hat{\Psi}(X + i) \rangle \right\} + \frac{q}{\hbar} r_w \text{Im} \left\{ \langle T \hat{\Psi}(X) U_i(X) \hat{\Psi}(X + i) \rangle \right\} \\ & + \frac{1}{\Delta x_i} \frac{e}{\hbar} \rho^2(X) \text{Im} \left\{ \Theta^\dagger(X) U_i^{e/q} \Theta(X + i) \right\} - j_i(X) = 0, \end{aligned} \quad (5.40b)$$

$$\begin{aligned} & \frac{1}{2\Delta x_0} \gamma^0 \left(\langle \hat{\Psi}(X + 0) \rangle - \langle \hat{\Psi}(X - 0) \rangle \right) \\ & + \sum_i \frac{1}{2\Delta x_i} \gamma^i \left(U_i(X) \langle \hat{\Psi}(X + i) \rangle - U_i^\dagger(X - i) \langle \hat{\Psi}(X - i) \rangle \right) + \frac{mc}{\hbar} \langle \hat{\Psi}(X) \rangle \\ & - \sum_i \frac{1}{\Delta x_i} \frac{r_w}{2} \left(U_i(X) \langle \hat{\Psi}(X + i) \rangle \right. \\ & \left. - 2 \langle \hat{\Psi}(X) \rangle + U_\mu^\dagger(X - i) \langle \hat{\Psi}(X - i) \rangle \right) = 0, \end{aligned} \quad (5.40c)$$

$$\begin{aligned} & \frac{1}{\Delta x_0} \rho^2(X) (S(X) - S(X - 0)) \\ & - \sum_i \frac{1}{(\Delta x_i)^2} \left(\rho^2(X) \text{Im} \left\{ \Theta^\dagger(X) U_i^{e/q}(X) \Theta(X + i) \right\} \right. \\ & \left. - \rho^2(X - i) \text{Im} \left\{ \Theta^\dagger(X - i) U_i^{e/q}(X - i) \Theta(X) \right\} \right) = 0. \end{aligned} \quad (5.40d)$$

These form the discretized analogue of the fundamental, continuum equations of motion (5.9) to determine the quantum-fermion evolution in the background of

the classical electromagnetic fields and a superconducting barrier, with the quantum back-reaction through the fermionic (and Wilson) current onto the gauge field.

5.4.3 Mode Expansion

Expanding the fermionic fields on the lattice into the mode functions results in the standard substitution of the integral in the continuum expansion to a summation over the finite and discrete mode-space⁷:

$$\hat{\Psi}(X) = \sqrt{\hbar c V_x} \sum_s \sum_{\mathbf{K}} \frac{\Delta k_1}{2\pi} \frac{\Delta k_2}{2\pi} \frac{\Delta k_3}{2\pi} \left[\hat{b}_{\mathbf{K},s} \psi_{\mathbf{K},s}^{(U)}(X) + \hat{d}_{\mathbf{K},s}^\dagger \psi_{\mathbf{K},s}^{(V)}(X) \right]. \quad (5.41)$$

The orthonormal modes $\{\psi_{\mathbf{K},s}^{(U)}\}$ and $\{\psi_{\mathbf{K},s}^{(V)}\}$ on the lattice independently satisfy the discrete, fermion equation of motion (5.40c):

$$\begin{aligned} & \frac{1}{2\Delta x_0} \gamma^0 \left(\psi_{\mathbf{K},s}^{(A)}(X+0) - \psi_{\mathbf{K},s}^{(A)}(X-0) \right) \\ & + \sum_i \frac{1}{2\Delta x_i} \gamma^i \left(U_i(X) \psi_{\mathbf{K},s}^{(A)}(X+i) - U_i^\dagger(X-i) \psi_{\mathbf{K},s}^{(A)}(X-i) \right) + \frac{mc}{\hbar} \psi_{\mathbf{K},s}^{(A)}(X) \\ & - \sum_i \frac{1}{\Delta x_i} \frac{r_w}{2} \left(U_i(X) \psi_{\mathbf{K},s}^{(A)}(X+i) - 2\psi_{\mathbf{K},s}^{(A)}(X) + U_i^\dagger(X-i) \psi_{\mathbf{K},s}^{(A)}(X-i) \right) = 0. \end{aligned} \quad (5.42)$$

⁷The choice of a particular boundary condition on the spatial lattice will determine the precise relationship between the site index e_i in the mode-space and the lattice wave-vector K (see Section 5.6.1)

Asserting, further, the creation and annihilation operators satisfy analogous relations to those in the continuum thus imposes

$$\{\hat{b}_{\mathbf{K},s}, \hat{d}_{\mathbf{L},r}\} = 0, \quad (5.43a)$$

$$\{\hat{b}_{\mathbf{K},s}^\dagger, \hat{d}_{\mathbf{L},r}\} = 0; \quad (5.43b)$$

$$\{\hat{b}_{\mathbf{K},s}, \hat{b}_{\mathbf{L},r}^\dagger\} = V_x^{-2} (2\pi)^3 \delta_{sr} \frac{\delta_{\mathbf{KL}}^3}{\Delta k_1 \Delta k_2 \Delta k_3}, \quad (5.43c)$$

$$\{\hat{d}_{\mathbf{K},s}, \hat{d}_{\mathbf{L},r}^\dagger\} = V_x^{-2} (2\pi)^3 \delta_{sr} \frac{\delta_{\mathbf{KL}}^3}{\Delta k_1 \Delta k_2 \Delta k_3}, \quad (5.43d)$$

where the Dirac delta-function in the respective, continuum commutators has been substituted for the equivalent Kronecker-delta factor⁸.

Substituting the discretized mode-expansion (5.41) into the fermionic corre-

⁸The choice of the ladder anti-commutators ensure the mode-expansion (5.41) satisfies the necessary constraint to reproduce the canonical field-commutator (5.39): equivalently to the mode function method in the continuum (see footnote 1).

This procedure will be demonstrated subsequently on the lattice, in the non-standard case of the ansatz mode-expansion with Neumann boundaries (Section 5.6.1).

The choice of the $V_x^{-2} (2\pi)^3$ factor analogous to the continuum case further implies the dimensionality of the ladder operators and hence the corresponding number operators $\hat{b}_{\mathbf{K},s}^\dagger \hat{b}_{\mathbf{K},s}$ and $\hat{d}_{\mathbf{K},s}^\dagger \hat{d}_{\mathbf{K},s}$ in the discrete case likewise match. Hence the eigenvalues of the number operators for the choice of discretized anti-commutators might be associated directly to the number density of the fermion particles in a mode K on the lattice.

An alternative choice in the variety of potential anti-commutators might be to entirely eliminate all except the dimensionless factors in the relations; and accordingly modify the factors in the mode-expansion to satisfy the condition to reproduce the canonical field-commutator. This configuration implies the ladder operators and hence corresponding number operators to equally be dimensionless. The eigenvalues of the number operators in this system may therefore be associated directly to the total fermion particle number in the associated mode. This may be considered to provide a more sensible quantity on the lattice; with the corresponding anti-commutator structure, accordingly, forming a more sensible choice on the lattice than the direct equivalence to the continuum.

Since the ladder operators occur only in the fermion correlators within the dynamics and these are invariant under the change in ladder-commutator structure; and further since this study omits any direct measurement of the particle number, the particular choice of the ladder commutator structure is irrelevant to the analysis. The construction of the ladder anti-commutators on the lattice directly equivalent to the continuum provides a simple uniformity in the choice of commutator structure.

lators on the lattice and applying the vacuum-state definition (5.13) provides

$$\begin{aligned} \langle T \hat{\Psi}(X) \hat{O} \hat{\Psi}(X + \mu) \rangle = \\ \frac{\hbar c}{2} \sum_s \sum_{\mathbf{K}} \frac{\Delta k_1}{2\pi} \frac{\Delta k_2}{2\pi} \frac{\Delta k_3}{2\pi} \left[\bar{\psi}_{\mathbf{K},s}^{(V)}(X) \hat{O} \psi_{\mathbf{K},s}^{(V)}(X + \mu) \right. \\ \left. - \bar{\psi}_{\mathbf{K},s}^{(U)}(X) \hat{O} \psi_{\mathbf{K},s}^{(U)}(X + \mu) \right], \end{aligned} \quad (5.44)$$

for the relevant operators \hat{O} and direction μ in the dynamics: thus obtaining the fermion self-interaction on the lattice entirely in terms of the mode functions.

This mode function expression of the correlators (5.40b) and the evolution (5.42) of the discrete modes together with the definition of the electric field (5.36) in terms of the gauge link, and the discretized, classical, Higgs dynamics (5.34d) may fully define the evolution of the quantized system on the lattice.

5.4.4 Numerical Evolution: Mode Functions

Rearranging the evolution equations of the electric field (5.40b), fermion modes (5.42) and the Higgs phase (5.40d) provides iteration relations for evolving the system:

$$\begin{aligned}
E_i(X) &= E_i(X-0) - \sum_j \frac{\Delta x_0}{\Delta x_i (\Delta x_j)^2} \frac{\hbar c}{q} \text{Im} \{U_{ij}(X) - U_{ji}(X-j)\} \\
&+ \Delta x_0 \frac{\mu_0 c q}{\hbar} \text{Im} \left\{ \langle T \hat{\Psi}(X) \gamma^i U_i(X) \hat{\Psi}(X+i) \rangle \right\} \\
&- \Delta x_0 \frac{\mu_0 c q}{\hbar} r_w \text{Im} \left\{ \langle T \hat{\Psi}(X) U_i(X) \hat{\Psi}(X+i) \rangle \right\} \\
&- \frac{\Delta x_0}{\Delta x_i} \frac{\mu_0 c e}{\hbar} \rho^2(X) \text{Im} \left\{ \Theta^\dagger(X) U_i^{e/q} \Theta(X+i) \right\} + \Delta x_0 \mu_0 c j_i(X), \tag{5.45a}
\end{aligned}$$

$$\begin{aligned}
\psi_{\mathbf{K},s}^{(A)}(X+0) &= \psi_{\mathbf{K},s}^{(A)}(X-0) \\
&+ \sum_i \frac{\Delta x_0}{\Delta x_i} \gamma^0 \gamma^i \left(U_i(X) \psi_{\mathbf{K},s}^{(A)}(X+i) - U_i^\dagger(X-i) \psi_{\mathbf{K},s}^{(A)}(X-i) \right) + \frac{mc}{\hbar} \psi_{\mathbf{K},s}^{(A)}(X) \\
&- \sum_i \frac{\Delta x_0}{\Delta x_i} r_w \gamma^0 \left(U_i(X) \psi_{\mathbf{K},s}^{(A)}(X+i) \right. \\
&\left. - 2\psi_{\mathbf{K},s}^{(A)}(X) + U_i^\dagger(X-i) \psi_{\mathbf{K},s}^{(A)}(X-i) \right), \tag{5.45b}
\end{aligned}$$

$$\begin{aligned}
S(X) &= S(X-0) + \sum_i \frac{\Delta x_0}{(\Delta x_i)^2} \left(\text{Im} \left\{ \Theta^\dagger(X) U_i^{e/q}(X) \Theta(X+i) \right\} \right. \\
&\left. - \frac{\rho^2(X-i)}{\rho^2(X)} \text{Im} \left\{ \Theta^\dagger(X-i) U_i^{e/q}(X-i) \Theta(X) \right\} \right), \tag{5.45c}
\end{aligned}$$

where the expansion (5.44) in the modes on renormalization provides the standard method to determine the correlators. This evolution further entails determining both the gauge and phase links. These may be obtained respectively through the definition on the lattice of the electric field (5.36) and the variable $S(X)$ (5.35) expressing the Higgs evolution.

The electric field definition in the temporal gauge implies

$$\text{Im} \left\{ U_i(X+0) U_i^\dagger(X) \right\} = \Delta x_0 \Delta x_1 \frac{q}{\hbar c} E_i(X);$$

the unitarity of the gauge links, in general, hence yields

$$\text{Re} \left\{ U_i(X+0)U_i^\dagger(X) \right\} = \pm \sqrt{\left(1 - \left(\Delta x_0 \Delta x_i \frac{q}{\hbar c} E_i(X) \right)^2 \right)},$$

while the unitarity, in particular, where $E_i = 0$ consequently determines

$$\text{Re} \left\{ U_i(X+0)U_i^\dagger(X) \right\} = + \sqrt{\left(1 - \left(\Delta x_0 \Delta x_i \frac{q}{\hbar c} E_i(X) \right)^2 \right)}.$$

This result on rearrangement therefore provides the iteration relation to evolve the gauge-link terms in the dynamics:

$$U_i(X+0) = \left(+ \sqrt{\left(1 - \left(\Delta x_0 \Delta x_i \frac{q}{\hbar c} E_i(X) \right)^2 \right)} + i \Delta x_0 \Delta x_i \frac{q}{\hbar c} E_i(X) \right) U_i(X). \quad (5.46)$$

Likewise, the constructed Higgs-variable $S(X)$ implies

$$\text{Im} \left\{ \Theta^\dagger(X)\Theta(X+0) \right\} = \Delta x_0 S(X),$$

while the unitarity of phase-link in general and at $S(X) = 0$, together, determine

$$\text{Re} \left\{ \Theta^\dagger(X)\Theta(X+0) \right\} = + \sqrt{\left(1 - (\Delta x_0 S(X))^2 \right)};$$

and hence, the constructed variable $S(X)$ yields the iteration relation to evolve phase link:

$$\Theta(X+0) = \left(+ \sqrt{\left(1 - (\Delta x_0 S(X))^2 \right)} + i \Delta x_0 S(X) \right) \Theta(X). \quad (5.47)$$

This expression, the equivalent gauge-link evolution (5.46), and the field iteration relations (5.45) with the mode function expansion (5.44) of the correlators fully specify the dynamics to evolve the system numerically from a given initial state.

Confirming the constraint (5.40a) on the lattice to machine-level accuracy in addition offers a convenient indicator for validating the reliability of the mode function simulation.

5.4.5 The Ensemble Approach

A summation over the discrete lattice, mode-space replaces the integral over this space in the continuum, to define the discretized $\Psi_{M,c}$ and $\Psi_{F,c}$ fields:

$$\Psi_{M,c}(x) = \sqrt{\frac{\hbar c}{2}} V_x \sum_s \sum_{\mathbf{K}} \frac{\Delta k_1}{2\pi} \frac{\Delta k_2}{2\pi} \frac{\Delta k_3}{2\pi} \frac{1}{2\omega_{\mathbf{K}}} \left[\xi_{\mathbf{K},s,c} \psi_{\mathbf{K},s}^{(U)}(X) + \zeta_{\mathbf{K},s,c} \psi_{\mathbf{K},s}^{(V)}(X) \right],$$

$$\Psi_{F,c}(x) = \sqrt{\frac{\hbar c}{2}} V_x \sum_s \sum_{\mathbf{K}} \frac{\Delta k_1}{2\pi} \frac{\Delta k_2}{2\pi} \frac{\Delta k_3}{2\pi} \frac{1}{2\omega_{\mathbf{K}}} \left[\xi_{\mathbf{K},s,c} \psi_{\mathbf{K},s}^{(U)}(X) - \zeta_{\mathbf{K},s,c} \psi_{\mathbf{K},s}^{(V)}(X) \right],$$

and each evolves according to the discretized, fermionic equation of motion (5.40c).

The independence constraints on the two sets of random numbers at each wave-vector value are imposed to be identical to the continuum case; and with each set again chosen to form a Gaussian distribution of mean zero but with a variance in the discrete case equal to

$$\langle \xi_{\mathbf{K},s} \xi_{\mathbf{L},r} \rangle_E = \langle \zeta_{\mathbf{K},s} \zeta_{\mathbf{L},r} \rangle_E = V_x^{-2} (2\pi)^3 \delta_{sr} \frac{\delta_{\mathbf{KL}}^3}{\Delta k_1 \Delta k_2 \Delta k_3}.$$

These conditions along with the vacuum-state definition (5.13) consequently yield equality between the lattice, quantum correlators and the equivalent variance of the ensemble fields:

$$\begin{aligned} \langle \hat{\Psi}(X) \hat{O} \hat{\Psi}(X + \mu) \rangle = \\ - \frac{1}{2} \left(\langle \bar{\Psi}_M(X) \hat{O} \Psi_F(X + \mu) \rangle_E + \langle \bar{\Psi}_F(X) \hat{O} \Psi_M(X + \mu) \rangle_E \right). \end{aligned} \quad (5.48)$$

Setting in particular the real- and imaginary-part of both the $\xi_{\mathbf{K},s,c}$, and the

$\zeta_{\mathbf{K},s,c}$ identically to the continuum case except in the non-trivial cases imposing the variance

$$\frac{1}{2} V_x^{-2} (2\pi)^3 \delta_{sr} \frac{\delta_{\mathbf{KL}}^3}{\Delta k_1 \Delta k_2 \Delta k_3} \quad (5.49)$$

may produce the discretized constraints on the complex-numbers.

The discrete ensemble fields importantly each comprise a linear combination of the mode functions. This with also the linearity of the mode function dynamics (5.42), equivalently to the continuum (see Section 5.2.3), determines the ensemble fields on the lattice each satisfy the discrete mode dynamics (5.42). Establishing the equality (5.48) at the initial time likewise also ensures the evolved ensemble-fields may yield the quantum-correlators at subsequent times. These correlator expansions thus can be consistently replaced by the ensemble variance in the electric field equations (5.40a) and (5.40b).

Equal sample-sizes of the random sets, identically to the continuum case, may define the ensemble in practice, and accordingly the statistical properties involve the discrete average over the N_E samples. These reduced sets approximating the Gaussian-distribution may yield a variance closely approximating the fermionic correlators at any instant; and hence this finite sample may highly accurately determine the fermionic contribution in the electric field equations.

These finite-ensemble equations and the ensemble-field dynamics, together with the definition of the electric field on the lattice (5.36), and the classical Higgs-dynamics (5.34d) with the variable (5.35) specifying the phase-link evolution comprises the ensemble-field method for determining the semi-quantized dynamics on the lattice.

5.4.6 Numerical Evolution: Ensemble Method

The determined iteration-relations (5.45), (5.46) and (5.47) again for the ensemble case fully specify the numerical evolution from an initial state except with the correlators determined through the variances (5.48) of the ensemble fields.

Confirming the constraint (5.40a) to machine-level accuracy on computing the renormalized correlator through the ensemble-variance (5.48) again for this method offers a convenient indicator for assuring the validity of the simulation.

5.4.7 An Ansatz for the Fields

The symmetry of the superconducting sheets defined through the Higgs modulus (5.4) and the homogeneity of the electromagnetic fields and fermionic fields remain on discretization; the ansatz determined in the continuum for the Higgs phase (5.17a) and the gauge field (5.19) generated further from the chosen external-current (5.18) hence likewise remain valid on the lattice.

This homogeneity perpendicular to the z -direction and the quantum nature of the fermions also recreate on the lattice precisely the conditions in the continuum indicating the fermion modes comprise the vacuum solutions with the factor in the z -direction modified; and hence these considerations likewise may reasonably determine the mode ansatz on the lattice. The vacuum configuration on the lattice – through effectively setting the gauge field to zero in the interacting case (5.42) – specifically satisfy

$$\sum_{\mu} \frac{1}{2\Delta x_{\mu}} \gamma^{\mu} (\Psi(X + \mu) - \Psi(X - \mu)) + \frac{mc}{\hbar} \Psi(X) - \sum_i \frac{1}{\Delta x_i} \frac{r_w}{2} (\Psi(X + i) - 2\Psi(X) + \Psi(X - i)) = 0, \quad (5.50)$$

with the standard positive- and negative-energy solutions respectively specifying⁹

$$\begin{aligned} \psi_{\mathbf{k},s}^{(+)}(X) &= e^{iK \cdot X} U_{\mathbf{K},s}, \\ \psi_{\mathbf{k},s}^{(-)}(X) &= e^{-iK \cdot X} V_{\mathbf{K},s}; \end{aligned} \quad (5.51)$$

⁹For further details on the lattice solutions to the vacuum-dynamics see also (5.6.1).

and the modification in the z -direction hence yields

$$\begin{aligned}\psi_{(K_1, K_2, \Lambda, s)}^{(U)}(X) &= e^{iK_1 X_1} e^{iK_2 X_2} \chi_{(K_1, K_2, \Lambda, s)}^{(U)}(T, X_3), \\ \psi_{(-K_1, -K_2, -\Lambda, s)}^{(V)}(X) &= e^{-iK_1 X_1} e^{-iK_2 X_2} \chi_{(-K_1, -K_2, -\Lambda, s)}^{(V)}(T, X_3).\end{aligned}$$

Substituting this form into the discrete mode-expansion (5.41) and similarly to the continuum case, switching the z -variable to sum over the ansatz label¹⁰ Λ yields the expansion in the mode ansatz; with the ladder operators likewise relabelled to denote association to the variable in the modified direction:

$$\begin{aligned}\hat{\Psi}(X) &= \sqrt{\hbar c V_x} \sum_{K_1, K_2, \Lambda, s} \frac{\Delta k_1}{(2\pi)} \frac{\Delta k_2}{(2\pi)} \frac{\Delta \lambda}{(2\pi)} \\ &\quad \left[\hat{b}_{(K_1, K_2, \Lambda, s)} e^{iK_1 X_1} e^{iK_2 X_2} \chi_{(K_1, K_2, \Lambda, s)}^{(U)}(T, X_3) \right. \\ &\quad \left. + \hat{d}_{(K_1, K_2, \Lambda, s)}^\dagger e^{-iK_1 X_1} e^{-iK_2 X_2} \chi_{(-K_1, -K_2, -\Lambda, s)}^{(V)}(T, X_3) \right].\end{aligned}$$

The ladder-operator anti-commutators on the lattice correspondingly are asserted to satisfy

$$\begin{aligned}\{\hat{b}_{(K_1, K_2, \Lambda, s)}, \hat{d}_{(L_1, L_2, \Upsilon, r)}\} &= 0, \\ \{\hat{b}_{(K_1, K_2, \Lambda, s)}^\dagger, \hat{d}_{(L_1, L_2, \Upsilon, r)}\} &= 0, \\ \{\hat{b}_{(K_1, K_2, \Lambda, s)}, \hat{b}_{(L_1, L_2, \Upsilon, r)}^\dagger\} &= V_x^{-2} (2\pi)^3 \delta_{sr} \frac{\delta_{K_1 L_1} \delta_{K_2 L_2} \delta_{\Lambda \Upsilon}}{\Delta k_1 \Delta k_2 \Delta \lambda}, \\ \{\hat{d}_{(K_1, K_2, \Lambda, s)}, \hat{d}_{(L_1, L_2, \Upsilon, r)}^\dagger\} &= V_x^{-2} (2\pi)^3 \delta_{sr} \frac{\delta_{K_1 L_1} \delta_{K_2 L_2} \delta_{\Lambda \Upsilon}}{\Delta k_1 \Delta k_2 \Delta \lambda},\end{aligned}\tag{5.52}$$

where the ansatz label notably replaces the z wave-vector in the delta functions compared to the standard relations (5.43)¹¹.

¹⁰The relation of the measure $\Delta\lambda/(2\pi)$ to the known, physical quantities in the system is expressly considered subsequently on Neumann boundaries in Section 5.6.1 when examining the relation of the ansatz mode functions to the fermion anti-commutator.

¹¹The validity of these ladder anti-commutators may be determined through establishing these reproduces the field anti-commutator (see footnote 1). This procedure will be expressly

Completing equivalently to the continuum the transformation $K_1 \rightarrow -K_1$, $K_2 \rightarrow -K_2$, $\Lambda \rightarrow -\Lambda$ in the lattice ansatz-expansion yields

$$\begin{aligned} \hat{\Psi}(X) = \sqrt{\hbar c} V_x \sum_{K_1, K_2, \Lambda, s} \frac{\Delta k_1}{(2\pi)} \frac{\Delta k_2}{(2\pi)} \frac{\Delta \lambda}{(2\pi)} \\ \left[\hat{b}_{(K_1, K_2, \Lambda, s)} e^{iK_1 X_1} e^{iK_2 X_2} \chi_{(K_1, K_2, \Lambda, s)}^{(U)}(T, X_3) \right. \\ \left. + \hat{d}_{(-K_1, -K_2, -\Lambda, s)}^\dagger e^{iK_1 X_1} e^{iK_2 X_2} \chi_{(K_1, K_2, \Lambda, s)}^{(V)}(T, X_3) \right]. \end{aligned} \quad (5.53)$$

Both the positive- and the negative-energy ansatz in the expansion on the lattice as in the continuum thereby reduce to the identical, general form

$$\psi_{(K_1, K_2, \Lambda, s)}^{(A)}(X) = e^{iK_1 X_1} e^{iK_2 X_2} \chi_{(K_1, K_2, \Lambda, s)}^{(A)}(T, X_3), \quad (5.54)$$

thus simplifying the fermion ansatz.

Substituting the gauge and Higgs-phase ansatz on the lattice into the electric field equations (5.40a) and (5.40b), and likewise into the Higgs dynamics (5.40d), demonstrated for the ansatz expansion with Neumann boundaries on the lattice subsequently (Section 5.6.1).

with both the modulus structure (5.4) and external current (5.18) discretized yields

$$\begin{aligned} & \frac{q}{\hbar} \text{Im} \{ \langle \hat{\Psi}(X) \gamma^0 \hat{\Psi}(X+0) \rangle \} \\ & + \frac{1}{\Delta x_0} \frac{e}{\hbar} \rho^2(T, X_3) \text{Im} \{ \Theta^\dagger(T, X_3) \Theta(T+0, X_3) \} - j_0(X) = 0, \end{aligned} \quad (5.55)$$

$$\frac{q}{\hbar} \text{Im} \left\{ \langle \hat{\Psi}(X) \gamma^2 \hat{\Psi}(X+2) \rangle \right\} - \frac{q}{\hbar} r_w \text{Im} \left\{ \langle \hat{\Psi}(X) \hat{\Psi}(X+2) \rangle \right\} = 0, \quad (5.56)$$

$$\begin{aligned} & \frac{q}{\hbar} \text{Im} \left\{ \langle \hat{\Psi}(X) \gamma^3 \hat{\Psi}(X+3) \rangle \right\} - \frac{q}{\hbar} r_w \text{Im} \left\{ \langle \hat{\Psi}(X) \hat{\Psi}(X+3) \rangle \right\} \\ & - \frac{1}{\Delta x_3} \frac{e}{\hbar} \rho^2(T, X_3) \text{Im} \{ \Theta^\dagger(T, X_3) \Theta(T, X_3+3) \} = 0, \end{aligned} \quad (5.57)$$

$$\begin{aligned} & \frac{1}{\Delta x_0} \frac{1}{\mu_0 c} (E_1(T, X_3) - E_1(T-0, X_3)) \\ & + \frac{1}{\Delta x_1 (\Delta x_3)^2} \frac{\hbar}{q \mu_0} \text{Im} \{ U_{13}(T, X_3) - U_{31}(T, X_3-3) \} \\ & - \frac{q}{\hbar} \text{Im} \left\{ \langle \hat{\Psi}(X) \gamma^1 U_1(T, X_3) \hat{\Psi}(X+1) \rangle \right\} \\ & + \frac{q}{\hbar} r_w \text{Im} \left\{ \langle \hat{\Psi}(X) U_1(T, X_3) \hat{\Psi}(X+1) \rangle \right\} \\ & + \frac{1}{\Delta x_1} \frac{e}{\hbar} \rho^2(T, X_3) \text{Im} \left\{ U_1^{e/q}(T, X_3) \right\} - j_1(X) = 0, \end{aligned} \quad (5.58)$$

$$\begin{aligned} & \frac{1}{\Delta x_0} \rho^2(T, X_3) (S(T, X_3) - S(T-0, X_3)) \\ & - \frac{1}{(\Delta x_3)^2} \left(\rho^2(T, X_3) \text{Im} \left\{ \Theta^\dagger(T, X_3) \Theta(T, X_3+3) \right\} \right. \\ & \left. - \rho^2(T, X_3-3) \text{Im} \left\{ \Theta^\dagger(T, X_3-3) \Theta(T, X_3) \right\} \right) = 0; \end{aligned} \quad (5.59)$$

and where

$$E_1(T, X_3) = \frac{-i}{\Delta x_0 \Delta x_1} \frac{\hbar c}{2q} (U_{01}(T, X_3) - U_{10}(T, X_3)) \quad (5.60)$$

results on substituting the gauge ansatz into the electric field definition (5.36).

Likewise, the gauge, Higgs phase and mode ansatz substituted into the mode

function dynamics (5.11) with the modulus structure determines

$$\begin{aligned}
& \frac{1}{\Delta x_0} \frac{1}{2} \gamma^0 \left(\chi_{(K_1, K_2, \Lambda, s)}^{(A)}(T+0, X_3) - \chi_{(K_1, K_2, \Lambda, s)}^{(A)}(T-0, X_3) \right) \\
& + \frac{1}{\Delta x_1} \gamma^1 i \sin \left(\Delta x_1 \left[K_1 - \frac{q}{\hbar} A_1(T, X_3) \right] \right) \chi_{(K_1, K_2, \Lambda, s)}^{(A)}(T, X_3) \\
& + \frac{1}{\Delta x_2} \gamma^2 i \sin(\Delta x_2 K_2) \chi_{(K_1, K_2, \Lambda, s)}^{(A)}(T, X_3) \\
& + \frac{1}{\Delta x_3} \frac{1}{2} \gamma^3 \left(\chi_{(K_1, K_2, \Lambda, s)}^{(A)}(T, X_3 + 3) - \chi_{(K_1, K_2, \Lambda, s)}^{(A)}(T, X_3 - 3) \right) \\
& + \frac{mc}{\hbar} \chi_{(K_1, K_2, \Lambda, s)}^{(A)}(T, X_3) \\
& + \frac{1}{\Delta x_1} r_w \left(\cos \left(\Delta x_1 \left[K_1 - \frac{q}{\hbar} A_1(T, X_3) \right] \right) - 1 \right) \chi_{(K_1, K_2, \Lambda, s)}^{(A)}(T, X_3) \\
& + \frac{1}{\Delta x_2} r_w (\cos(\Delta x_2 K_2) - 1) \chi_{(K_1, K_2, \Lambda, s)}^{(A)}(T, X_3) \\
& + \frac{1}{\Delta x_3} \frac{r_w}{2} \left(\chi_{(K_1, K_2, \Lambda, s)}^{(A)}(T, X_3 + 3) - 2\chi_{(K_1, K_2, \Lambda, s)}^{(A)}(T, X_3) \right. \\
& \left. + \chi_{(K_1, K_2, \Lambda, s)}^{(A)}(T, X_3 - 3) \right) = 0. \tag{5.61}
\end{aligned}$$

Substituting the mode ansatz into the discrete, fermionic correlator, on ap-

plying the ladder anti-commutator (5.52) and vacuum-state definition (5.13) provides

$$\begin{aligned}
\langle \hat{\Psi}(X) \hat{O} \hat{\Psi}(X+0) \rangle &= \\
\frac{\hbar c}{2} \sum_{K_1, K_2, \Lambda, s} \frac{\Delta k_1}{(2\pi)} \frac{\Delta k_2}{(2\pi)} \frac{\Delta \lambda}{(2\pi)} &\left(\bar{\chi}_{(K_1, K_2, \Lambda, s)}^{(V)}(T, X_3) \hat{O} \chi_{(K_1, K_2, \Lambda, s)}^{(V)}(T+0, X_3) \right. \\
&\left. - \bar{\chi}_{(K_1, K_2, \Lambda, s)}^{(U)}(T, X_3) \hat{O} \chi_{(K_1, K_2, \Lambda, s)}^{(U)}(T+0, X_3) \right), \\
\langle \hat{\Psi}(X) \hat{O} U_1(T, X_3) \hat{\Psi}(X+1) \rangle &= \\
\frac{\hbar c}{2} \sum_{K_1, K_2, \Lambda, s} \frac{\Delta k_1}{(2\pi)} \frac{\Delta k_2}{(2\pi)} \frac{\Delta \lambda}{(2\pi)} &e^{i\Delta x_1(K_1 - qA_1(T, X_3))} \\
&\left(\bar{\chi}_{(K_1, K_2, \Lambda, s)}^{(V)}(T, X_3) \hat{O} \chi_{(K_1, K_2, \Lambda, s)}^{(V)}(T, X_3) \right. \\
&\left. - \bar{\chi}_{(K_1, K_2, \Lambda, s)}^{(U)}(T, X_3) \hat{O} \chi_{(K_1, K_2, \Lambda, s)}^{(U)}(T, X_3) \right), \\
\langle \hat{\Psi}(X) \hat{O} \hat{\Psi}(X+2) \rangle &= \\
\frac{\hbar c}{2} \sum_{K_1, K_2, \Lambda, s} \frac{\Delta k_1}{(2\pi)} \frac{\Delta k_2}{(2\pi)} \frac{\Delta \lambda}{(2\pi)} &e^{i\Delta x_2 K_2} \left(\bar{\chi}_{(K_1, K_2, \Lambda, s)}^{(V)}(T, X_3) \hat{O} \chi_{(K_1, K_2, \Lambda, s)}^{(V)}(T, X_3) \right. \\
&\left. - \bar{\chi}_{(K_1, K_2, \Lambda, s)}^{(U)}(T, X_3) \hat{O} \chi_{(K_1, K_2, \Lambda, s)}^{(U)}(T, X_3) \right), \\
\langle \hat{\Psi}(X) \hat{O} \hat{\Psi}(X+3) \rangle &= \\
\frac{\hbar c}{2} \sum_{K_1, K_2, \Lambda, s} \frac{\Delta k_1}{(2\pi)} \frac{\Delta k_2}{(2\pi)} \frac{\Delta \lambda}{(2\pi)} &\left(\bar{\chi}_{(K_1, K_2, \Lambda, s)}^{(V)}(T, X_3) \hat{O} \chi_{(K_1, K_2, \Lambda, s)}^{(V)}(T, X_3+3) \right. \\
&\left. - \bar{\chi}_{(K_1, K_2, \Lambda, s)}^{(U)}(T, X_3) \hat{O} \chi_{(K_1, K_2, \Lambda, s)}^{(U)}(T, X_3+3) \right). \tag{5.62}
\end{aligned}$$

These equations, equivalently to the continuum, thus simplify the dynamics to a one-dimensional system in the z -coordinate with the correlator involving a summation over a three-dimensional mode-space.

The Higgs-field phase again as in the continuum entirely decouples from the gauge and fermionic fields ensuring likewise on the lattice that the phase may be neglected throughout the evolution – in effect setting $\theta(T, X_3) = 0$ to satisfy the

evolution equation (5.34d) – without constraint on the primary interactions.

This assertion, hence, eliminates the phase-evolution equation from the dynamics; and further determines that the gauge-field equations (5.55), (5.56) and (5.57), involving the phase, respectively simplify to

$$\frac{q}{\hbar} \text{Im} \{ \langle \hat{\Psi}(X) \gamma^0 \hat{\Psi}(X+0) \rangle \} - j_0(X) = 0, \quad (5.63)$$

$$\frac{q}{\hbar} \text{Im} \left\{ \langle \hat{\Psi}(X) \gamma^2 \hat{\Psi}(X+2,3) \rangle \right\} - \frac{q}{\hbar} r_w \text{Im} \left\{ \langle \hat{\Psi}(X) \hat{\Psi}(X+2,3) \rangle \right\} = 0. \quad (5.64)$$

These results thus specify the constraints on the gauge field in the ansatz case on the lattice; while the electric field dynamics (5.58) and mode function ansatz-equation (5.61), together with the corresponding correlator expansions (5.62) and the definition of the electric field (5.60) in the ansatz may thus determine the quantized evolution on the lattice under the inherent symmetries of the system.

5.4.8 Numerical Evolution: Ansatz Case

Rearranging the electric field evolution (5.58) and the mode-ansatz dynamics (5.61) yields iteration relations to numerically evolve the ansatz case:

$$\begin{aligned}
E_1(T, X_3) &= E_1(T - 0, X_3) \\
&- \frac{\Delta x_0}{\Delta x_1 (\Delta x_3)^2} \frac{\hbar c}{q} \text{Im} \{ U_{13}(T, X_3) - U_{31}(T, X_3 - 3) \} \\
&+ \Delta x_0 \frac{\mu_0 c q}{\hbar} \text{Im} \left\{ \langle \hat{\Psi}(X) \gamma^1 U_1(T, X_3) \hat{\Psi}(X + 1) \rangle \right\} \\
&- \frac{q}{\hbar} r_w \text{Im} \left\{ \langle \hat{\Psi}(X) U_1(T, X_3) \hat{\Psi}(X + 1) \rangle \right\} \\
&- \frac{\Delta x_0}{\Delta x_1} \frac{\mu_0 c e}{\hbar} \rho^2(X) \text{Im} \left\{ U_1^{e/q}(T, X_3) \right\} + \Delta x_0 \mu_0 c j_1(X), \tag{5.65a}
\end{aligned}$$

$$\begin{aligned}
\gamma^0 \chi_{(K_1, K_2, \Lambda, s)}^{(A)}(T + 0, X_3) &= \chi_{(K_1, K_2, \Lambda, s)}^{(A)}(T - 0, X_3) \\
&+ \frac{\Delta x_0}{\Delta x_1} \gamma^0 \gamma^1 2i \sin \left(\Delta x_1 \left[K_1 - \frac{q}{\hbar} A_1(T, X_3) \right] \right) \chi_{(K_1, K_2, \Lambda, s)}^{(A)}(T, X_3) \\
&+ \frac{\Delta x_0}{\Delta x_2} \gamma^0 \gamma^2 2i \sin(\Delta x_2 K_2) \chi_{(K_1, K_2, \Lambda, s)}^{(A)}(T, X_3) \\
&+ \frac{\Delta x_0}{\Delta x_3} \gamma^0 \gamma^3 \left(\chi_{(K_1, K_2, \Lambda, s)}^{(A)}(T, X_3 + 3) - \chi_{(K_1, K_2, \Lambda, s)}^{(A)}(T, X_3 - 3) \right) \\
&+ \Delta x_0 \gamma^0 \frac{2mc}{\hbar} \chi_{(K_1, K_2, \Lambda, s)}^{(A)}(T, X_3) \\
&+ \frac{\Delta x_0}{\Delta x_1} \gamma^0 2r_w \left(\cos \left(\Delta x_1 \left[K_1 - \frac{q}{\hbar} A_1(T, X_3) \right] \right) - 1 \right) \chi_{(K_1, K_2, \Lambda, s)}^{(A)}(T, X_3) \\
&+ \frac{\Delta x_0}{\Delta x_2} \gamma^0 2r_w (\cos(\Delta x_2 K_2) - 1) \chi_{(K_1, K_2, \Lambda, s)}^{(A)}(T, X_3) \\
&+ \frac{\Delta x_0}{\Delta x_3} \gamma^0 r_w \left(\chi_{(K_1, K_2, \Lambda, s)}^{(A)}(T, X_3 + 3) - 2\chi_{(K_1, K_2, \Lambda, s)}^{(A)}(T, X_3) \right. \\
&\left. + \chi_{(K_1, K_2, \Lambda, s)}^{(A)}(T, X_3 - 3) \right) = 0, \tag{5.65b}
\end{aligned}$$

with the fermionic correlators determined through the ansatz mode-expansion (5.62). This evolution further entails determining both the gauge field in the x -direction and the corresponding gauge-link.

The expression (5.46) determined on rearranging the discrete electric field again in the ansatz provides an iteration relation for evolving the gauge link.

Applying the gauge ansatz (5.19) and the corresponding electric field (5.60), though, readily determines that the gauge link dynamics depends purely on the z -coordinate:

$$U_1(T+0, X_3) = \left(+ \sqrt{\left(1 - \left(\Delta x_0 \Delta x_1 \frac{q}{\hbar c} E_1(T, X_3)\right)^2\right)} + i \Delta x_0 \Delta x_1 \frac{q}{\hbar c} E_1(T, X_3) \right) U_1(T, X_3). \quad (5.66)$$

Substituting the (evolved) gauge link into the definition (5.33a) of the link hence yields

$$A_1(T, X_3) = \frac{i}{\Delta x_1} \frac{\hbar}{q} \ln(U_1(T, X_3)),$$

to thus determine the evolution of the gauge field.

This relation and the gauge-link evolution (5.66), with the field iteration relations (5.65) and the ansatz expansion (5.62) of the correlators on the lattice fully specify the dynamics to evolve the system numerically from a given initial state.

Confirming, also, the constraint equations (5.63) and (5.64) on the lattice to machine-level accuracy offers a test to confirm the self-consistency of the ansatz; and, further, may provide assurance of reliability of the simulation.

5.5 Lattice Boundary Conditions

5.5.1 Periodic Boundaries

Asserting periodic boundary conditions on the lattice forms the standard method to compute those spatial derivatives across the lattice boundaries. This effectively imposes a circular geometry in each orthogonal direction on the lattice¹²; the wavefunctions on the lattice thus correspond to a complete rotation

¹²The boundary conditions correspond, most intuitively, to an infinite space formed of the finite lattice-volume periodically repeated in each direction or equivalently, to a (spatial) three-dimensional torus.

of the field in each periodic direction.

Implementing a complete rotation on a Bosonic fields simply returns the field to the initial value. The field value at the site beyond the upper or lower boundary in the sequence of lattice sites $n_i = [0, N_i - 1]$, under the periodic constraints therefore respectively satisfy

$$\begin{aligned} f(X)|_{n_i=-1} &= f(X)|_{n_i=N_i-1}, \\ f(X)|_{n_i=N} &= f(X)|_{n_i=0}. \end{aligned}$$

Applying the periodic boundary conditions to the superconductor system accordingly imposes:

$$\begin{aligned} E_j(X)|_{n_i=-1} &= E_j(X)|_{n_i=N_i-1}, \\ E_j(X)|_{n_i=N_i} &= E_j(X)|_{n_i=0}, \\ A_\mu(X)|_{n_i=-1} &= A_\mu(X)|_{n_i=N_i-1}, \\ A_\mu(X)|_{n_i=N_i} &= A_\mu(X)|_{n_i=0}, \\ \theta(X)|_{n_i=N_i} &= \theta(X)|_{n_i=0}, \\ \theta(X)|_{n_i=-1} &= \theta(X)|_{n_i=N_i-1}. \end{aligned} \tag{5.67}$$

The spin-half property of a fermion field determines that conducting a complete rotation of the field negates the initial value. This therefore implies that in each periodic direction, the fermion field-value respectively at the adjacent site beyond the upper and lower boundary satisfies

$$\begin{aligned} \Psi(X)|_{n_i=-1} &= -\Psi(X)|_{n_i=N_i-1}, \\ \Psi(X)|_{n_i=N_i} &= -\Psi(X)|_{n_i=0}. \end{aligned} \tag{5.68}$$

These and the conditions (5.67) on the bosonic fields provide the complete set of periodic boundary conditions to evolve the dynamics on the lattice.

5.5.2 Neumann Boundaries

Implementing Neumann boundaries in the z -direction on the lattice enables consistently setting independent initial conditions on the bounding, x - y planes¹³.

The Neumann conditions on a scalar field in 3+1D impose the gradient normal to the bounding surface vanishes. Forming the standard, first-order approximation of the differential on a cuboidal lattice specifies the discretized derivative in the z -direction comprises¹⁴

$$\frac{f(X+3) - f(X)}{\Delta x_3}.$$

Further, asserting the sites at $n_3 = -1$ and $n_3 = N_3 - 1$ respectively form the upper and lower boundaries in the z -direction hence determines the derivatives normal to the z -boundaries:

$$\frac{f(X)|_{n_3=0} - f(X)|_{n_3=-1}}{\Delta x_3},$$

$$\frac{f(X)|_{n_3=N_3} - f(X)|_{n_3=N_3-1}}{\Delta x_3}.$$

Applying the Neumann boundary condition to the discretized gradients corre-

¹³In particular, this will enable consistently setting an external current aligned in opposite directions at the opposing boundaries in the z -direction. This may be used to generate a uniform magnetic field of identical orientation in the two regions outside the region enclosed by the superconductor; or a single, electromagnetic pulse travelling along the z -axis may be generated from an oscillating current at only one boundary.

¹⁴The standard, first-order approximation of the differential may alternatively impose $\frac{f(X) - f(X-3)}{\Delta x_3}$ to define the discretized derivative on the lattice. This in the scalar case yields an identical result to the original definition except asserting the boundaries at the sites $n_3 = 0$ and $n_3 = N_3$. The chosen derivative and the associated boundary site simply offers a definite convention for obtaining consistent, explicit boundary conditions. (see also footnote 16)

spondingly yields

$$f(X)|_{n_3=-1} = f(X)|_{n_3=0},$$

$$f(X)|_{n_3=N_3} = f(X)|_{n_3=N_3-1}.$$

These constraints on the super-conducting system therefore impose the Higgs phase on the z -boundaries satisfies

$$\theta(X)|_{n_3=-1} = \theta(X)|_{n_3=0},$$

$$\theta(X)|_{n_3=N_3} = \theta(X)|_{n_3=N_3-1}.$$

Implementing the Neumann conditions further on a 3+1D vector imposes the spatial component perpendicular to the boundary vanishes while the gradient of those parallel to the boundary vanish¹⁵. The standard, first-order approximation of the differential hence implies the components parallel to the z boundaries, under the Neumann constraints satisfy

$$a_{1/2}(X)|_{n_3=-1} = a_{1/2}(X)|_{n_3=0},$$

$$a_{1/2}(X)|_{n_3=N_3} = a_{1/2}(X)|_{n_3=N_3-1};$$

¹⁵These conditions on the scalar and vector are equivalent to considering the Neumann conditions impose a reflectional symmetry at the boundary.

while the condition on the perpendicular component yields¹⁶

$$\begin{aligned} a_3(X)|_{n_3=-1} &= 0, \\ a_3(X)|_{n_3=N_3-1} &= 0. \end{aligned}$$

Hence, the electric field components under the Neumann boundary conditions satisfy

$$\begin{aligned} E_{1/2}(X)|_{n_3=-1} &= E_{1/2}(X)|_{n_3=0}, & E_3(X)|_{n_3=-1} &= 0, \\ E_{1/2}(X)|_{n_3=N_3} &= E_{1/2}(X)|_{n_3=N_3-1}, & E_3(X)|_{n_3=N_3-1} &= 0, \end{aligned} \quad (5.69)$$

and likewise the boundary conditions on the gauge field imply

$$\begin{aligned} A_{1/2}(X)|_{n_3=-1} &= A_{1/2}(X)|_{n_3=0}, & A_3(X)|_{n_3=-1} &= 0, \\ A_{1/2}(X)|_{n_3=N_3} &= A_{1/2}(X)|_{n_3=N_3-1}, & A_3(X)|_{n_3=N_3-1} &= 0. \end{aligned} \quad (5.70)$$

Further, the vector boundary conditions impose the fermion current satisfies

$$\begin{aligned} \frac{q}{\hbar} \text{Im} \left\{ \langle T \hat{\Psi}(X + \gamma)^{1/2} U_{1/2}(X) \hat{\Psi}(X + 1/2) \rangle \right\} \Big|_{X=X_B} &= \\ \frac{q}{\hbar} \text{Im} \left\{ \langle T \hat{\Psi}(X + 3) \gamma^{1/2} U_{1/2}(X) \hat{\Psi}(X + 1/2 + 3) \rangle \right\} \Big|_{X=X_B}, & \\ \frac{q}{\hbar} \text{Im} \left\{ \langle T \hat{\Psi}(X) \gamma^3 U_3(X) \hat{\Psi}(X + 3) \rangle \right\} \Big|_{X=X_B} &= 0, \end{aligned} \quad (5.71)$$

at the coordinates X_B on the z -boundaries; and the Neumann conditions likewise

¹⁶ The alternative choice of the derivative at the boundary yields, equivalently to the scalar field, an identical result to the employed definition, except assuming the boundaries occur at the sites $n_3 = 0$ and $n_3 = N$. This alternative boundary location further in the vector case interchanges the actual sites on the lattice where the field value vanishes: switching from fixing the field to zero at the sites where $n_3 = -1$ and $n_3 = N - 1$ to where $n_3 = 0$ and $n_3 = N$. Physically though, this variation in the boundary location only corresponds trivially to a shift in the positioning equal to a single lattice spacing.

constrain the Wilson current:

$$\begin{aligned} \frac{q}{\hbar} r_w \text{Im} \left\{ \langle T \hat{\Psi}(X + U_\mu)[1/2](X) \hat{\Psi}(X + 1/2) \rangle \right\} \Big|_{X=X_B} &= \\ \frac{q}{\hbar} r_w \text{Im} \left\{ \langle T \hat{\Psi}(X + 3)[1/2](X) \hat{\Psi}(X + 1/2 + 3) \rangle \right\} \Big|_{X=X_B}, & \\ \frac{q}{\hbar} r_w \text{Im} \left\{ \langle T \hat{\Psi}(X) U_3(X) \hat{\Psi}(X + 3) \rangle \right\} \Big|_{X=X_B} &= 0. \end{aligned} \quad (5.72)$$

These requirements on the fermionic currents may be attained at the upper and lower limits of the z -direction, through a matrix relating the field value across the boundary:

$$\begin{aligned} \Psi(X) \Big|_{n_3=-1} &= B_0 \Psi(X) \Big|_{n_3=0}, \\ \Psi(X) \Big|_{n_3=N} &= B_N \Psi(X) \Big|_{n_3=N-1}. \end{aligned}$$

Substituting these relations, accordingly, into the boundary conditions on the fermionic current, and applying the Neumann conditions on the gauge field (5.70) in the definition of the gauge link (5.33a) determines

$$\begin{aligned} B_{0/N}^\dagger \gamma^0 \gamma^{1/2} B_{0/N} &= \gamma^0 \gamma^{1/2}, & B_{0/N}^\dagger \gamma^0 \gamma^3 &= -\gamma^0 \gamma^3 B_{0/N}, \\ B_{0/N}^\dagger \gamma^0 B_{0/N} &= \gamma^0, & B_{0/N}^\dagger \gamma^0 &= \gamma^0 B_{0/N}. \end{aligned}$$

These matrices, in constraining the fermions, may reasonably be expected to derive from the γ -matrices central in determining the fermion behaviour. This constraint moreover on the z -direction indicates the γ^3 matrix in particular – related uniquely among the γ matrices to the z -direction – may reasonably be selected for creating the $B_{0/N}$ -matrices; and also the γ^5 without association to any direction in particular may in general be reasonably chosen to form the boundary matrices. The simplest combination of these matrices satisfying the

boundary conditions, hence, imposes

$$B_{0/N} = \pm i \gamma^5 \gamma^3, \quad (5.73)$$

with either the positive or negative combination possible (independently) at each boundary. Further, the definition of the Neumann conditions through the directions perpendicular to the boundary involve an inherent orientation, and, thus, indicate the choice of the relative sign of the matrices. Specifically, the operation

$$\pm i \left(\hat{N}_1 \gamma^5 \gamma^1 + \hat{N}_2 \gamma^5 \gamma^2 + \hat{N}_3 \gamma^5 \gamma^3 \right)$$

defines the projection of the matrix $\pm i \gamma^5 \gamma^i$ on the outward-orientated, normal vector-field $\hat{\mathbf{N}}(X)$ of the lattice. This in particular on the z -boundaries implies

$$\begin{aligned} \pm i \left(\hat{N}_1 \gamma^5 \gamma^1 + \hat{N}_2 \gamma^5 \gamma^2 + \hat{N}_3 \gamma^5 \gamma^3 \right) \Big|_{n_3=-1} &= \mp i \gamma^5 \gamma^3, \\ \pm i \left(\hat{N}_1 \gamma^5 \gamma^1 + \hat{N}_2 \gamma^5 \gamma^2 + \hat{N}_3 \gamma^5 \gamma^3 \right) \Big|_{n_3=N-1} &= \pm i \gamma^5 \gamma^3; \end{aligned}$$

and thus on comparison to the boundary constraints (5.73) indicates that the choice of the boundary matrices includes only those including a relative sign difference:

$$\begin{aligned} B_0 = +i \gamma^5 \gamma^3, & & B_0 = -i \gamma^5 \gamma^3, \\ & \text{or} & \\ B_N = -i \gamma^5 \gamma^3, & & B_N = +i \gamma^5 \gamma^3. \end{aligned}$$

(Notably, the imposed fermion-constraints in the continuum limit consistently reproduce those relations satisfying the continuum Neumann-conditions while enabling an arbitrary current in the x -direction on the z -boundaries: consistent with the ansatz assertion that current may exist in this direction. For further details see the Appendix B.) The positive option at the lower boundary and accordingly negative at the upper will be applied for definitiveness in the subse-

quent analysis¹⁷. These constraints on the fermion field together with the electric field conditions (5.69) and those on the gauge field (5.70) complete the Neumann boundaries in the z -direction on the cuboidal lattice.

Imposing the periodic conditions additionally on the remaining directions provides a complete set of boundary conditions in the $3 + 1$ D system.

The ansatz case significantly eliminates both the x - and y -directions expressly in the dynamics and thus the need to explicitly constrain the boundaries in these directions; these boundary conditions though shall implicitly determine the valid lattice-modes determining the fermion field-expansion. Applying the periodic boundaries matches the asserted uniformity in the x - and y -directions, and, thus, these boundary conditions may consistently provide the necessary, additional constraints on the x - and y -boundaries. The Neumann constraints on the z -direction, with also the periodic boundaries on the x and y -directions determining the lattice wave-vectors, therefore, form a complete and self-consistent set of boundary conditions for the ansatz case.

5.6 Initial Conditions

5.6.1 Fermion Field

Evolving the fermionic fields numerically in the mode, ensemble or ansatz case requires initially setting the mode functions for subsequent iteration through the leap-frog algorithm.

To obtain consistency with the correlator results requires the initial configuration in the vacuum state to match the assumption in the derivations. Further, the vacuum provides a tractable configuration to analytically determine the fermion mode functions. The standard, free-fermion solutions provide the vacuum dy-

¹⁷The particular choice of boundary matrix affects the precise form of the mode functions and notably the vacuum initial-modes satisfying the Neumann conditions (see Section 5.6.1); the difference in signs on the surface though would not be expected to create significant qualitative differences in the physical system.

namics in an infinite, continuum space; and the equivalent result on the lattice satisfies the discretized fermion dynamics with the periodic boundary conditions mimicking an infinite volume. These functions on the periodic lattice usefully remain the basis for determining the vacuum modes in this case imposing the Neumann boundary conditions.

Periodic Boundaries

The vacuum fermion-dynamics on the lattice (5.50) yield

$$\begin{aligned} \left(i\gamma^\mu S_\mu + \frac{M_L c}{\hbar} \right) U_{\mathbf{K}} &= 0, \\ - \left(i\gamma^\mu S_\mu - \frac{M_L c}{\hbar} \right) V_{\mathbf{K}} &= 0, \end{aligned}$$

for respectively the discrete, positive- and negative-energy configurations (5.51) where

$$\begin{aligned} S_i &\equiv \frac{\sin(K_i \Delta x_i)}{\Delta x_i}, \\ M_L &\equiv m + \frac{r_W \hbar}{c} \sum_i \frac{1}{\Delta x_i} (1 - \cos(K_i \Delta x_i)). \end{aligned}$$

These equations thus exactly reproduce the respective, standard vacuum-dynamics in the continuum except the variable S_μ replaces the continuous-variable k_μ and likewise the quantity M_L substitutes the free-fermion mass. (This equivalence notably establishes the correspondence of the fermionic wave-vectors and mass on the lattice to the equivalent physical quantities.) Applying accordingly the substitutions to the standard positive and negative-energy solutions in the continuum may therefore solve the positive- and negative-energy configurations

on the lattice:

$$\begin{aligned}\psi_{\mathbf{K},\pm}^{(+)}(X) &= \frac{1}{\sqrt{\omega_{\mathbf{K}}}} \begin{pmatrix} -\sqrt{\omega_{\mathbf{K}}\mathbb{I}_2 - \boldsymbol{\sigma} \cdot \mathbf{S}} \xi_{\pm} \\ \sqrt{\omega_{\mathbf{K}}\mathbb{I}_2 + \boldsymbol{\sigma} \cdot \mathbf{S}} \xi_{\pm} \end{pmatrix} e^{i\mathbf{K} \cdot X}, \\ \psi_{\mathbf{K},\pm}^{(-)}(X) &= \frac{1}{\sqrt{\omega_{\mathbf{K}}}} \begin{pmatrix} \sqrt{\omega_{\mathbf{K}}\mathbb{I}_2 - \boldsymbol{\sigma} \cdot \mathbf{S}} \xi_{\pm} \\ \sqrt{\omega_{\mathbf{K}}\mathbb{I}_2 + \boldsymbol{\sigma} \cdot \mathbf{S}} \xi_{\pm} \end{pmatrix} e^{-i\mathbf{K} \cdot X},\end{aligned}\quad (5.74)$$

where $\omega_{\mathbf{K}} = \sqrt{(M_L c/\hbar)^2 + \mathbf{S}^2}$ and the square root of the matrices is formed through the standard, Taylor-series of the matrix function¹⁸. The orthogonality of the mode functions asserted in creating the expansion further constrains the spinors ξ_s to an orthogonal set:

$$\xi_s \xi_r = 0, \quad s \neq r.$$

These for simplicity are typically constructed to form

$$\xi_s \xi_s = \mathbb{I}_2;$$

and thus these spinors satisfy both the orthonormal constraint and the vacuum mode-equation. The choice

$$\xi_+ = \begin{pmatrix} 1 \\ 0 \end{pmatrix}, \quad \xi_- = \begin{pmatrix} 0 \\ 1 \end{pmatrix},$$

in particular provides a simple configuration of the orthonormal spinors to specify the basis modes chosen in the initial expansion. The solutions thus define an orthogonal, vacuum configuration.

Asserting that the physical distances relate to the lattice-site index n_i in the

¹⁸See the Appendix C for the detailed form and a practical method to numerically compute this expansion.

respective direction through

$$X_1 = n_1 \Delta x_1,$$

and substituting either the positive or negative energy mode into the periodic boundary condition (5.68) on the corresponding direction consistently for both the modes implies

$$K_i = \frac{2\pi}{L_i} \left(e_i + \frac{1}{2} \right),$$

where e_i is the site index in the respective direction of the discrete mode-space. These constraints on the lattice wave-vectors thus ensure that the vacuum solutions satisfy the boundary conditions imposed in the x and y directions.

The positive- and negative-energy solutions accordingly may provide the orthogonal, vacuum modes for the initial conditions on the lattice satisfying the periodic boundary conditions¹⁹.

Neumann Boundaries

Imposing the Neumann Boundaries determines, in particular, the initial, vacuum-state fermions satisfy the constraints

$$\Psi(0, \mathbf{X})|_{n_3=-1} = B_0 \Psi(0, \mathbf{X})|_{n_3=0},$$

$$\Psi(0, \mathbf{X})|_{n_3=N} = B_N \Psi(0, \mathbf{X})|_{n_3=N-1},$$

with also the choice $B_0 = +i\gamma^5\gamma^3$ and $B_N = -i\gamma^5\gamma^3$ (see Section 5.5.2). This, hence, invalidates the standard, discrete vacuum configuration (5.74), and an

¹⁹The vacuum configuration on substitution into the mode and ansatz expansion with the respective ladder-commutators may satisfy the condition to reproduce the fermion anti-commutator (5.39) in particular at the initial time. These initial modes therefore validate the expansions and associated ladder-commutators throughout the evolution on the periodic lattice (see footnote 1).

This procedure to reproduce the anti-commutator in the ansatz case notably asserts the wave-vector in the z -direction initially forms the ansatz-variable. The process further involves setting the summation weighting $d\lambda/(2\pi)$ to yield the required anti-commutator; and the time invariance of the weighting hence determines the determined form remains valid throughout the evolution in the periodic case. This process is demonstrated explicitly in the subsequent Section (5.6.1) for the Neumann boundaries.

alternative vacuum configuration is required to satisfy the Neumann boundaries for the ansatz.

The linearity of the vacuum equation (5.50) yields the possibility for linear combinations of the standard results to likewise form further modes satisfying the dynamics. Creating in particular the combination

$$\tilde{\psi}_{\mathbf{K},s}^{(+)}(X) = e^{i(K_1 X_1 + K_2 X_2)} (e^{iK_3 X_3} U_{\mathbf{K},s} + i\gamma^5 \gamma^3 e^{-iK_3 X_3} U_{\mathbf{K},s}) \quad (5.75)$$

employs two terms each independently satisfying the vacuum equation (5.50) with the associated spinor $U_{\mathbf{K},s}$; these configurations importantly also involve only this single spinor from the standard orthogonal set and hence form an orthogonal set to satisfy the orthogonality assumption in defining the modes expansion. These linear combinations thus readily define an alternative set of mutually-orthogonal, vacuum solutions associated to the positive-energy modes.

Likewise, the linear combination

$$\tilde{\psi}_{\mathbf{K},s}^{(-)}(X) = e^{-i(K_1 X_1 + K_2 X_2)} (e^{-iK_3 X_3} V_{\mathbf{K},s} + i\gamma^5 \gamma^3 e^{iK_3 X_3} V_{\mathbf{K},s}) \quad (5.76)$$

incorporates two terms each independently satisfying the vacuum dynamics (5.50) with the associated spinor $V_{\mathbf{K},s}$ and involving only this single spinor from the standard orthogonal set; these hence define a set of mutually-orthogonal, vacuum solutions associated to the negative-energy modes²⁰.

Asserting that the z -coordinate relates to the lattice-site index n_3 in the z -direction through

$$X_3 = \left(n_3 + \frac{1}{2} \right) \Delta x_3 \quad (5.77)$$

ensures that the constructed, linear combinations both satisfy the Neumann con-

²⁰A more complex combination of the standard modes may conceivably form an orthogonal basis satisfying both the vacuum dynamics and the Neumann boundaries: potentially adding more terms involving a single spinor, combining distinct spinors of either the positive- or the negative-energy modes or mixing both the positive- and negative-energy spinors. These though involve an unnecessary, additional complexity; and the case of mixing the positive- and negative-energy solutions poses a particularly unclear form to interpret physically.

ditions at the origin:

$$\begin{aligned}
i\gamma^5\gamma^3\tilde{\psi}_{\mathbf{K},s}^{(+)}(X)\Big|_{n_3=0} &= e^{i(K_1X_1+K_2X_2)} \left(i\gamma^5\gamma^3e^{i\frac{1}{2}K_3\Delta x_3}U_{\mathbf{K},s} + e^{-i\frac{1}{2}K_3\Delta x_3}U_{\mathbf{K},s} \right) \\
&= \tilde{\psi}_{\mathbf{K},s}^{(+)}(X)\Big|_{n_3=-1}, \\
i\gamma^5\gamma^3\tilde{\psi}_{\mathbf{K},s}^{(-)}(X)\Big|_{n_3=0} &= e^{-i(K_1X_1+K_2X_2)} \left(i\gamma^5\gamma^3e^{-i\frac{1}{2}K_3\Delta x_3}V_{\mathbf{K},s} + e^{i\frac{1}{2}K_3\Delta x_3}V_{\mathbf{K},s} \right) \\
&= \tilde{\psi}_{\mathbf{K},s}^{(-)}(X)\Big|_{n_3=-1}.
\end{aligned}$$

Substituting either mode combination into the Neumann condition at the upper z -boundary in both cases consistently implies

$$K_3 = \frac{\pi}{L_3} \left(n_3 + \frac{1}{2} \right), \quad (5.78)$$

where n_3 is the site-index in the z -direction of the discrete mode-space.

These linear combinations with the constraints on the wave-vectors and coordinate in the z -direction thus provide the vacuum field-configurations satisfying also the Neumann boundary conditions imposed on the z -axis.

Asserting that the x and y -coordinate relates to the respective, lattice-site index n_i through

$$X_i = n_i\Delta x_i,$$

equivalently to the periodic case – only instead substituting the linear combinations into the boundary conditions – determines

$$K_i = \frac{2\pi}{L_i} \left(e_i + \frac{1}{2} \right), \quad (5.79)$$

where e_i is the site index in the corresponding direction of the discrete mode-space.

These constraints on the lattice wave-vectors in the x - and y -direction thus ensure that the constructed, linear vacuum-solutions satisfy the boundary con-

ditions imposed in the x and y directions. This result further effectively incorporates the x - and y -boundary choices into the dynamics although the ansatz notably eliminates any explicit x - or y - spatial gradient terms that would require directly implementing the periodicity conditions.

The constructed linear-combinations with the determined form of the mode- and the lattice-space coordinates thus ultimately provide the vacuum mode functions comprehensively satisfying the boundary-conditions on the lattice. This choice of the initial condition further specifies the mode-variable Λ notably to be K_3 for the initialization.

Implementing the transformation $K_i \rightarrow -K_i$ on the negative energy solution further yields the initial mode function

$$\tilde{\psi}_{\mathbf{K},s}^{(-)}(X) = e^{i(K_1 X_1 + K_2 X_2)} \left(e^{iK_3 X_3} V_{-\mathbf{K},s} + i\gamma^5 \gamma^3 e^{-iK_3 X_3} V_{-\mathbf{K},s} \right).$$

Thus, the x and y dependency becomes identical to the positive energy solution. Matching these configurations to the simplified ansatz expression (5.54) hence readily determines the constructed initial conditions satisfy the ansatz expression and yields

$$\begin{aligned} \chi_{(K_1, K_2, \Lambda, s)}^{(U)}(0, X_3) &= e^{iK_3 X_3} U_{\mathbf{K},s} + i\gamma^5 \gamma^3 e^{-iK_3 X_3} U_{\mathbf{K},s}, \\ \chi_{(K_1, K_2, \Lambda, s)}^{(V)}(0, X_3) &= e^{iK_3 X_3} V_{-\mathbf{K},s} + i\gamma^5 \gamma^3 e^{-iK_3 X_3} V_{-\mathbf{K},s}, \end{aligned} \quad (5.80)$$

with also the recognition $\Lambda = K_3$ in this initial configuration.

Consistency with the Canonical Quantization

To validate these vacuum solutions for the Neumann boundaries requires confirming their consistency with the standard, anti-commutator relations imposed on quantization.

The canonical commutator (5.39), in particular, at the initial time imposes

$$\left\{ \hat{\Psi}_a(0, \mathbf{X}), \hat{\Psi}_b^\dagger(0, \mathbf{Y}) \right\} = \hbar c \frac{\delta_{\mathbf{X}\mathbf{Y}}^3}{\Delta x_1 \Delta x_2 \Delta x_3} \delta_{ab},$$

This therefore requires the mode expansion of the fermion operator (5.53) with the standard (time-independent) commutator relations for the ladder operators (5.43) together reproduce this field commutator for the choice of initial modes.

Asserting the ladder-operator relations to be valid at the initial time, and substituting the constructed vacuum-solutions (5.80) into the mode expansion (5.53) – with the identification that initially $\Lambda = K_3$ (though importantly, the weighting $\Delta\lambda/(2\pi)$ of the integral remains to be determined subsequently) – yields:

$$\begin{aligned} \left\{ \hat{\Psi}_a(0, \mathbf{X}), \hat{\Psi}_b^\dagger(0, \mathbf{Y}) \right\} &= \hbar c \sum_{K_1, K_2, K_3} \frac{\Delta k_1}{(2\pi)} \frac{\Delta k_2}{(2\pi)} \frac{\Delta\lambda}{(2\pi)} e^{iK_1(X_1-Y_1)} e^{K_2(X_2-Y_2)} \\ &\left(\left(e^{iK_3(X_3-Y_3)} + e^{-iK_3(X_3-Y_3)} \right) \sum_s \left((U_{\mathbf{K},s})_a (U_{\mathbf{K},s}^\dagger)_b + (V_{-\mathbf{K},s})_a (V_{-\mathbf{K},s}^\dagger)_b \right) \right. \\ &+ \sum_{c,d} e^{-iK_3(X_3+Y_3)} i (\gamma^5)_{ac} (\gamma^3)_{cd} \sum_s \left((U_{\mathbf{K},s})_d (U_{\mathbf{K},s}^\dagger)_b + (V_{-\mathbf{K},s})_d (V_{-\mathbf{K},s}^\dagger)_b \right) \\ &\left. + \sum_{c,d} e^{iK_3(X_3+Y_3)} i (\gamma^5)_{dc} (\gamma^3)_{cb} \sum_s \left((U_{\mathbf{K},s})_a (U_{\mathbf{K},s}^\dagger)_d + (V_{-\mathbf{K},s})_a (V_{-\mathbf{K},s}^\dagger)_d \right) \right). \end{aligned}$$

The conventional positive and negative-energy solutions further satisfy the standard result

$$\begin{aligned} \sum_s U_{\mathbf{K},s} U_{\mathbf{K},s}^\dagger &= \frac{i}{2\omega_{\mathbf{K}}} \left(\left(\frac{mc}{\hbar} \right) \mathbb{I}_4 - i\gamma^0 \omega_{\mathbf{K}} - i \sum_i \gamma^i K_i \right) \gamma^0, \\ \sum_s V_{\mathbf{K},s} V_{\mathbf{K},s}^\dagger &= \frac{i}{2\omega_{\mathbf{K}}} \left(- \left(\frac{mc}{\hbar} \right) \mathbb{I}_4 - i\gamma^0 \omega_{\mathbf{K}} - i \sum_i \gamma^i K_i \right) \gamma^0; \end{aligned}$$

and this in the initial condition readily determines

$$\begin{aligned} \left\{ \hat{\Psi}_a(0, \mathbf{X}), \hat{\Psi}_b^\dagger(0, \mathbf{Y}) \right\} = & \\ \hbar c \sum_{K_1, K_2, \Lambda} \frac{\Delta k_1}{(2\pi)} \frac{\Delta k_2}{(2\pi)} \frac{\Delta \lambda}{(2\pi)} e^{iK_1(X_1 - Y_1)} e^{K_2(X_2 - Y_2)} & \\ \left(\cos(K_3[X_3 - Y_3]) (\mathbb{I}_4)_{ab} + \cos(K_3[X_3 + Y_3]) \sum_c i(\gamma^5)_{ac} (\gamma^3)_{cb} \right) & \end{aligned} \quad (5.81)$$

Considering the form of the spatial coordinates (5.77) satisfying the boundary conditions determines

$$X_3 + Y_3 = (n_3 + n_3 + 1)\Delta x_3.$$

This is non-zero everywhere on the lattice, and hence, the second term in the correlator expansion (5.81) involves a summation in the k_3 direction over anti-symmetric, cosine values: entirely cancelling pairwise for even N_3 , to zero at any pair of z -coordinates.

The spatial-coordinate structure (5.77) similarly implies

$$X_3 - Y_3 = (n_3 - m_3)\Delta x_3.$$

This is non-zero over the lattice except at $X_3 = Y_3$; and for $X_3 \neq Y_3$, the summation in the z -mode direction again equals zero for even N_3 , through the pairwise cancellations of the summed cosine-values. At $X_3 = Y_3$ though, the cosine term equals unity; and equally the summation over the x - and y -mode directions vanish everywhere except where $X_1 = Y_1$ and $X_2 = Y_2$. The first term in the correlator expansion therefore yields

$$\left\{ \hat{\Psi}_a(0, \mathbf{X}), \hat{\Psi}_b^\dagger(0, \mathbf{Y}) \right\} = N_1 N_2 N_3 \hbar c \frac{\Delta k_1}{(2\pi)} \frac{\Delta k_2}{(2\pi)} \frac{\Delta \lambda}{\pi} \delta_{\mathbf{X}\mathbf{Y}}^3 \delta_{ab}.$$

This result notably involves the undetermined summation weighting $\Delta\lambda/2\pi$. The initial relation $\lambda = k_3$ indicates the weighting relates to Δk_3 ; choosing the weighting in particular to satisfy

$$\frac{\Delta\lambda}{\pi} = \frac{\Delta k_3}{\pi} = \frac{K_3|_{e_3+1} - K_3|_{e_3}}{\pi},$$

thus, explicitly specifies this constant through the lattice wave-vectors. Substituting the expressions (5.79) and (5.78) for the wave-vectors into the initial correlator therefore yields

$$\left\{ \hat{\Psi}_a(0, \mathbf{X}), \hat{\Psi}_b^\dagger(0, \mathbf{Y}) \right\} = \hbar c \frac{\delta_{\mathbf{X}\mathbf{Y}}^3}{\Delta x_1 \Delta x_2 \Delta x_3} \delta_{ab}.$$

This precisely forms the canonical-quantization requirements on the fermionic anti-commutators for the fermionic initial conditions satisfying the Neumann boundaries, notably through the implementation of the standard, ladder-operator relations. These derived, vacuum mode functions thus provide an initial condition entirely consistent with the canonical quantization of the discrete system. The time independence of the ladder operators determine their initial commutation relation remains valid at all times; and equivalently, the conservation standardly of the field commutator ensures that the implementation of the canonical-quantization relation at the initial time remains throughout the evolution. This choice of initial modes in the Neumann system hence ensures the required, canonical-quantization conditions remain valid for all time.

The initial consistency results, further, through the particular weighting of λ in the summation²¹. This consistency thus validates the chosen value of the

²¹This form of the summation weighting $\Delta\lambda/(2\pi)$ creating the canonical, field-quantization commutator significantly results for the particular choice of the initial modes, the ladder-operators and the expansion summation. The ansatz specifies the initial form of the fermions fields only up to an arbitrary factor; while the field commutator places the only further constraint on these modes and the additional components forming the mode expansion. This therefore enables a considerable freedom in specifying the quantities multiplying either the mode functions, the ladder operators, the sum weightings or additional factors within the expansion: redefining the particular factors in any component with a redefinition within the

summation weighting initially; the time independence of the weighting further ensures this expression throughout the evolution (although the relevant variable in the summation may no longer be K_3) specifies the relevant weighting.

5.6.2 Gauge Field, External Current and Higgs Phase

Consistency with the vacuum initial conditions for the fermions requires no initial magnetic or electric field; this hence implies that the initial gauge fields likewise are trivially zero everywhere. The electromagnetic fields required in the dynamics for the initialization thus satisfy

$$E_i(0, \mathbf{X}) = 0,$$

$$A_\mu(0, \mathbf{X}) = 0.$$

Creating the consistency with the vacuum initial configuration further determines the external current is uniformly zero. This with the absence of the electromagnetic fields, and setting both the fermion and the Wilson current effectively to zero through the vacuum mode-configuration, on substitution into the gauge dynamics implies that the initial Higgs charge and current vanish everywhere. These conditions may most simply be accomplished through setting the phase uniformly to zero at the initial time:

$$\theta(0, \mathbf{X}) = 0.$$

This configuration with the vacuum modes and the absence of the electromagnetic fields, thus, trivially satisfy the electric field dynamics at the initial time; and notably in particular, the discretized Gauss'-law constraint, specifying charge conservation on the lattice.

further quantities might equally produce the required result. Thus in general, the asserted initial modes and the ladder, anti-commutator relations through the particular form of the field expansion determine the specific summation weighting of Λ .

The ensemble variances of the infinite, Gaussian distributions may precisely reproduce the fermionic correlator, and hence, these initial conditions for the fields may likewise trivially satisfy the Gauss'-law constraint in the ensemble method. In practice though, the variation in the ensemble-averages of the finite sample selected may prevent the trivial initial conditions satisfying the Gauss'-law constraint. This deviation, in particular, determines the fermions contribute a finite change in the Gauss'-law constraint. Satisfying this condition, even in the case of a zero external current and Higgs field, hence involves a finite, initial electric field.

Defining the discrete Fourier transform on the lattice through

$$f(X) \equiv \sum_j \sum_{e_j} \exp\left(-2\pi i \frac{e_j n_j}{N_j}\right) \tilde{f}(K)$$

and implementing this transformation on the Gauss'-law constraint (5.40a) implies

$$\sum_j i\tilde{K}_j \tilde{E}_j(K) = \tilde{\rho}(K),$$

with also

$$\tilde{K}_j \equiv \frac{i}{\Delta x_j} \left(1 - \exp\left(2\pi i \frac{e_j n_j}{N_j}\right)\right),$$

and where the term sourcing the electric field is derived through acting the Fourier transform on the discretized charge-densities:

$$\rho(X) \equiv \frac{q}{\hbar} \text{Im}\{\langle T \hat{\Psi}(X) \gamma^0 \hat{\Psi}(X+0) \rangle\} - \frac{1}{\Delta x_0} \frac{e}{\hbar} \rho^2(X) \text{Im}\{\Theta^\dagger(X) \Theta(X+0)\} + j_0(X).$$

Asserting that the electric field satisfies

$$E_j \propto \tilde{K}_j$$

consequently yields

$$\tilde{E}_j(K) = \frac{i\tilde{\rho}(K)}{\sum_i \tilde{K}_i^2} \tilde{K}_j, \quad (5.82)$$

specifying the electric field in Fourier space. The inverse Fourier transform hence provides the initial electric field satisfying also the non-trivial, Gauss'-law constraint in practice for the ensemble case.

5.7 Generating the Uniform Magnetic-Field

To examine tunnelling of a magnetic field through the superconducting barrier involves forming a static magnetic field outside the region enclosed by the barrier. The external current may produce this magnetic field; while the initial vacuum-state requires evolving the fields to the final, static state.

5.7.1 External Current Configuration

Imposing, in particular, the only non-zero component of the external current

$$j_1(X) = \Theta(T) \left(|J| \exp\left(-\frac{(X_3 - z_1)^2}{2\sigma^2}\right) - |J| \exp\left(-\frac{(X_3 - z_2)^2}{2\sigma^2}\right) \right), \quad (5.83)$$

with $z_1 < z_2$ and $\sigma \ll z_2 - z_1$ provides a smooth distribution generating an approximately uniform magnetic field in the z -direction, away from the Gaussian peaks in the current; while the time-dependent coefficient may gradually increase the external current from the vacuum initial state to the static, final state. (This configuration notably both satisfies the constraint on the current for the ansatz, and likewise provides an equivalent expression suitable to use in the full 3 + 1D case.)

The Gaussian terms effectively each form a sheet of current localised around z_i with the width equal to σ . Any sheet of constant current without additional modification generates a uniform magnetic field in the region external to the current; the current, the normal from the sheet to the point in the field and

the magnetic force in this configuration form a right-handed set. The Gaussian centred at z_1 , hence, in the final, static state generates a uniform magnetic field, orientated in the positive y -direction at $X_3 > z_1 + \sigma$; while the negative current centred at z_2 , likewise, produces a magnetic field at $X_3 < z_2 - \sigma$. These two fields therefore, in the absence of any barrier or the fermionic fields, mutually reinforce in the region $z_1 + \sigma < X_3 < z_2 - \sigma$ to generate a uniform field in the static state. The Gaussian centred at z_1 further may generate a uniform magnetic field at $X_3 < z_1 - \sigma$ except orientated in the negative direction and likewise the current centred at z_2 . On periodic boundaries, these generated fields may mutually reinforce: thus in the static, final state, without fermions or any barrier, the two combine to form a uniform field in the region $X_3 < z_1 - \sigma, X_3 > z_2 + \sigma$ aligned though oppositely to in the region $z_1 + \sigma < X_3 < z_2 - \sigma$.

The form of the magnetic fields demonstrates the reflectional symmetry around the centre of the z -axis. Positioning the super-conducting enclosure centrally on this axis will retain the symmetry, and hence ensure the currents generate the magnetic field symmetrically in the two regions outside the barrier. The symmetry in the location of the currents and the barriers remains also on the inclusion of the fermions. This therefore implies both the magnetic field and the fermion field will incorporate the symmetry around the centre of the z -axis. Observing this symmetry, in both the quantum and classical case, may therefore confirm the validity of the simulation.

Setting the time variation to

$$\Theta(T) = \frac{1}{2} \tanh(\theta) + \frac{1}{2}, \quad \theta = \tan\left(\frac{\pi T}{\tau} - \frac{\pi}{2}\right) \quad (5.84)$$

enables a smooth initial transition from zero and rapid stabilization after the time τ to produce the fixed, final state for investigation.

5.7.2 Siting the External Current on the Lattice

Centring the oppositely-aligned currents respectively on the z -boundaries in the Neumann case provides a distinct and definite location for the current peaks, while the independence of the boundaries excludes any inherent inconsistency in the configuration. This choice also importantly maximises the region of the magnetic field on the lattice external to the current and the superconducting barrier.

The fermionic terms contributing to the current notably define the location of the currents within the discrete system: thus, in particular, defining the boundary position of the external current. These fermionic contributions on the lattice involve the field value at adjacent sites; the fermion (and Wilson) current associated to the site of index n_3 in the z -direction hence occurs physically at $X_3|_{n_3} + X_3|_{n_3-1} = (n_3 - 1/2)\Delta x_3$: offset, midway between the discretization interval. This – with the boundaries defined respectively at $n_3 = -1$ and $n_3 = N-1$ – therefore determines $z_1 = -\Delta x_3/2$ and $z_2 = (N_3 - 1/2)\Delta x_3$.

In the periodic case, the relation between the boundaries prevents positioning the oppositely aligned currents on the boundaries without inconsistency. The current peaks, though, may likewise be positioned midway between the discretization interval to match their position in the Neumann case; this notably enables producing a region in the periodic case equivalent to the Neumann system for direct comparison. Choosing the distance $z_1 < X_3 < z_2$ equal to the combined length of the regions $z_2 < X_3$ and $X_3 < z_1$ may define the location of the peaks. This, in particular, may be obtained through setting $z_1 = (N_3/4 - 1/2)\Delta x_3$ and $z_2 = (3N_3/4 - 1/2)\Delta x_3$. These coordinates thus, define the explicit configuration of the current, for use in the periodic case.

5.7.3 Dissipating Generated Waves

The varying external current in the smooth increase to the static, final state inherently generates electromagnetic waves. These disrupt the uniform magnetic field usefully generated and further may excite similar oscillations in the fermion and Wilson current. (Increasing the transition time to the final state may decrease the amplitude of the generated waves but the system still includes waves and the longer time impairs the computational efficiency.) Enabling the energy in the waves to dissipate from system provides an efficient method to prevent the disruption of these oscillations in the final, static configuration. Adding a dissipative term proportional to the time derivative of the gauge field provides a simple method for accomplishing this decay without disrupting the static magnetic field. The dissipative term, specifically, in the classical dynamics may comprise simply

$$-\frac{\zeta}{\mu_0}\partial_0 A_i(x),$$

with ζ a constant and > 0 added onto the non-zero terms (on the left-hand side) in the quantized, electric field dynamics (5.9b). This notably reduces to zero when the gauge field is constant, and therefore contributes nothing to the ideally static, final state of the system; the term, also, acts to oppose any change in the gauge field and, thus, generates the required dissipative effect while the electromagnetic fields evolve to the final state.

Applying the definition of the continuum electric field (5.6) to the dissipative term yields

$$-\frac{\zeta}{\mu_0}\partial_0 A_i(x) = \frac{\zeta}{\mu_0 c} E_i(x).$$

This expression in terms of the electric field forms the basis to hence readily obtain the equivalent dissipative term on the lattice:

$$\frac{\zeta}{\mu_0 c} E_i(X),$$

where the discrete electric field (5.36) implicitly involves a discretized equivalent of the gauge-field derivative, defined through the gauge links. This addition into the non-zero terms (on the left-hand side) in the quantized, electric field dynamics (5.40b) on the lattice, hence equivalently to the continuum, generates the required dissipation without altering the ideally static, final state.

The dissipative term correspondingly modifies the iteration relations for the electric field evolution; and notably under the ansatz, this modification reduces to purely the addition of the $E_i(X)$ contribution. These additions thus form the practical mechanism to obtain the static, final state of the system.

Chapter 6

Tunnelling of the 3rd Kind: Simulations

6.1 Parameter Choices for Numerical Simulations

Throughout the simulations, natural units of $\hbar = c = 1$ are imposed for simplicity. The fermion mass m and the Higgs charge e respectively defining the units of mass and of charge corresponds to these parameters equalling unity in the dynamics. Setting the gauge-fermion coupling to $q = 0.3$ provides a fermion-gauge coupling smaller than the Higgs-charge e , while sufficiently large to compute numerically. Choosing also $r_W = 0.5$ accomplishes the effective prevention of spatial-doublers in the simulation.

6.2 Numerical Code

Converting the iteration relations for the fields in the ensemble case (see Section 5.4.6) and in the ansatz case (see Section 5.4.8) for the fields into a C code provided the basis for evolving the system. The simulations without the fermions involved sufficiently few field values to compute, conveniently, using only a serial code. Employing the Open MPI libraries enabled parallelizing the evolution to compute the substantially increased number of field values, on incorporating the fermions. Constructing the current (5.83) configuration and the static, super-

conducting barrier (5.4) involves simply evaluating these functions on the relevant lattice sites, using the standard library of C maths operations.

The ensemble code with the periodic boundaries computes the field evolution equivalently to the ensemble method in the bosonic system (see Section 3.2). This procedure, in the tunnelling case, divides the fermion ensemble onto the processors, with the gauge field and Higgs phase also computed on each processor to evolve the ensemble; the MPI-sum algorithm again yields the ensemble variances throughout the dynamics. The initialization of the fermions, also, is accomplished equivalently to the boson ensemble (see Section 3.2). This process, though, for the fermions notably instead uses the (updated) FFTW3 algorithms to efficiently compute the Fourier transforms. The random numbers, further, are employed to generate both the male and female fields, and the effective independence of these random coefficients further, ensures the variances vanish except for identical spin-states and spinor components, in addition to identical wave-vectors. Computing the non-zero Electric field components in the ensemble case also involves a Fourier transform, again, efficiently accomplished using the FFTW routines. Simply setting the initial Higgs-phase and gauge field to zero in the code completes the initialization.

Implementing the ansatz case, on both periodic and Neumann boundaries, involved an equivalent procedure to the ensemble case, though each processor, rather than computing a portion of the ensemble, instead evolves a portion of the fermion modes. The processors, in particular, compute, the modes for every coordinate in the z -direction of the wave-vector space but only a section of the x and y directions, along the entire, real-space z -axis on the lattice. Constructing the initial fermion fields importantly only involves computing the vacuum modes without the need for a Fourier transform; the electric field involves also simply the initial value to zero, without the FFTW3 routine needed to compute the field. This notably, thus, entirely alleviates the need for the (computationally demanding) FFTW3 routines on applying the ansatz.

6.3 Computational Efficiency

6.3.1 Lattice-Site Quantity: Mode Functions

Completing the numerical analysis on an array of N_i sites in each spatial dimension entails the electric vector and spatial gauge-components – the time component set to zero in the temporal gauge – with the Higgs phase evaluated on $N_1N_2N_3$ sites: comprising in total $6N_1N_2N_3$ values. The discrete mode space correspondingly forms an equally sized lattice; and evaluating the correlator-expansion entails the summation over this mode space at each site on the spatial lattice, with each mode-value including both spin states, each themselves a four-component spinor: a total of $8(N_1N_2N_3)^2$ values. This evolution through the mode function method, therefore, in total, requires evolving $6N_1N_2N_3 + 8(N_1N_2N_3)^2$; and thus – notably through the quantized, fermion fields – depends quadratically on the lattice dimensions.

6.3.2 Lattice-Site Quantity: Ensemble Method

The ensemble-method evolution computes the electric field, gauge-components and Higgs phase identically to the mode function case except altering the method to compute the correlators. This therefore entails an equal number of these field-values: in total, $6N_1N_2N_3$.

Obtaining each ensemble correlator at a site on the lattice involves the average over the N_E ensemble fields for the four-components of each ensemble field: $4N_EN_1N_2N_3$ values in total. The ensemble size – precisely reproducing the quantum correlators – in principle is infinite; the finite sample of N_E fields in practice though is sufficient for numerical convergence of the evolution¹.

¹The ensemble-variance in the finite case differs from the quantum variance in particular at the initial time. An analytic expression of the initial correlators further may be obtained on the choice of the modes initializing equally the ensemble and the quantum fields. This therefore enables quantifying the discrepancy between the cases; and thus may as in the Bosonic case provide a measure of the precision of the finite ensemble in reproducing the quantum result.

This evolution through the ensemble method therefore in total requires evolving $6N_1N_2N_3 + 4N_EN_1N_2N_3$; and hence if $N_E < 2N_1N_2N_3$ at the convergence in the ensemble size, the technique reduces the number of computed field values scales slower than the quadratic variation in the mode function case.

6.3.3 Lattice-Site Quantity: Ansatz Case

The ansatz method entails the electric vector and spatial gauge-components with Higgs phase evolved on the N_3 lattice sites in purely the z -direction: these $6N_3$ values, in total, significantly fewer than the number evolved in the previous $3 + 1\text{D}$ -cases.

Obtaining the correlator involves the summation over the discrete mode-space at each real-space site. The mode-space in each direction comprises a site number equal to the respective quantity in real-space direction. Hence, the z -direction in the mode space incorporates N_3 sites.

The site number in the transverse mode space remains unconstrained directly by the existence of any real-space sites – in contrast to the $3 + 1\text{D}$ mode function case. Both the real-space length and the lattice sites in these directions though remain relevant quantities in the mode space through the discrete wave-vectors on the lattice (Section 5.6.1).

Specifying the real-space lengths and requiring convergence in the lattice spacing may determine these parameters on the real-space lattice: and hence in particular defines the lattice-site quantity in the real-space, x and y -directions. This procedure thus indirectly yields the number of real-space sites in the transverse directions and hence the equality of the sites in the real and the mode space determines the number of sites in the respective directions of the mode space.

The correlator summation over the mode space of N_i sites in the i th direction while including both spin states (each a four-component spinor) involves in total $8N_1N_2N_3^2$ values. This ansatz method therefore in total requires the computation of $6N_3 + 8N_1N_2N_3^2$. The greatest reduction in the computational

requirements compared to the mode function simulations thus occurs through this total depending quadratically only on the z -direction rather than the entire three-dimensional space. These ansatz dynamics in contrast to the ensemble system provide a significant reduction in the computational requirements when $N_1 N_1 N_3^2$, in the ansatz case, is much less than $N_1 N_2 N_3 N_E$, in the ensemble case; this may notably result if $N_E \sim N_1 N_2 N_3$, while both cases involve a similar site quantity in each direction.

6.3.4 Measured Computational-Efficiencies

Implementing the ensemble method on a lattice of length $L_x = L_y = 9.6$ and $L_z = 18$ for $\Delta x_1 = \Delta x_2 = \Delta x_3 = 0.3$ and with the periodic boundaries provides a trial to evaluate the procedure.

Setting the external current amplitude to $|J| = 0.5$ (and located at the sites equivalent to the Neumann case, see Section 5.7.2) sourced a magnetic field density of $\mathcal{O}(1)$. The width set to $\sigma = 0.8/\sqrt{2}$ sufficiently smoothed the current to prevent numerical difficulties, while still remaining comparatively localized in the volume. Choosing $\tau = 80$ in increasing the current from zero to the final state, further, provided a practicably brief transition time. Preliminary simulations without fermions confirmed this choice, with the damping coefficient set to $2\pi/9$, generated negligible transient disruptions in the final state.

Choosing further $\Delta x_0 = 0.002$ set the time-step necessarily smaller than the lattice spacing; and the preliminary numerical tests without fermions indicated this yielded sufficient convergence in the magnetic field.

The trial lattice comprises $N_1 \times N_2 \times N_3 = 61440$ sites – notably, also the total number of fermion modes in the lattice system. A comparatively small ensemble of 1536 fields, equal to two and a half per cent of the mode number forms the case for assessment.

This trial configuration omits the Higgs field, for simplicity. The evolution without fermions therefore generates a uniform magnetic field between the cur-

rents centred at $z_1 = (N_3/4 - 1/2)\Delta x_3$ and $z_2 = (3N_3/4 - 1/2)\Delta x_3$, with the field oppositely aligned in the regions either side (in the effectively contiguous space crossing the periodic boundary) – the figure 6.5 illustrates the generic form.

Incorporating the fermions through the ensemble method produces a magnetic field of the typical form illustrated in the figure 6.1 (top, left). This shows the field sufficiently long after the external current has ceased increasing for the magnetic field in the case without fermions to have settled to a steady value. The field with the fermions, though, continues fluctuating throughout the simulation. These continuous variations thus prevent a non-uniform field forming between the current peaks even when the current is static. The figure 6.1 (top, left) illustrates the typically significant deviations.

This persistent fluctuation indicates simply an insufficient ensemble size was applied in the simulation. The initial statistical variation in the ensemble current across the lattice for the finite ensemble inherently sources an inhomogeneous evolution contrasting the true, zero vacuum-current. These deviations for a sufficiently small ensemble may form substantial deviations, amplified through the subsequent evolution averaging over the insufficient ensemble size. The figure 6.1 illustrates the irregular spatial-variation typical in the x - y - and z -components (respectively top, right; bottom, left; bottom, right) of the ensemble current. These variations also fluctuate throughout the simulation. This consequently confirms the inadequate size of the ensemble.

The symmetry in the system, notably, yielding the constraint equation (5.64) determines the system excludes any fermion or Wilson current (within the bulk, outside the external current) in respectively the y - and z -directions. The current measured in these directions for the ensemble, hence, may only result through the inaccuracies in the method approximating to the true quantum correlators. These measured, erroneous currents, thus, indicate the approximate error for the chosen ensemble-size. The figure 6.1, in particular, illustrates the ensemble of 1535 fields produces an $\epsilon \sim \mathcal{O}(10^{-4})$ error in the average current-density across

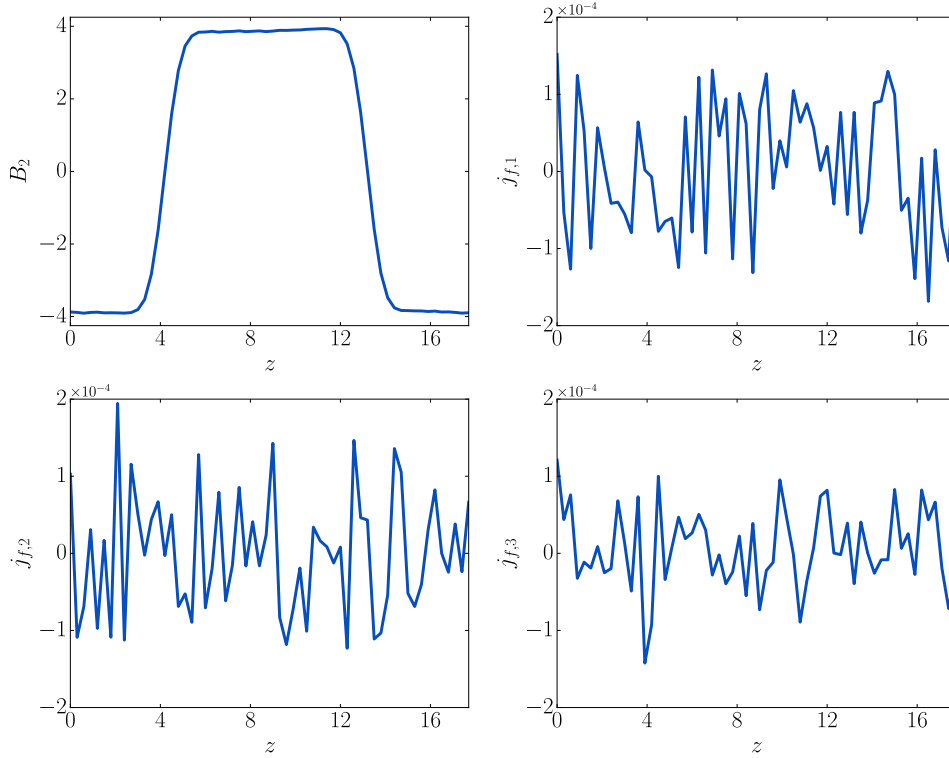


Figure 6.1: A trial simulation using the ensemble method for an ensemble of 1536 fields, without the superconducting barrier and on periodic boundaries in each direction. The trial was completed for the lattice of length $L_x = L_y = 9.6$ and $L_z = 18$, with $\Delta x_1 = \Delta x_2 = \Delta x_3 = 0.3$. These figures show $t = 100$ when the external current is constant, having increased to the final value in time $\tau = 80$. Each field is averaged over the x - y plane, at every lattice site in the z -direction. These results illustrate the typically large fluctuations in the combined fermion- and Wilson-current (top-right and bottom) because of the inadequate ensemble size. The combined fermion- and Wilson-current at a site X on the lattice notably involves an asymmetric combination of the fermion field (see Section 5.1.1, and also the equation (5.40b)); and the electric field dynamics (5.40b). This determines that despite the periodic boundary conditions, the combined fermion- and Wilson-current at the boundaries in each direction may form the

considerably asymmetric configuration shown. The magnetic field (top, left) illustrates the resultant disruption to the uniformity of this field between the peaks of the current at $z_1 = 4.35$ and $z_2 = 13.35$, generated by the large fluctuations in the combined fermion- and Wilson-current.

the x - y plane. This notably matches the typical amplitude of the current in the x -direction, also illustrated in the figure. The statistical error, thus, dominates the expectedly physical fermionic current. This computed current in the x -direction further sources the x -component of the electric field (through the equation (5.40b)); and hence, the statistical errors in the ensemble current disrupt the magnetic field. The irregularities in the field thus correspond precisely to the inadequate approximation of the ensemble to the exact fermion and Wilson current.

A larger ensemble-size would ameliorate the difficulties observed in the trial case. This simulation though already required over 156 hours (real-time) to complete on 256 processors. A significant increase in the ensemble size – the lattice sites scaling according to $4N_E N_1 N_2 N_3$ – would entail further processors and protract the simulation. These both in computational resources and the time involved to examine varying parameters constitute a highly impractical option.

The ansatz case for an equal volume and equal discretization intervals to a (longer) simulation time of $t = 150$ involve again 256 processors but reliably complete in less than an hour. These thus offer a substantially more practical option to evaluate; and accordingly will form the method employed in the ensuing tunnelling simulations.

6.4 Renormalization

6.4.1 Numerical Renormalization Procedure

Renormalization essentially implies that the potentially observable quantities in the quantum system prior to implementation of the procedure include an unphysical component. This component occurs through the correlator mode-expansion involving a non-convergent integrand. In the continuum, the integration of this integrand over all modes produces an infinite result. The restriction to a finite number of modes on the lattice ensures a finite result. Reducing the lattice spacing on a fixed physical length, though, increases the number of modes in the summation and, hence, the non-convergence of the additional contributions causes the summation to diverge. Any physical observable may reasonably be assumed to remain independent of the lattice parameters. This, hence, implies the divergence on the reduction of the lattice spacing results entirely through the unphysical contribution to the correlators. (In practice, the physical variables converge to a constant value, rather than remaining strictly invariant, on reducing the lattice spacing. The convergence of the results to a sufficient degree, though, may ensure the physical values remain constant to an arbitrarily high accuracy on changing the spacing. This hence enables distinguishing any much larger, unphysical contributions.) The correlator, prior to any renormalization, thus includes both this physical component, invariant on the reduction in lattice spacing, and the unphysical contribution dependent on the lattice spacing. This in particular implies that the combined fermion- and Wilson-current on the lattice, without renormalization, likewise involves both these contributions:

$$\begin{aligned}
 j_f(X, \Delta \mathbf{x}) &\equiv \left(\frac{q}{\hbar} \text{Im} \left\{ \langle \hat{\Psi}(X) \gamma^1 U_1(T, X_3) \hat{\Psi}(X+1) \rangle \right\} \right. \\
 &\quad \left. - \frac{q}{\hbar} r_w \text{Im} \left\{ \langle \hat{\Psi}(X) U_1(T, X_3) \hat{\Psi}(X+1) \rangle \right\} \right) \Big|_{\Delta \mathbf{x}} \\
 &= j_{\text{phys}}(X) + j_{\text{div}}(X, \Delta \mathbf{x}).
 \end{aligned}$$

Obtaining the renormalized dynamics hence effectively entails subtracting the spacing-dependent contribution in the fermion current.

The invariance of the physical component at differing lattice spacing implies:

$$j_{\text{div}}(X, \Delta \mathbf{x}) = j_f(X, \Delta \mathbf{x}) - j_f(X, \Delta \mathbf{x}_{\text{ref}}) + j_{\text{div}}(X, \Delta \mathbf{x}_{\text{ref}});$$

thus expressing the renormalizable contribution at any lattice spacing through the fermionic current at the selected reference-spacing. Further, the field renormalization in principle results through adding contributions in the action constructed through a coordinate-independent variable multiplying the existing terms; and these factors accordingly modifying the corresponding components in the dynamics. These additional terms may reasonably be derived from the multiplying of the plaquette terms – defining the discrete equivalent to the electromagnetic field tensor – in the action (5.32) on the lattice:

$$\frac{1}{c} \Delta V \left[\alpha_E \sum_i \frac{\hbar^2}{2q\mu_0(\Delta x_i)^2(\Delta x_0)^2} (2 - U_{i0}(X) - U_{0i}(X)) \right. \\ \left. - \alpha_B \sum_{ij} \frac{\hbar^2}{4q^2\mu_0(\Delta x_i)^2(\Delta x_j)^2} (2 - U_{ij}(X) - U_{ji}(X)) \right].$$

The first summation, on varying the action and applying the ansatz, corresponds to additional terms (on the non-zero side) in the electric field dynamics (5.58), identical to the existing electric field contribution except with the renormalization coefficient α_E multiplying the field:

$$\alpha_E \frac{1}{\Delta x_0} \frac{1}{\mu_0 c} (E_1(T, X_3) - E_1(T - 0, X_3)).$$

Likewise, the second summation yields additional terms in the electric field dynamics, identical to the existing plaquette terms – corresponding to the magnetic field in the continuum limit – except with the renormalization coefficient α_B mul-

tipling each term²:

$$\alpha_B \frac{1}{\Delta x_1 (\Delta x_3)^2} \frac{\hbar}{q\mu_0} \text{Im} \{U_{13}(T, X_3) - U_{31}(T, X_3 - 3)\}.$$

An identical renormalization coefficient may be chosen, for simplicity, in both the additional contributions to the action: $\alpha_E \equiv \alpha_B \equiv \alpha$. This single factor α may specify the renormalization factor multiplying both the electric and plaquette term³.

For the renormalization terms to cancel the divergent contribution to the current in the electric field dynamics, hence, implies these opposing components relate through

$$j_{\text{div}}(X, \Delta \mathbf{x}) = \alpha \left(\frac{1}{\Delta x_0} \frac{1}{\mu_0 c} (E_1(T, X_3) - E_1(T - 0, X_3)) + \frac{1}{\Delta x_1 (\Delta x_3)^2} \frac{\hbar}{q\mu_0} \text{Im} \{U_{13}(T, X_3) - U_{31}(T, X_3 - 3)\} \right). \quad (6.1)$$

This expression for the divergent contribution, further, involves purely fixed parameters, the discretized electromagnetic fields and the renormalization coefficient. The requirement for physical observables to essentially remain independent of lattice spacing, further, applies to the discrete electric field and plaquette terms inside the bracket, respectively corresponding to the time derivative of the electric field and of the spatial derivative of the magnetic field. Any lattice spacing dependency in the renormalization current therefore occurs within the renormalization coefficient; and the coordinate independence of the coefficient determines the spatial variation of the renormalization piece occurs entirely in

²These additions to the action notably also will contribute to the Gauss'-law constraint on the lattice (5.55); consideration of this is not necessary to obtain the correct dynamics of the system.

³This contrasts the more complicated choice examining distinct factors in the analytic calculation.

the electric field and plaquettes:

$$j_{\text{div}}(X, \Delta \mathbf{x}) = \alpha(\Delta \mathbf{x}) \left(\frac{1}{\Delta x_0} \frac{1}{\mu_0 c} (E_1(T, X_3) - E_1(T - 0, X_3)) + \frac{1}{\Delta x_1 (\Delta x_3)^2} \frac{\hbar}{q \mu_0} \text{Im} \{U_{13}(T, X_3) - U_{31}(T, X_3 - 3)\} \right). \quad (6.2)$$

This, thus, provides the expressions for determining the renormalization coefficient. The renormalization procedure correspondingly involves evaluating the unrenormalized current minus this contribution in the electric field dynamics (5.58). This effectively implies modifying the equation to include a factor of $1 + \alpha(\Delta \mathbf{x})$ multiplying each electric field term and plaquette to, thus, obtain the renormalized dynamics.

6.4.2 Evaluating the Renormalization

Considering the expression (6.2) in the simple case involving a static state and the magnetic gradient identical with both the lattice spacings therefore yields

$$\alpha(\Delta \mathbf{x}) = \Delta x_1 (\Delta x_3)^2 \frac{q \mu_0}{\hbar} \frac{j_f(X, \Delta \mathbf{x}) - j_f(X, \Delta \mathbf{x}_{\text{ref}})}{\text{Im} \{U_{13}(T, X_3) - U_{31}(T, X_3 - 3)\}} + \alpha(X, \Delta \mathbf{x}_{\text{ref}}).$$

This, thus, determines the renormalization coefficient at any lattice spacing. The evaluation involves measuring the unrenormalized current at both the relevant scale and at a reference lattice spacing for an identical, set magnetic field in both cases, with also the renormalization coefficient specified at the reference lattice spacing.

This reference coefficient forms a constant addition to the expression, and correspondingly to the unrenormalized current at any scale. The (unphysical) divergence in the current, thus, occurs independently of this piece. This, therefore, implies the precise value of this term may simply be ignored for obtaining

the physical, convergent current⁴. Alternatively, this constant piece may be considered to arbitrarily define the scale of the renormalization and accordingly the value simply set at the reference lattice spacing to define the renormalization scheme. The simplest case may therefore impose the coefficient at the reference scale to equal zero.

Obtaining the convergence in the current regardless may thus result on determining the renormalization coefficient specified through

$$\alpha(\Delta\mathbf{x}) = \Delta x_1(\Delta x_3)^2 \frac{q\mu_0}{\hbar} \frac{j_f(X, \Delta\mathbf{x}) - j_f(X, \Delta\mathbf{x}_{\text{ref}})}{\text{Im}\{U_{13}(T, X_3) - U_{31}(T, X_3 - 3)\}} + \alpha(X, \Delta\mathbf{x}_{\text{ref}}), \quad (6.3)$$

and the corresponding physical current replacing the bare current in the dynamics may fully specify the renormalization scheme to yield the physical dynamics.

To obtain the renormalization coefficient may in practice be accomplished through simulating the fermion and gauge-field evolution (without the Higgs-superconductor) from the initial vacuum-configuration to the final static state. Setting the gauge field manually ensures an identical magnetic gradient in each case. A simple scaling in time may uniformly multiply the final configuration to increase the field from zero to the final static, state; in particular the scaling (5.84) may provide a smooth variation⁵.

⁴A standard interpretation of the renormalization procedure considers the process to modify the coupling constant in the system. The particular expression of the gauge terms in this system excludes an explicit coupling constant multiplying the gauge-field tensor in the action. A simple field redefinition though may produce this form in an equivalent action, and hence the addition of renormalization terms multiplying the field tensor may be factorized to form a single, new coefficient. This factor thus incorporates the renormalization coefficient; and the resultant term multiplying the field tensor defines effective coupling. Determining the precise value of the renormalization coefficient therefore determines the effective coupling; the neglecting of the constant contribution to the renormalization coefficient thus simply prevents the precise determination of the effective coupling constant in the system.

⁵The electric field definition on the lattice implies the time-varying gauge field forms a non-zero electric field, ultimately vanishing in the final, static state. This time -variation, thus, models a damping of the electric field in the evolution to the final state.

Imposing the tanh variation in the continuum, further, implies the resultant electric field varies proportionally to $\text{sech}^2(\tan(\pi t/\tau - \pi/2))$. Hence in the limit $t \rightarrow \tau$, the electric field decays approximately exponentially. The final decay in the equivalent discrete-case, notably therefore, models an exponentially-damped field.

Further, the sech variation at times close to zero determines the electric field increases ap-

The static solution to the pure gauge-dynamics in the continuum – omitting the Higgs-field, fermion and Wilson currents – readily provides a suitable analytic expression for the final gauge-field. This configuration reasonably approximates the result on the lattice in the full dynamical case including also the (expectedly perturbative) fermionic currents.

Substituting the chosen form (5.83) of the external current into the consequent dynamics in particular determines the final state:

$$\frac{1}{\mu_0} \partial_3 B_2(t, x_3) = \frac{1}{\mu_0} \partial_3^2 A_1(t, x_3) = |J| \exp\left(-\frac{(X_3 - z_1)^2}{2\sigma^2}\right) - |J| \exp\left(-\frac{(X_3 - z_2)^2}{2\sigma^2}\right).$$

Integrating this expression once hence determines

$$B_2(t, x_3) = \partial_3 A_1(t, x_3) = \mu_0 \sqrt{\frac{\pi}{2}} \sigma |J| \left[\operatorname{erf}\left(-\frac{(X_3 - z_1)^2}{2\sigma^2}\right) - \operatorname{erf}\left(-\frac{(X_3 - z_2)^2}{2\sigma^2}\right) \right] + B_C. \quad (6.4)$$

The condition on the magnetic field to form anti-symmetrically in the two, separate regions between the external currents on the periodic boundaries (see Section 5.7) constrains the arbitrary constant. For the current peaks positioned to divide the periodic z -axis into two equal regions, simply subtracting half the maximum height of the combined error function pieces yields a suitably symmetric form: the error functions matching the requisite symmetry except about

proximately exponentially in the continuum; and accordingly the discrete analogue models a similarly smooth increase in the initial electric field on the lattice.

the half-maximum value rather than zero. This thus determines the constant satisfies

$$B_C = -\mu_0 \sqrt{\frac{\pi}{8}} \sigma |J| \left[\operatorname{erf} \left(-\frac{(z_M - z_1)^2}{2\sigma^2} \right) - \operatorname{erf} \left(-\frac{(z_M - z_2)^2}{2\sigma^2} \right) \right],$$

$$z_M = \frac{z_1 + z_2}{2}.$$

Integrating the resultant expression again hence determines

$$A_1(t, x_3) =$$

$$\mu_0 \sqrt{\frac{\pi}{2}} \sigma |J| \left[(X_3 - z_1) \operatorname{erf} \left(-\frac{(X_3 - z_1)^2}{2\sigma^2} \right) - (X_3 - z_2) \operatorname{erf} \left(-\frac{(X_3 - z_2)^2}{2\sigma^2} \right) \right.$$

$$\left. + \sqrt{\frac{2}{\pi}} \sigma \exp \left(-\frac{(X_3 - z_1)^2}{2\sigma^2} \right) - \sqrt{\frac{2}{\pi}} \sigma \exp \left(-\frac{(X_3 - z_2)^2}{2\sigma^2} \right) \right] + B_C X_3 + A_C.$$

The symmetry constraint on the magnetic field further indicates the gauge field ranges between equal and opposite values. This, hence, constrains the half-maximum value to zero. Subtracting the value at the location $X_3 = z_M$ midway between the current peaks correspondingly imposes the constraint and thus sets the second integration constant. This therefore fully defines the express analytic form of the gauge field in the final, static state.

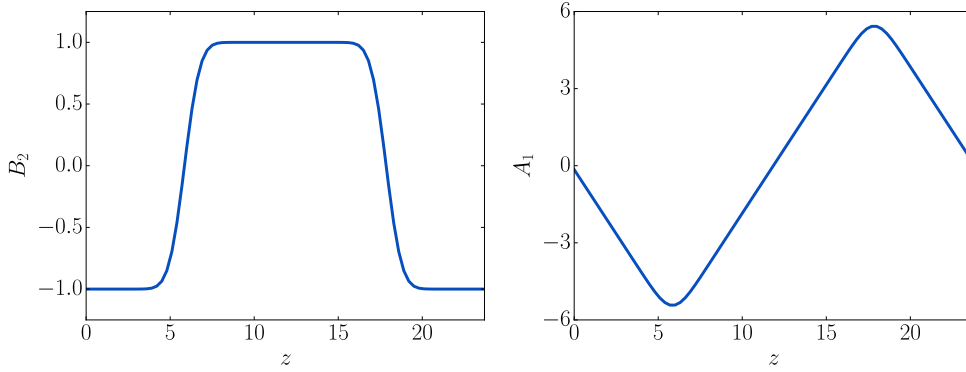


Figure 6.2: The magnetic field (left) and gauge field (right) evaluated analytically for calculating the renormalization coefficient.

This gauge-field configuration and the tanh prefactor thus together provide the analytic expression of the magnetic field to determine the renormalization coefficients numerically.

Setting the current width to satisfy $2\sigma^2 = 1$, for simplicity, and choosing the amplitude J to set the magnitude of the analytic magnetic field to $B_{\max} = 1.0$ (comparable to the subsequent, fully-dynamical simulations) in the analytic expressions generates the final gauge field and corresponding magnetic field, shown in figure 6.2.

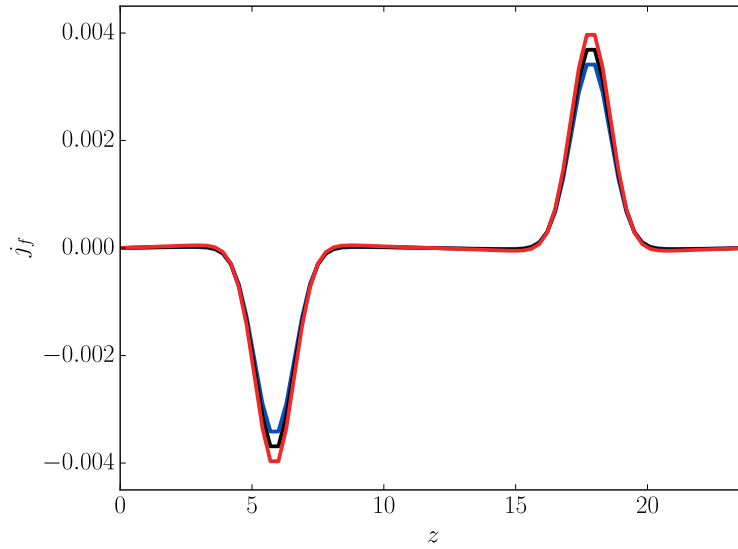


Figure 6.3: The fermionic current in the x -direction generated by the analytically set gauge-field for $\Delta x_1 = 0.4$ (blue), 0.3 (black), 0.2 (red) with $\Delta x_2 = \Delta x_3 = 0.3$ and the physical volume constant; $\Delta x_0 = 0.002$, $|J| = 1$.

Determining the renormalization coefficients consequently for differing Δx_1 demonstrates the effectiveness of the renormalization scheme. Setting the lattice spacing in the x -direction separately to $\Delta x_1 = 0.4, 0.3, 0.2$ while fixing $\Delta x_2 = \Delta x_3 = 0.3$ and in a fixed physical volume of $L_x = L_y = 9.6$ and $L_z = 24$ produces the unrenormalized fermionic current – including both the fermion and Wilson parts – illustrated in the figure 6.3. Choosing the combined fermion-

and Wilson-current generated at $\Delta x_3 = 0.3$ to provide the reference with the determined magnetic gradient and the measured current substituted into the expression (6.3) hence yields the renormalization coefficients.

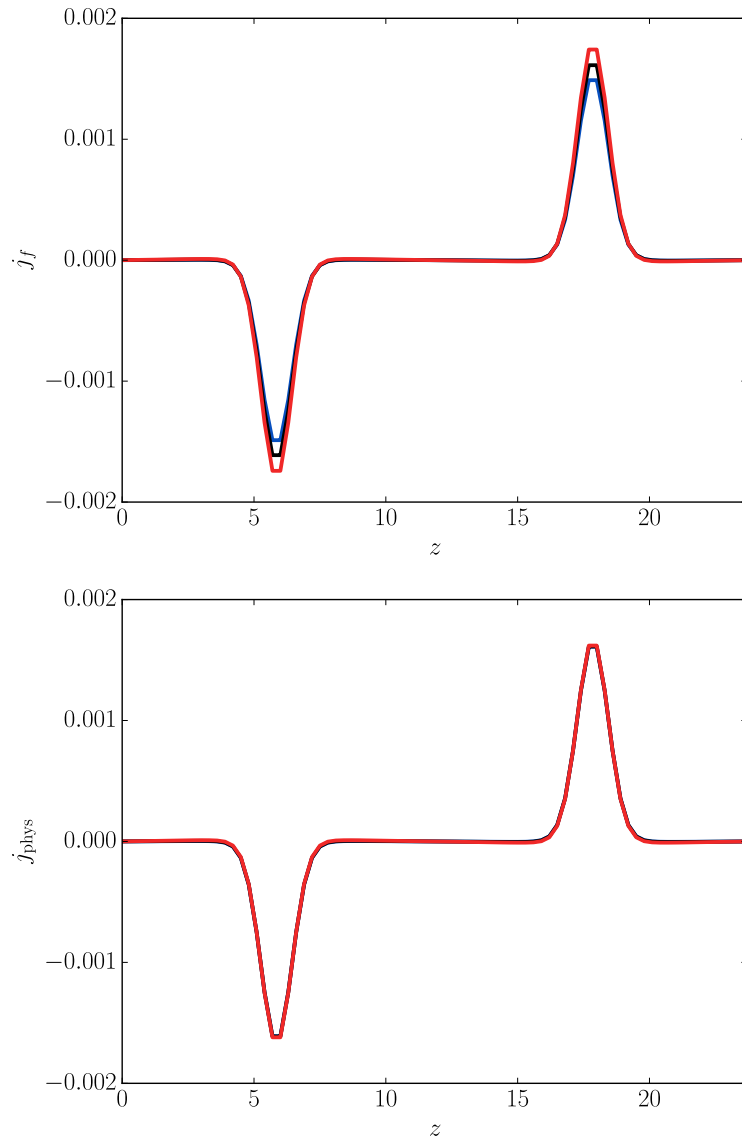


Figure 6.4: The fermionic current in the x -direction in the fully-dynamical simulations without renormalization (top) and with renormalization (bottom) for $\Delta x_1 = 0.4$ (blue), 0.3 (black), 0.2 (red) with $\Delta x_2 = \Delta x_3 = 0.3$ and the physical volume constant; $\Delta x_0 = 0.002$, $|J| = 0.5$ and $\zeta = \pi/6$.

The coefficient in principle is coordinate independent; in practice though, numerically determined value varies both in time and along the z -direction. Averaging the unrenormalized current over times much longer than the typical temporal fluctuations though helps reduce this random error. The peaks in the external current offer a definite and distinctive location for determining the precise coefficient-value; while the anti-symmetry in the peak locations implies the averaging the coefficient evaluated at both peaks may help further reduce the error. These peak values though notably occur at sites off the lattice and hence the simulations provides no direct measure of the unrenormalized-current at this location. Obtaining the numerically measured current at the two adjacent sites of the peak provides a simple alternative while retaining the distinction and definiteness of the location. The time-averaged value of the current at these four sites and the average of the corresponding coefficients in the physical current therefore fully defines the renormalization procedure.

For the cases $\Delta x_1 = 0.2, 0.4$, this yields respectively $\alpha = -0.000265269471$ and $\alpha = 0.00026365064$. Implementing these renormalization parameters in the equivalent fully-dynamical case (for the respective lattice spacings with both the volume and time-step identical to the manual analysis) yields the renormalized current illustrated in figure 6.4, bottom. A comparison of the renormalized currents to the unrenormalized current (top) in figure 6.4 – especially at the peaks (coincident with the peaks in the external current) – clearly demonstrates the procedure effectively eliminates the lattice-dependent divergence. The concomitant magnetic field in the renormalized case further confirms the effectiveness: the figure 6.5 demonstrates the closely distributed values of the field after renormalization.

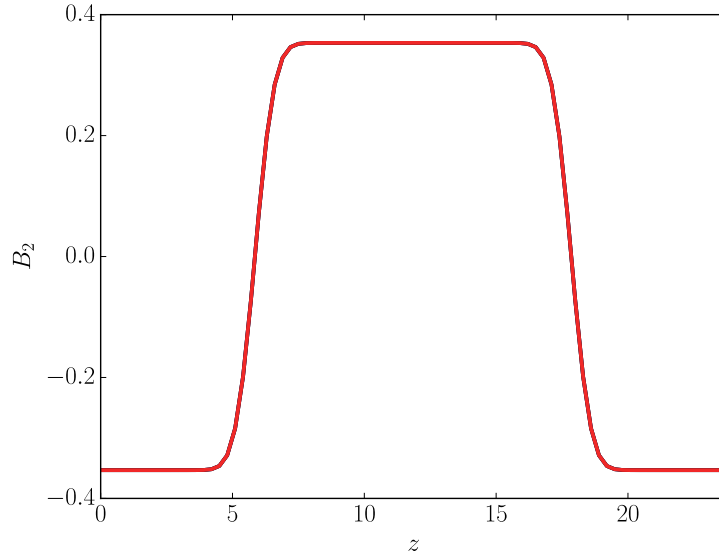


Figure 6.5: The magnetic field in the dynamical simulations with renormalization for $\Delta x_1 = 0.4$ (blue), 0.3 (black), 0.2 (red) with $\Delta x_2 = \Delta x_3 = 0.3$ and the physical volume constant; $\Delta x_0 = 0.002$, $|J| = 0.5$ and $\zeta = \pi/6$.

These example cases, confirming the convergence in the observable values, therefore validate the selected lattice-parameters and the corresponding renormalization coefficient for examining the superconducting system. In particular, the parameters setting the lattice spacing equally to 0.3 where also $\alpha = 0$ are chosen for simplicity throughout the subsequent simulations.

6.5 Tunnelling System on the Lattice

6.5.1 Wall Parameters

Fixing the skin width of the barriers to smaller than the lattice spacing and the thickness of each to $d = 1.5$ forms the narrowest feasible barrier – only five sites, for the chosen lattice spacing – to reliably examine the transmission through the barrier. This, in particular, includes a region on the lattice entirely within the barrier and not purely on the surface, to examine the transmission without simply

examining any surface effects. The minimizing of the barrier thickness further ensures the maximum potential to observe the fermionic tunnelling. Setting the separation of the barrier centres to $S = 5.7$ prevented an overlap of the the edges for the barrier thickness chosen. This also created a reasonably sized region (larger than both the skin width, $\delta < 1$ and the chosen thickness $d = 1.5$) enclosed between the barriers where the magnetic field transmitted through the sheets could form without further interference of the barriers. Positioning the barriers centrally between currents (see Section 5.7.2) requires setting the midpoint of the barriers to $M = N_3\Delta x_3/2 = L_z/2$ for the choice of length L_z on the lattice. This, for simplicity, creates an identical region where the magnetic field may form between the current and barrier on both sides external to the enclosed volume

6.5.2 Lattice Parameters

Implementing the renormalized dynamics for the lattice spacing $\Delta x_1 = \Delta x_2 = \Delta x_3 = 0.3$ in the volume of length $L_x = L_y = 9.6$ and $L_z = 18$ with the Neumann boundaries forms the discretized system for examining transmission through the the superconducting barrier. The chosen length in the z -direction further offered sufficient space to produce an almost uniform magnetic field in the region between the barrier and the external-current width with a region to examine the field penetrating the barrier: the figure 6.6 (top) shows a typical configuration in the static state.

Setting $\Delta x_0 = 0.002$ provided time-step necessarily smaller than the lattice spacing and sufficient to readily yielding convergence in the observable parameters; while setting $\tau = 80$ to transition from the vacuum to the static state further provided a practicably brief transition with negligible transient features perturbing the static state.

The lattice discretization intervals, further, involved a total number of lattice sites readily implemented on a computer; while this total lattice size, along with the choice of temporal discretization-interval and the brief initial-increase time

ensured numerical evaluation within a practicable time-frame.

6.5.3 Typical, Magnetic-Field Transmission

Setting the external-current magnitude to $|J| = 0.5$ with the width $\sigma = 0.8/\sqrt{2}$ while varying the squared wall-strength through $\eta = [2, 7.5]$ in half-integer increments will provide the specific configuration for examining the transmission on varying the wall strength.

The analytical estimates indicating the bound for detecting the tunnelling signal (Section 5.3) determines the maximum wall-strength. Examining the transmission, therefore, up to $\eta = 7.5$ will sufficiently encompass the region where the tunnelling signal is expected to dominate.

Choosing the increase in the external current to the final, maximum amplitude in a time $\tau = 80$ produces increasing fields until this time. The generated electromagnetic waves subsequently decay: their amplitude rapidly negligible, with the damping coefficient set to $\zeta = 6\pi/35$. This hence generates the essentially static, final state before $X_0 = 150$, when the resultant fields are examined.

The figure 6.6, top illustrates the typical magnetic field variation in the static state: the field strongly decays through even the narrow wall to a magnitude several orders smaller in between the superconducting barriers.

A significant Higgs current also occurs within the wall: the figure 6.6, bottom demonstrates the typical form. The Higgs current varies essentially $\propto A_1\rho^2$; hence, the decrease in the current occurs, essentially, due to the decay in the gauge-field, while the sharp peak at the boundary results through the almost step-function variation in ρ . This current also notably acts in accordance with Lenz's Law to essentially oppose the magnetic flux generating the current: the current aligns in the negative x -direction to form a magnetic field counteracting the gauge field generated by the external current. The Higgs current, in the absence of any fermion contribution, notably coincides with the several orders decrease in the magnetic amplitude through the barrier; the current, thus, corresponds to the

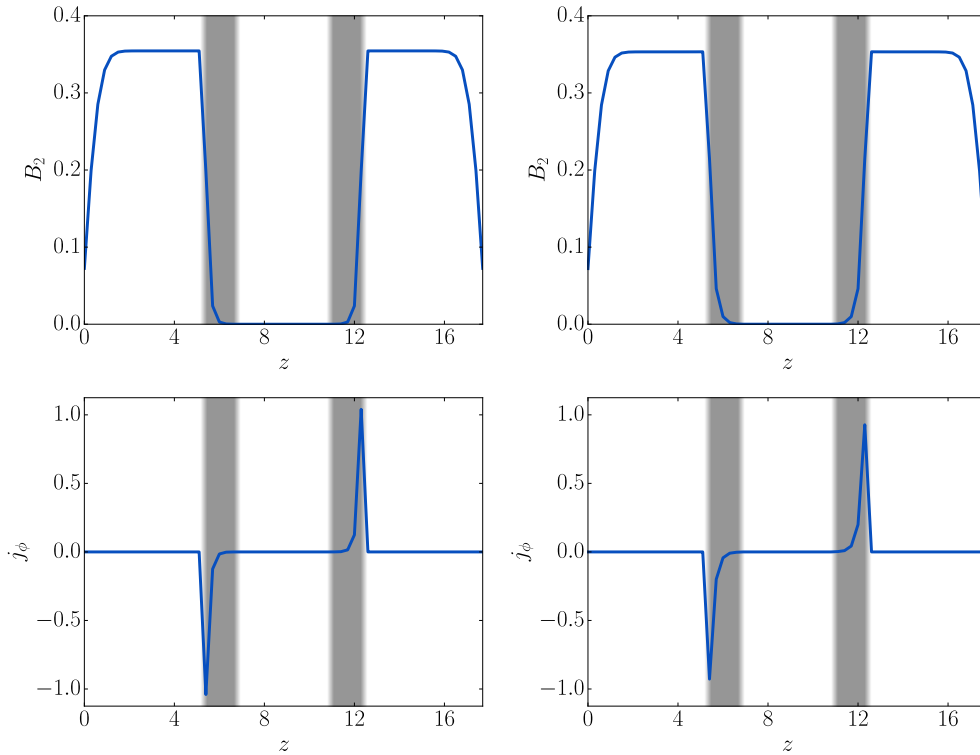


Figure 6.6: The typical magnetic field (top) and Higgs-current (bottom) without fermions (left) and with fermions (right) in the presence of the superconducting barrier (grey-shaded region): $|J| = 0.5$, $\eta^2 = 8$.

purely classical decay in the magnetic field.

This strong decay in the magnetic field notably results both with and without the fermions: the figure 6.6, top and right incorporating fermions and the case excluding fermions in figure 6.6, top and left demonstrate the typical similarity. The Higgs superconductor-current, both with and without fermions, thus produces the most substantial change in the magnetic field.

A comparably small fermionic current results within the barrier: the figure 6.7 illustrates the fermions within the barrier typically generate a combined fermion- and Wilson-current several orders of magnitude smaller than the Higgs current. The fermionic current thus forms a sub-dominant effect in the field decay.

This current may, nonetheless, generate a significant contribution to the

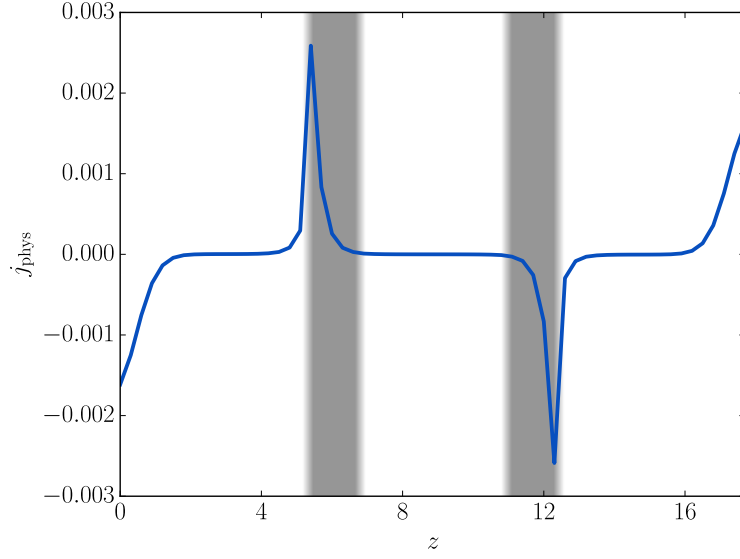


Figure 6.7: The typical fermion current in the presence of the superconducting barrier (grey, shaded region): $|J| = 0.5$, $\eta^2 = 8$.

transmission where the resultant change in transmission becomes comparable to the classical transmission. The typical fermion contribution forms an additional current opposing the Higgs current within the barrier. This fermionic contribution, hence, counteracts the Higgs-field suppression of the magnetic field to increase the magnetic transmission. The fermion current, moreover, comprises the fermions formed within the barrier and therefore effectively includes the particles contributing to the tunnelling. These particles, in counteracting the Higgs suppression to increase the transmission, thus act in qualitative accordance with the tunnelling effect. Both the fermion and Higgs current within the barrier vary on the change in the barrier strength and thus complicate the precise correspondence between the fermionic current and the tunnelling amplitude. Examining the magnetic transmission, regardless, may enable measurement of the resultant tunnelling.

The fermionic current, further, at the boundaries acts in accordance with Lenz's Law. These currents, thus, align opposite to the external current and,

hence, generate a magnetic flux opposing the field corresponding to the external current. Increasing the wall strength without fermions also, notably, alters the magnetic field amplitude in the regions between the boundary and superconductor. This variation in the presence of fermions, reacting to the external current in accordance to Lenz's Law, causes the induced fermion current to generate a magnetic flux, varying on the change in wall strength. The resultant magnetic field in the regions between boundary and the superconductor thus varies on the change in wall strength, both with and without fermions; and the resultant fields differ in the case with fermions, compared to the equivalent case without the fermions.

This variation in the external magnetic field, thus, prevents a direct comparison between the field transmission on varying the wall strength or on including the fermions. Forming the ratio of the central value between the superconducting barriers, to a representative field-value external to the superconducting enclosure provides an equivalent variable for directly comparing the differing cases:

$$B_R = \frac{B_{\text{int}}}{B_{\text{ext}}}. \quad (6.5)$$

To attribute the variation in this ratio purely to the changes in wall strength and the presence (or absence) of fermions neglects the potentially complex variation in the transmitted electric field related simply to the changes in the external field. This variation, though, may approximate a linear relation over a sufficiently small range in the external field. The ratio in this limit meaningfully comprises the proportionality constant distinguishing the linear relation; and, thus, within the linear regime, represents the transmission independently of the precise external field. Examining a common range of the external field in each case, further, forms a suitably equivalent context for comparison.

The magnetic field halfway between each boundary and the adjacent wall provides a definite representative-value external to the superconductor within

the accurately-uniform region; while the symmetry in the system implies an identical magnetic field forms at these two positions. Averaging the field at both locations, hence, may reduce the computational error in the measured exterior field-value. Selecting the central field value between the superconducting barrier may provide a definite, distinctive location to measure the transmitted magnetic field.

These specified positions, though, in practice, may occur off the defined lattice-sites. The only minor deviation from uniform over a wide region external to the superconductor ensures in this case that the field value at the adjacent sites provides a highly similar value to the field at the off-lattice site; and thus essentially yields an equally-representative value of the field external to the superconductor. Selecting, in particular, the field value at the adjacent site closest to the boundary when the defined external-location occurs off the lattice, therefore, provides the external-field values to average. Comparing these in each case to the field at the adjacent site, but nearer the barrier, and assuming a smooth variation in the field between the lattice sites may, hence, provide an upper bound on the deviation between the field at the specified site and the measured value at the adjacent site nearer the boundary. The magnitude of this difference for each case in the subsequent data set to measure the tunnelling (figure 6.9) equals $\sim \mathcal{O}(10^{-5})$ per cent of the representative value used in computing the transmission. This confirms the chosen, adjacent site provides a highly comparable value to the true measurement at the defined location, off the lattice; the measured field, therefore, forms an equally suitable, representative value for examining the transmission ratio.

The field value inside the superconducting enclosure also varies very little; hence, the values at the adjacent sites to the midpoint between the barriers, when the midpoint occurs off the lattice may provide a suitably-representative value of the internal field. Further, the symmetry in the system implies the field at these sites are equal, and thus either value may equivalently define the

internal value. Averaging the pair therefore technically reduces the error in this representative value. These field values thus practically define the internal and external fields examined on the lattice.

Varying the current through the range $|J| = 0.5, 0.5 + 5 \cdot 10^{-5}, 0.5 + 5 \cdot 10^{-4}, 0.5 + 5 \cdot 10^{-3}$ for a fixed wall-strength produces a variable, external – and correspondingly varied, internal – magnetic field. Calculating the linear-regression fit to these correlated variables, hence, yields the proportionality constant describing the magnetic transmission.

The figure 6.8 shows the typical ratio and linear regression both with and without fermions for the examined wall-strengths within a common range of the external field.

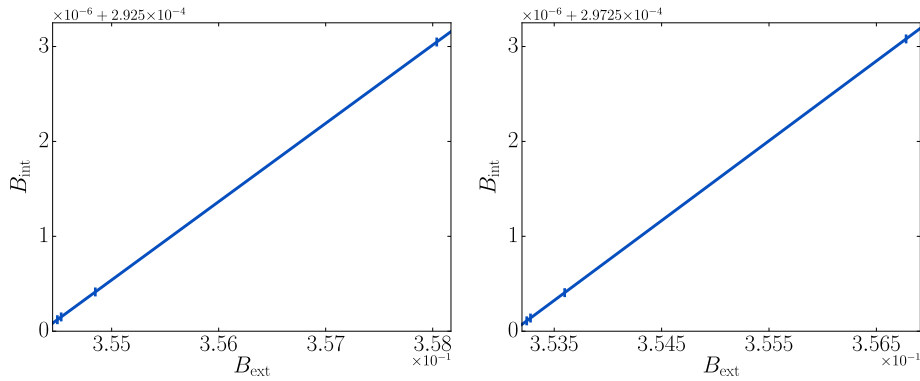


Figure 6.8: The typical variation in magnetic field inside the shielded region (B_{int}) on varying the uniform, external field (B_{ext}) both without (left) and with (right) fermions. These demonstrate the highly linear relation between these fields over approximately an order or magnitude in the external field.

These cases illustrate the highly linear relation between the external and internal currents over around an order of magnitude range in the external field. The wall strength and presence of fermions affecting the generated field causes the precise range to vary within each case; but these various regimes, importantly, include a common range.

This high linearity, therefore, confirms the suitability of the ratio for describ-

ing the transmission; while the common range enables the examination of the differing transmissions in a consistent context. These ratios thus form a suitable variable for comparing the transmission.

6.5.4 Tunnelling of the 3rd Kind: Detection

Evaluating the magnetic field ratio for the chosen range in wall strength forms the method for quantifying the transmission dependency on the barrier strength both with and without fermions.

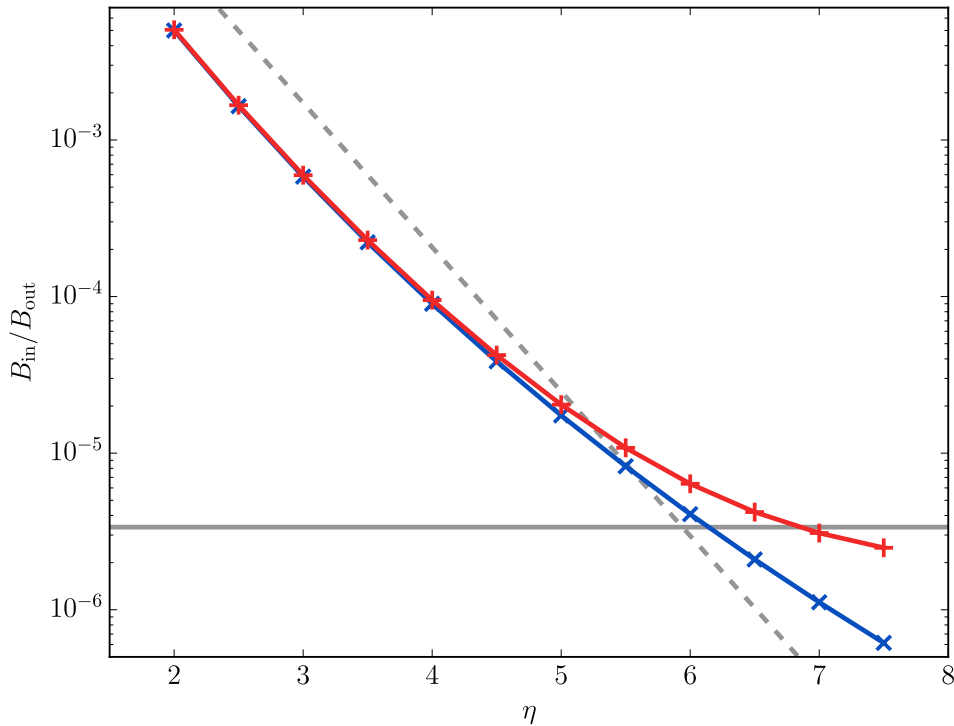


Figure 6.9: The ratio of magnetic fields inside and outside the box, when varying the wall strength η with (red) and without (blue) fermions. Also shown is the analytic estimate (5.31) of the classical transmission (grey, dashed) and the result of the perturbative calculation (5.30) (grey, solid) for $m = 1$, $e = 1$, $q = 0.3$ and $d = 1.5$. (Note the log scale.)

The figure 6.9 illustrates the measured variation in the transmission ratio.

Both the case with (red line) and without (blue line) fermions, for low wall strengths of $\eta \lesssim 5$ produce effectively identical transmission. This indicates the classical transmission dominates within this regime of wall strength. The figure also shows the simplistic heuristic guide (grey, dashed line) for comparison. This simple estimate differs in the absolute value; the discrepancy, though, is expected to result, considering the classical guide neglected both the finite volume and discretization effects on the transmission in the fully dynamical simulations (see also the discussion on this in Section 5.3). The simulation results in the weak barrier regime, nonetheless, notably form the exponentially decaying relation predicted in the simplistic, classical estimate: thus, further confirming the dominance of classical effects within this regime.

Significant differences in the measured transmission with the fermions, compared to without begin where $\eta \approx 5$. The increasing barrier strength produces a progressive decrease in the case without fermions, while the system with fermions begins to asymptote to a value around $2 \cdot 10^{-6}$. This indicates the quantum interaction affect the system more markedly within this regime of barrier strength.

The computed transmission without the fermions also noticeably grows to values larger than continued exponential decreasing transmission predicted through the simple guide. This may simply result since the measured external field is lower than the actual magnetic field strength incident on the barrier.

Although the magnetic field forms a predominantly level region outside the superconducting enclosure (see figure 6.6 for an illustrative case), the magnetic field, actually, increases slightly towards the barrier. This rise, thus, implies an increased in the field of $B_{\text{err}} \sim \mathcal{O}(10^{-5})$ incident on the barrier, compared to the measured external-field, at the position only partway between the boundary and the wall (see Section 6.5.3). The stronger magnetic field incident on the barrier causes a larger, classical transmission compared to the classical estimate for the measured external field. This may, hence, significantly increase the measured transmission-ratio without fermions, compared to the classical guide where the

discrepancy in the ratio matches the order of the classical estimate. Examining the classical estimate (5.31) determines the increased, incident field value of $B_{\text{err}} \sim \mathcal{O}(10^{-5})$ yields an approximately $\mathcal{O}(10^{-4})$ increased transmission ratio for the measured external field value of $B_{\text{ext}} \sim \mathcal{O}(10^{-1})$ (see the figure 6.6 for an illustrative case), in contrast to the classical estimate for the measured external value. (The consequent variation is also reasonably assumed, simply, to superimpose on the finite volume and discretization effects expected to alter the classical guide – and evidenced for the low barrier-strengths.) This, therefore, indicates the discrepancy in the incident field generates a significant affect where $\eta \gtrsim 4$ and this effect grows. The measured transmission-ratio without fermions, notably, increases slightly at $\eta \sim 4$, to a slower decay compared to the strictly exponential form, predicted in the classical estimate; and this grows on increasing wall-strength until the transmission ratio exceeds the classical guide. These deviations, thus, match the discrepancy expected simply through the difference in the incident field on the wall and the measured external value.

The classical estimate indicates the magnetic transmission tends to zero on increasing barrier strength, irrespective of the magnitude of the external field. This implies any contribution independent of wall strength will dominate for sufficiently high wall strength. The decay to zero of the classical transmission, thus, assures the asymptoting to a fixed value for $\eta \gtrsim 5$ in the simulations with fermions results through the quantum contributions to the transmission. This asymptotic value equal to around $2 \cdot 10^{-6}$, moreover, matches the analytic result (grey, solid line) to within the expected factor of two. The numerical transmission, though, notably, tends to a value slightly lower than the analytic estimate. This may result through the measurement of the magnetic field at a finite distance inside the enclosure. The analytic calculation evaluates the tunnelling expectation infinitely far from the barrier, where the entirety of the fermions tunnelling through the barrier may be expected to have (re-)combined to generate magnetic field. In contrast, the simulations measure the magnetic

field near the barrier, compared to the width of the barrier. The finite fermion current (if smaller than visible on the scale for the illustrative case in figure 6.7) generated inside the superconducting enclosure, from an initial absence of current in the vacuum, indicates a small portion of the fermions having tunneled through the barrier remain to (re-)combine into magnetic field. These fermions, hence, reduce the transmitted field compared to the complete conversion expected at infinite distance and, thus, may cause the slightly lower measured value of the tunnelling contribution.

Repeating the analysis, using different lattice spacings, for a fixed physical volume and fixed couplings may provide a quantitative estimate of the numerical error in the measured transmission. The variation in the observed fields on the change in lattice spacing would indicate the dependence of the discretization errors on the lattice spacing. Evaluating this error for the lattice spacing in the simulation, hence, would provide a quantitative measure of the discrepancy between the computed and analytic estimates resulting simply through discretization; any remaining deviation might be attributed to physical effects. This computationally intensive analysis to compute the numerical errors in the transmission, currently though, remains a work to complete. The discrepancies without distinguishing the numerical errors, notably, nonetheless, match the qualitative expectation on considering the physical effects in the system. This provides assurance the results accurately demonstrate the physical, field transmission.

The strong deviation in the case on incorporating fermions, compared to without, and the transmission ratio asymptoting to a constant, slightly below the analytically determine value, therefore, forms a reasonable confirmation of the analytic estimate. This result likewise indicates the measured fermionic current includes the tunnelling fermions and, thus, the dynamical system incorporates the tunnelling of the 3rd kind.

6.5.5 Conclusion

The work in this chapter has, in summary, developed and refined the techniques for examining tunnelling of the 3rd kind in real-time simulations. This distinct form of tunnelling provides a potentially interesting application of quantum field effects in a laboratory arrangement. The simulations have examined this phenomenon in an idealized laboratory scenario where two parallel and infinite superconducting planes shield a central region from the uniform magnetic field in the regions to either side. These superconducting sheets strongly suppressing the magnetic transmission form the classical barrier to the external magnetic field. The simple estimate of this effect predicted the exponential decay in the transmission. Incorporating the quantum effects also enables the magnetic field external to the barrier to convert into fermionic particles. These cross unhindered through the barrier with the subsequent annihilation (re-)creating the magnetic field. This tunnelling of the 3rd kind thus contributes to the magnetic transmission through the barrier. The perturbative calculation of this effect implies the resultant transmission equals only around $3.4 \cdot 10^{-6}$ times the external field with a possible correction to this by a factor between one to two – accounting for the differences between the analytic calculation and the numerical simulation. This effect becomes detectable only where the superconductors reduce the classical transmission to less than the tunnelled component. The combination of the classical decay and the tunnelling effected together formed the basic estimate for the expected transmission both with and without the fermions.

These results matched the dynamical simulations with significant accuracy. The decay on increasing wall-strength without fermions qualitatively reproduced the estimated exponential-decrease to reasonable precision; though, the absolute numerical values were significantly less than the analytic estimate. This discrepancy likely resulted through the intricacies involved in implementing the results in the finite volume on the lattice, unaccounted for in the simple estimate. The

transmission without fermions also demonstrated a slightly slower than exponential decay where $\eta \gtrsim 5$. This simply occurred through the consistently larger field incident on the barrier compared to the measured external field generating a significant increase in the transmission for the larger wall strengths. The tunnelling signal of $B_{\text{in}}/B_{\text{out}} \approx 2 \cdot 10^{-6}$, significantly, equalled the perturbative estimated within the expected correction factor. Determining the discretization errors in the result may be accomplished on the repetition of the simulation using different lattice sizes, for a fixed physical volume and fixed couplings. This may enable quantifying the lattice spacing errors and, correspondingly, distinguishing the genuine physical discrepancies between the numerical results and the analytic estimates. The qualitative consistence in the discrepancies to the expected deviation, nonetheless, validated the physical nature of the computed transmission. These results, therefore, provided a reasonable confirmation of the tunnelling-effect, and the perturbatively calculated transmission signal. The successful implementation of the system indicates, further, the potential for real-time simulations of fermionic systems to produce accurate predictions for testing in the laboratory.

This numerical simulation of tunnelling were accomplished on applying the established techniques for dynamical fermions to the idealized experimental arrangement. The ensemble method offered a possible procedure to solve the dynamics analogously to the oscillon system. This essentially involved the statistical average of ordinary numbers replacing the ladder operators for evaluating the fermionic correlators. The method required an additional set of fields in contrast

to the purely bosonic case. These “male” and “female” fields respectively were of the form

$$\Psi_{M,c}(x) = \sqrt{\frac{\hbar c}{2}} V_x \sum_s \sum_{\mathbf{K}} \frac{\Delta k_1}{2\pi} \frac{\Delta k_2}{2\pi} \frac{\Delta k_3}{2\pi} \frac{1}{2\omega_{\mathbf{K}}} \left[\xi_{\mathbf{K},s,c} \psi_{\mathbf{K},s}^{(U)}(X) + \zeta_{\mathbf{K},s,c} \psi_{\mathbf{K},s}^{(V)}(X) \right],$$

$$\Psi_{F,c}(x) = \sqrt{\frac{\hbar c}{2}} V_x \sum_s \sum_{\mathbf{K}} \frac{\Delta k_1}{2\pi} \frac{\Delta k_2}{2\pi} \frac{\Delta k_3}{2\pi} \frac{1}{2\omega_{\mathbf{K}}} \left[\xi_{\mathbf{K},s,c} \psi_{\mathbf{K},s}^{(U)}(X) - \zeta_{\mathbf{K},s,c} \psi_{\mathbf{K},s}^{(V)}(X) \right],$$

where the minus sign between the terms of the integrand distinguishes the two sets. This difference, importantly, ensures the statistical variance of the male and female fields in combination can reproduce the potentially negative values of the fermionic correlators.

The ensemble method for the fermions – equivalently to the oscillon case – offered the possibility to reduce the computational requirements. This method, in principle, entails infinitely many fields to precisely reproduce the quantum correlators. The use, though, of a finite ensemble, in practice, may adequately approximate the correlators. Had this finite ensemble in the fermionic system involved fewer fields than the total modes in the 3 + 1D system, the ensemble technique may have offered the possibility to readily evolve the system. The trial simulation involving the male and female fields, though, indicated a small ensemble, equal to two and a half per cent of the total modes, produced substantial statistical-noise in the fermionic current; this strongly distorted the formation of the uniform magnetic field. This demonstrated the need for a much larger ensemble size to accurately evolve the fermions. The comparatively small ensemble in the trail case also required over 156 hours (real-time) to simulate. This indicated the impracticable times required for the larger ensemble and therefore the unsuitability of this method for simulating the system.

Imposing the symmetries of the system explicitly on the fields provided the alternative method for simplifying the system. The superconducting planes aligned parallel and extended infinitely in the x and y directions, with the magnetic field

also aligned parallel to the planes essentially formed a homogeneous system orthogonal to the z -axis. This, hence, determined the ansatz for the fields:

$$A_1(x) = A_1(t, x_3), \quad A_2(x) = A_3(x) = 0;$$

$$j_1(x) = j_1(t, x_3), \quad j_2(x) = j_3(x) = 0;$$

$$\theta(x) = 0;$$

$$\psi_{(k_1, k_2, \lambda, s)}^{(U/V)}(x) = e^{ik_1 x_1} e^{ik_2 x_2} \chi_{(k_1, k_2, \lambda, s)}^{(U/V)}(t, x_3).$$

The ansatz effectively reduced the dynamical equations to a 1+1D system in the z -direction with the quantum correlators involving a sum also over the x - and y -directions in mode space. This produced a significant decrease in the field values to compute on the lattice and the consequent simulation times. The ansatz evolution typically required under an hour (real-time) for each simulation. This greatly improved on the ensemble method timings and, moreover, provided a practicable method for examining the tunnelling. The considerable increase in efficiency thus demonstrates the potential power of a suitable ansatz to significantly reduce the computational times in fermion simulations.

Chapter 7

Summary and Outlook

This work has presented the first dynamical, quantum simulations of oscillons. The precise quantum treatment of the decay substantially reduced the oscillon lifetimes. These structures classically lasted longer than $\mathcal{O}(10^4 |m|^{-1})$ (while simulations have demonstrated them to last longer than $\mathcal{O}(10^6 |m|^{-1})$ [37, 41, 43, 44]) and most remained beyond the end of the simulations. The structures in the quantum evolution, in contrast, lasted less than $\mathcal{O}(10^3 |m|^{-1})$ with the decay in all cases occurring before the end of the simulation. These also decayed gradually: in contrast to the abrupt endpoint (at a critical frequency) in the classical evolution. Despite the distinctly differing evolution, the classical and quantum oscillons occur for similar Gaussian initial conditions. This indicated that the Gaussian profiles, at least during the early stage (after that initial transients), evolve largely unaffected by the quantum fluctuations; and those configurations generating oscillons only react to the quantum effects at later times.

The procedure to examine the quantum system employed the Hartree approximation to expand the quantum correlators. This essentially split the field into the classical background and the quantum perturbation to the system with the correlators expanded in these two fields. The resultant correlators of the perturbation higher than second order were then set to vanish. This approximation might, perhaps most evidently, be improved through expanding to higher orders

in the perturbations. An equivalent system in the $1/N$ approximation for the scalar field likewise expanded to higher order in the perturbations may also provide an alternative method to precisely examine the quantum decay of oscillons. These possibilities remain to be examined.

This thesis has also presented the first dynamical simulations to examine tunnelling of the 3rd kind in an idealized laboratory scenario. The system involved two parallel, infinite superconducting-sheets shielding a central region from the uniform magnetic field in the regions to either side. These superconducting sheets formed the classical barrier to the external magnetic field. Incorporating the quantum interaction enabled the field to pair-create fermionic particles. These could cross unhindered through the barrier with their subsequent annihilation (re-)creating the magnetic field inside the shielded region. This tunnelling of the 3rd kind thus increased the transmission through the barrier.

The measurements of the transmitted field in the dynamical simulations remarkably accurately confirmed the simple, analytic estimates. These dynamical results qualitatively reproduced the exponential decrease estimated in the transmission on varying the interaction strength between the barrier and the magnetic field. The tunnelling signal in the transmitted magnetic field, moreover, equalled approximately $2 \cdot 10^{-6}$ per cent of the external field value. This matched the analytic value, within the expected correction factor and matched the qualitative deviation expected through heuristic arguments. The result, thus, provided a reasonable confirmation of this perturbative result.

Completing the simulations using different gauge-fermion couplings (g) offers a further method to test the validity of the analytic calculation. Obtaining the predicted analytic result in the regime where the total transmission tends to a constant value, correspondingly, would further confirm the existence of tunnelling of the 3rd kind.

The repetition of the analysis also, using different lattice sizes, for a fixed physical volume and fixed couplings, may provide a method to estimate the

discretization errors on the lattice. This, correspondingly, may ensure the distinguishing of physical effects in the discrepancies between the numerical results and the simplified, analytic estimates. The detailed examination may further assure the dynamical system accurately encapsulates the quantum tunnelling; and potentially also offers a more precise comparison to experiments, for claiming detection of the tunnelling.

These current results successfully implementing the tunnelling of the 3rd kind, importantly, demonstrate the potential for real-time simulations of quantum systems to produce accurate predictions for testing in the laboratory. The examined tunnelling configuration might most simply be adapted to examine the transmission of electromagnetic waves – this would form a version “light shining through a wall” experiments. A perturbative calculation, in reasonable limits where the system is tractable, predicts this case involves a frequency dependent transmission [98]. The simulations might test the validity of this estimate; and also examine the transmission in regimes where the analytical calculations are unable to provide explicit predictions. Preliminary trials to generate an electromagnetic wave on the lattice with Neumann boundaries have been attempted. The Neumann condition on the z -component of the gauge field, though, disrupt the correct formation of an sinusoidal pulse on the boundaries. Overcoming this numerical difficulty remains a challenge to solve for the practicable simulation of the sinusoidal pulses undergoing tunnelling of the 3rd kind.

These procedures developed for tunnelling, further, offer the potential to examine the quantum hall effect within a (fundamental) field-theoretic framework (for a detailed discussion of this quantum phenomenon, see for instance [100]). This phenomenon occurs in a current restricted to a planar conductor with a strong magnetic field perpendicular to the plane. The resistance in the direction perpendicular both to the direction of the current and to the magnetic field increases stepwise on increasing the magnetic field strength. These step sizes involve the ratio of the electron charge to Planck’s constant either in integer

multiples or a limited set of fractional values. The integer values result essentially through the magnetic field quantizing the electrons into the (quantum-mechanical) Landau levels with the steps in the resistance corresponding to the number of occupied Landau levels in the system. Electron-electron interactions generate the fractional steps in the resistance although this process is much less understood. The dynamical simulations of these systems might provide insight into the field theoretic origin of the integer steps and help further explain the nature of the fractional effect.

Both the scalar-field oscillon and the tunnelling systems demonstrated the application of a statistical ensemble to approximate the quantum two-point functions in the dynamics. This procedure for the bosonic scalar-field involves a single ensemble, constructed analogously to the operator mode expansion but where a Gaussianly-distributed number replaced the ladder operator. The statistical mean of these ordinary numbers in effect replaces the quantum average of the operators in the system. This determines the statistical variance of the ensemble fields may replace the quantum correlators throughout the dynamics. The statistical method likewise involves the statistical ensemble replacing the fermionic correlators in the dynamics, except the fermionic system requires two ensembles differing only in a minus sign. This crucial difference ensures that the statistical variances – on forming the products of fields in the two sets – can reproduce the potentially negative values of the fermion correlators.

The ensemble method offered the possibility to reduce the total field values to evolve on the lattice. This process, in the bosonic case, failed to offer significant gains. The convergence of the scalar-field evolution needed an ensemble size of $M = 60000$. On the square lattice of $N = 256$ point, this was only marginally fewer fields than the $N^2 = 65536$ modes required in the mode function method. The trial case in the fermionic system, similarly, indicated that the method required substantial computational resources and an impracticable real-time for completion.

These applications demonstrate an evident limit in the effectiveness of the ensemble method. The strongly inhomogeneous nature of the oscillon and the results obtained without volume averaging – to potentially reduce the statistical fluctuations – likely were the reasons for requiring a sizeable ensemble. These difficulties likewise potentially also caused the ensemble method to fail in the fermion case. The low dimensionality of the oscillon simulations also likely contributed to the large ensemble-size in comparison to the number of modes. These potential difficulties may therefore indicate that both the dimensionality and whether the results involve volume averaging are important factors in considering the ensemble method for use in future simulations.

Constructing an ansatz for the fields incorporating the symmetries in the system provided an alternative method for simplifying the tunnelling dynamics. This effectively reduced the system to a 1 + 1D problem in the z -direction with the quantum correlators involving a sum also over the x - and y -directions in mode space. This produced a significant decrease in the field values to compute on the lattice, and consequently enabled the evolution of the fermionic system in a practical time.

The ansatz dynamics reliably required less than an hour for each simulation in contrast to the more than six days in computing the trial ensemble case – still using fewer than the necessary fields. This considerable increase in efficiency thus demonstrates the potential power of a suitable ansatz to significantly reduce the computational times in fermion simulations. Using a spherically symmetric form of the fermion spinors [101], for instance, may simplify the dynamics to enable the completion of otherwise impracticable simulations. Devolving the techniques for fermion fields satisfying various symmetries, alongside the advances in computing resources to support larger numbers of fields on the lattice may increasingly enable practicable simulations using the exact mode functions to examine the dynamical evolution of fermions.

Appendix A

Neumann Boundaries: Continuum

The Neumann conditions on the z -boundaries, in the continuum (see Section 5.5.2) constrain both the gradient of the fermion current in the perpendicular directions and also the component parallel to vanish everywhere on these boundaries:

$$i\frac{q}{\hbar}\partial_3\langle T\hat{\Psi}(x)\gamma^{1/2}\hat{\Psi}(x)\rangle\Big|_{x=x_B} = 0, \quad (\text{A.1a})$$

$$i\frac{q}{\hbar}\langle T\hat{\Psi}(x)\gamma^3\hat{\Psi}(x)\rangle\Big|_{x=x_B} = 0, \quad (\text{A.1b})$$

where x_B is a location on these boundaries.

These conditions imply a constraint on the fermion fields on the boundary. In particular, the field at the lower and upper boundaries respectively may be asserted to satisfy a relation of the form

$$\begin{aligned} \Psi(x)\Big|_{x=x_0} &= \lim_{\delta x_3 \rightarrow 0} B_0 \Psi(x + \delta x_3)\Big|_{x=x_0}, \\ \Psi(x + \delta x_3)\Big|_{x=x_N} &= \lim_{\delta x_3 \rightarrow 0} B_N \Psi(x)\Big|_{x=x_N}, \end{aligned} \quad (\text{A.2})$$

where $(x + \delta x_3) \equiv (x_0, x_1, x_2, x_3 + \delta x_3)$, x_0 specifies a coordinate on the lower

boundary, x_N likewise on the upper boundary¹, and $B_{0/N}$ are the matrices to determine.

Substituting these relations into the conjugated spinor in the z -component of the fermions current, at both the upper and lower boundaries, implies

$$i\frac{q}{\hbar}\langle T\hat{\Psi}(x)\gamma^3\hat{\Psi}(x)\rangle\Big|_{x=x_B} = i\frac{q}{\hbar}\lim_{\delta x_3\rightarrow 0}\langle T\hat{\Psi}^\dagger(x+\delta x_3)B_{0/N}^\dagger\gamma^0\gamma^3\hat{\Psi}(x)\rangle\Big|_{x=x_B};$$

likewise, substituting this into the unconjugated spinor in the current yields

$$i\frac{q}{\hbar}\langle T\hat{\Psi}(x)\gamma^3\hat{\Psi}(x)\rangle\Big|_{x=x_B} = i\frac{q}{\hbar}\lim_{\delta x_3\rightarrow 0}\langle T\hat{\Psi}^\dagger(x)\gamma^0\gamma^3B_{0/N}\hat{\Psi}(x+\delta x_3)\rangle\Big|_{x=x_B}.$$

These both evaluated in the limit $\delta x_3 \rightarrow 0$, hence, determine the condition for the z -component to vanish on the boundary may be satisfied if and only if

$$\langle T\hat{\Psi}^\dagger(x)B_{0/N}^\dagger\gamma^0\gamma^3\hat{\Psi}(x)\rangle\Big|_{x=x_B} = -\langle T\hat{\Psi}^\dagger(x)\gamma^0\gamma^3B_{0/N}\hat{\Psi}(x)\rangle\Big|_{x=x_B}.$$

This may be obtained through asserting, in particular

$$B_{0/N}^\dagger\gamma^0\gamma^3 = -\gamma^0\gamma^3B_{0/N}. \quad (\text{A.3})$$

The strict definition of the derivative in the continuum specifies

$$\partial_3 f(x) \equiv \lim_{\delta x_3 \rightarrow 0} \frac{f(x + \delta x_3) - f(x)}{\delta x_3}.$$

Applying this to the Neumann condition (A.1a) in the directions perpendicular to the boundary implies

$$\lim_{\delta x_3 \rightarrow 0} \frac{1}{\delta x_3} \left(\langle T\hat{\Psi}(x + \delta x_3)\gamma^{1/2}\hat{\Psi}(x + \delta x_3)\rangle - \langle T\hat{\Psi}(x)\gamma^{1/2}\hat{\Psi}(x)\rangle \right)\Big|_{x=x_B} = 0.$$

¹The coordinates where $x_3 = -\delta x_3$ may be asserted to form the lower boundary and those coordinates where $x_3 = (N_3 - 1)\Delta x_3$ likewise for the upper boundary. This ensures both the location of these boundaries and the matrix conditions (A.2) on the field match the equivalent constraints, in the continuum limit, imposed on the lattice (see Section 5.5.2, and also the appendix B).

Substituting the boundary-matrix expressions (A.2) into this form of the derivative at the lower and upper boundaries, respectively yields

$$\lim_{\delta x_3 \rightarrow 0} \frac{1}{\delta x_3} \left(\langle T \hat{\Psi}^\dagger(x + \delta x_3) [B_0^\dagger \gamma_0 \gamma^{1/2} B_0 - \gamma_0 \gamma^{1/2}] \hat{\Psi}(x + \delta x_3) \rangle \right) \Big|_{x=x_0} = 0,$$

$$\lim_{\delta x_3 \rightarrow 0} \frac{1}{\delta x_3} \left(\langle T \hat{\Psi}^\dagger(x) [B_0^\dagger \gamma_0 \gamma^{1/2} B_0 - \gamma_0 \gamma^{1/2}] \hat{\Psi}(x) \rangle \right) \Big|_{x=x_N} = 0.$$

These constraints may both be satisfied if

$$B_{0/N}^\dagger \gamma_0 \gamma^{1/2} B_{0/N} = \gamma_0 \gamma^{1/2}. \quad (\text{A.4})$$

This result and the condition (A.3) obtained from the z -component of the current together form the necessary constraints on the boundary matrices to satisfy for implementing the Neumann boundaries on the fermions.

A.1 Solutions to the Neumann Constraint

The γ -matrices, in general, generate the relevant matrix-operations on fermions and thus are expected also to form the matrices $B_{0/N}$. Uniquely among the γ matrices, the relation of the γ^3 to the z -direction matches the distinctive direction in the Neumann conditions. Further, the γ^5 matrix provides a canonical combination of the direction-related γ -matrices but without association to a specific direction. This therefore indicates the boundary matrices may be comprised of any combination of γ^5 and γ^3 matrices.

A possible form incorporating these conditions may be to impose

$$B_{0/N} = \pm \gamma^3. \quad (\text{A.5})$$

Substituting this possibility into the constraints (A.3) and (A.4) on the boundary matrices readily determines this form satisfies the Neumann conditions for the fermions, on the z -boundaries.

The γ^5 matrix might likewise form a comparably simple alternative imposing

$$B_{0/N} = \pm i\gamma^5. \quad (\text{A.6})$$

Again substituting this into the constraints on the boundary matrices determines this form offers an alternative to produce the Neumann conditions for the fermions.

Combining both the γ^5 and γ^3 matrices through multiplication provides a further possible form of the boundary matrices:

$$B_{0/N} = \pm i\gamma^5\gamma^3. \quad (\text{A.7})$$

Substituting the possibility into the boundary constraints likewise confirms this combination also satisfies the Neumann conditions.

A.2 Selecting the Fermion Boundary Condition

The imposed matrix-constraint (A.2) on the boundary (in the limit $\delta x_3 \rightarrow 0$) implies

$$(\mathbb{I}_4 - B_{0/N})\Psi(x)|_{x_B} = 0. \quad (\text{A.8})$$

This in the simplest γ^5 -case (A.6) yields

$$(\mathbb{I}_4 \mp i\gamma^5)\Psi(x)|_{x_B} = 0,$$

where the plus corresponds to the negative option and the minus to the positive. Evaluating this explicitly using the Weyl representation of the γ -matrices (5.2) and specifying the four-component, fermion spinor through the two-component,

up-spinor Ψ_u and down-spinor Ψ_d yields

$$(1 \mp i)\Psi_u(x)|_{x_B} = 0,$$

$$(1 \pm i)\Psi_d(x)|_{x_B} = 0.$$

Each equation may be satisfied only if the spinor equals zero. The simple matrix-constraints hence impose $\Psi(x)|_{x_B} = 0$ and correspondingly the fermion current on the boundary at all times vanishes.

Applying the result (A.8) in the pure γ^3 case (A.5) yields

$$(\mathbb{I}_4 \mp \gamma^3)\Psi(x)|_{x_B} = 0,$$

where the positive and negative possibilities correspondingly produce the minus and plus equalities. Evaluating this using the explicit representation of the matrices and the two-component spinors to form the fermion-field yields

$$\Psi_u(x)|_{x_B} \mp i\sigma^3\Psi_d(x)|_{x_B} = 0,$$

$$\Psi_d(x)|_{x_B} \pm i\sigma^3\Psi_u(x)|_{x_B} = 0. \quad (\text{A.9})$$

These separate equations trivially imply an equivalent constraint on the up and down spinors. Thus, the matrix constraint underdetermines the variables and hence enables an arbitrary, either up or down, two-component spinor. This ultimately (through the constraint on the z -component at the surface to permanently vanish²) supports an arbitrary fermion-current in the x - and y -direction on the boundary.

²Evaluating the current in the z -direction using the explicit forms of the constituent contributions and substituting the derived relation between the up and down components into the resultant expression confirms the consistency of the constraint (A.9) with the initial requirement for the current in this direction to vanish on the boundary.

The relation (A.8) in the combined-matrices case (A.7) implies

$$(\mathbb{I}_4 \mp i\gamma^5\gamma^3)\Psi(x)|_{x_B} = 0,$$

where the plus corresponds to the negative and the minus to the positive option. Again explicitly evaluating the constraint on the two-component spinors yields

$$\Psi_u(x)|_{x_B} \pm \sigma^3\Psi_d(x)|_{x_B} = 0,$$

$$\Psi_d(x)|_{x_B} \pm \sigma^3\Psi_u(x)|_{x_B} = 0.$$

These separate equations trivially imply an equivalent constraint on the up and down spinors and thus underdetermines these variables. This case also, therefore, enables an arbitrary, either up or down, two-component spinor and ultimately (consequent to the initial requirement on the z -component to vanish³) supports an arbitrary fermion-current in the x and y -direction on the boundary.

The weaker constraint in the latter two cases thus enables a very general configuration. This also importantly encompasses the possibility of a fermion current along the x -direction, in reaction to the external-current likewise aligned in the ansatz (see Section 5.2.4). Imposing the simplest γ^5 -constraint creates a significantly stronger constraint on the fermion-current and distinctly stronger than the constraint on the current in the ansatz. Hence, the matrix-relation $B_{0/N} = \gamma^3$ or $B_{0/N} = \pm i\gamma^5\gamma^3$ offer a preferable boundary constraint to implement Neumann-conditions on the z -axis in the continuum. The greater generality in the constituent matrices forming the latter case differentiates the options and provides a slight preference for this case in implementing the Neumann-boundaries for the fermions.

Linear combinations of the matrix-constraints might also satisfy the Neu-

³Explicitly evaluating the current in the z -direction and substituting the derived relation between the up and down components into the expression (as in the pure- γ^3 case) confirms the consistency of the constraint on the fermion field with the initial requirement for the current in this direction to vanish on the boundary.

mann-boundary conditions since the analysis to determine the suitable matrices involves each only operating linearly. Constructing odd powers of the matrix-constraints, also, may individually satisfy the boundary constraints since the square of the $\gamma^{3/5}$ matrices produces the identity. The most general boundary-condition may therefore be obtained in the arbitrary linear combination of the possible constraint matrices and their odd powers⁴. This provides a very complex condition, though; accordingly, the use of the single matrix-term case remains the most convenient choice for implementation of the Neumann-boundaries.

⁴The combined, odd powers of the constraints might in particular create a standard matrix-function defined through the Taylor expansion – for instance, $\sin(\gamma^3)$.

Appendix B

Neumann Boundaries: Discrete

The Neumann conditions on both the fermion current (5.71) and on the Wilson current (5.72) in the discretized system imply a constraint on the fermion fields. Asserting, in particular, the field to satisfy the matrix relations specifying

$$\Psi(X)|_{n_3=-1} = B_0 \Psi(X)|_{n_3=0}, \quad (\text{B.1})$$

$$\Psi(X)|_{n_3=N} = B_N \Psi(X)|_{n_3=N-1}, \quad (\text{B.2})$$

across respectively the upper and lower boundaries in the z -direction, may define the implicit, Neumann condition on the fermions, for the lattice.

These conditions notably match the general, continuum-constraint (A.2) on the fermions, except relating the field at neighbouring points. This discrete case in the continuum limit (where the site separation reduces to zero), moreover, reproduces the equivalent, continuum condition.

The substitution of these lattice boundary constraints into the Neumann conditions (5.71) on the discrete fermion current, and the application of the Neumann constraint (5.70) on the gauge field together determine

$$B_{0/N}^\dagger \gamma^0 \gamma^{1/2} B_{0/N} = \gamma^0 \gamma^{1/2}, \quad B_{0/N}^\dagger \gamma^0 \gamma^3 = -\gamma^0 \gamma^3 B_{0/N}. \quad (\text{B.3})$$

These notably exactly match the constraint on the boundary matrices to satisfy the Neumann conditions in the continuum. The substitution of the field constraints (B.1) for the fermions also into the Neumann conditions (5.72) on the Wilson current, again with the application of the Neumann constraints on the gauge field, implies

$$B_{0/N}^\dagger \gamma^0 B_{0/N} = \gamma^0, \quad B_{0/N}^\dagger \gamma^0 = \gamma^0 B_{0/N}, \quad (\text{B.4})$$

forming the additional constraints on the boundary matrices for the fermions on the lattice.

B.1 Solutions to the Neumann Constraint

Those constraint matrices obtained in the continuum system through considering the symmetry of the boundaries, likewise, offer a potential solutions to the matrix-constraints (B.3) and (B.4) on the lattice. Substituting the three, basic possibilities into the lattice constraints readily determines only the matrix

$$B_{0/N} = \pm i \gamma^5 \gamma^3 \quad (\text{B.5})$$

satisfies all the conditions. This therefore provides the simplest, boundary matrix for the Neumann conditions on the lattice. The matrix constraint in the continuum limit, also notably corresponds to the preferred option in the continuum case (see Section A.2). This confirms the suitability of this basic option in implementing the Neumann conditions on the lattice.

The linearity of the matrix constraints (B.3) and (B.4) in the discrete case implies linear combinations of the simplest solution, equivalently to the continuum, may also satisfy the Neumann-boundary conditions. Any combination, in the continuum, involving purely the $i \gamma^5 \gamma^3$ option, hence, may also consistently provide a valid lattice constraint to satisfy the Neumann conditions. The

increased complexity on imposing these linear combinations in the continuum, though, causes a considerable difficulty in computing the equivalent constraint in the discrete system. Imposing the simplest, matrix, thus, offers the most practical choice for implementing the Neumann-boundaries on the lattice.

Appendix C

Functions of Pauli Matrices

Employing the general properties of the Taylor series to the particular expansion defining the square root of the Pauli matrices – required for forming the fermionic, vacuum mode functions – enables defining this expansion in finite terms, to compute numerically.

A Taylor expansion of a general function $f(x)$ around the point $x = a$ is of the form

$$f(x) = \sum_{n=0}^{\infty} \frac{f^{(n)}(a)}{n!} (x - a)^n;$$

this additionally implies

$$\frac{1}{2} (f(x) + f(-x)) = \sum_{n=0}^{\infty} \frac{f^{(2n)}(a)}{2n!} (x - a)^{2n}, \quad (\text{C.1a})$$

$$\frac{1}{2} (f(x) - f(-x)) = \sum_{n=0}^{\infty} \frac{f^{(2n+1)}(a)}{(2n+1)!} (x - a)^{2n+1}. \quad (\text{C.1b})$$

The square root $\sqrt{\omega_{\mathbf{K}} \mathbb{I}_2 \pm \boldsymbol{\sigma} \cdot \mathbf{K}}$ in the vacuum mode functions is defined through the standard, matrix-function expansion: substituting the square-matrix $\pm \boldsymbol{\sigma} \cdot \mathbf{K}$ into the equivalent Taylor series $(\omega + x)^{\frac{1}{2}}$ around $x = 0$ and promoting the

operations to the matrix equivalent yields

$$\sqrt{\omega_{\mathbf{K}} \mathbb{I}_2 \pm \boldsymbol{\sigma} \cdot \mathbf{K}} = \sum_{n=0}^{\infty} \frac{1}{n!} \left(\frac{d^n}{dx^n} (\omega \pm x)^{\frac{1}{2}} \right) \Big|_{x=0} (\pm \boldsymbol{\sigma} \cdot \mathbf{K})^n.$$

Applying the unitarity of the Pauli matrices and grouping the terms including the Pauli Matrices together and those without hence provides

$$\begin{aligned} \sqrt{\omega_{\mathbf{K}} \mathbb{I}_2 \pm \boldsymbol{\sigma} \cdot \mathbf{K}} &= \sum_{n=0}^{\infty} \frac{1}{(2n)!} \left(\frac{d^{2n}}{dx^{2n}} (\omega + x)^{\frac{1}{2}} \right) \Big|_{x=0} |K|^{2n} \mathbb{I}_2 \\ &\quad \pm \sum_{n=0}^{\infty} \frac{1}{(2n+1)!} \left(\frac{d^{2n+1}}{dx^{2n+1}} (\omega + x)^{\frac{1}{2}} \right) \Big|_{x=0} |K|^{2n+1} \boldsymbol{\sigma} \cdot \hat{\mathbf{K}}, \end{aligned}$$

where $\hat{\mathbf{K}} \equiv \mathbf{K}/|\mathbf{K}|$.

Comparing the first term to the result (C.1a) from the Taylor series and likewise the second to the result (C.1b) hence implies

$$\begin{aligned} \sqrt{\omega_{\mathbf{K}} \mathbb{I}_2 \pm \boldsymbol{\sigma} \cdot \mathbf{K}} &= \frac{1}{2} \left((\omega + |K|)^{\frac{1}{2}} + (\omega - |K|)^{\frac{1}{2}} \right) \mathbb{I}_2 \\ &\quad \pm \frac{1}{2} \left((\omega + |K|)^{\frac{1}{2}} - (\omega - |K|)^{\frac{1}{2}} \right) \boldsymbol{\sigma} \cdot \hat{\mathbf{K}}. \end{aligned}$$

This, thus, provides the expression infinite terms used to generate the fermion, vacuum initial conditions in the numerical simulations.

Bibliography

- [1] Zoltán Dörnyei, “Progressive Creation and the Struggles of Humankind: An Experiment in Canonical Narrative Interpretation”, PhD thesis, University of Durham, 2017.
- [2] Angela Anderson, *Art Draws Out the Beauty of Physics*, 2016, URL: <http://www.symmetrymagazine.org/article/art-draws-out-the-beauty-of-physics> (visited on 03/21/2017).
- [3] *Proms Plus Literary – 17:45 Saturday 31 Aug 2013*, Royal College of Music, 2013, URL: <http://www.bbc.co.uk/events/exdj5v> (visited on 03/21/2017).
- [4] Robert Mann, *An Introduction to Particle Physics and the Standard Model*, CRC Press, 2011, ISBN: 978-1-4398-8760-8.
- [5] Matthew D. Schwartz, *Quantum Field Theory and the Standard Model*, Cambridge University Press, 2014, ISBN: 978-1-107-03473-0.
- [6] Mischa Salle, Jan Smit, and Jeroen C. Vink, “Thermalization in a Hartree Ensemble Approximation to Quantum Field Dynamics”, in: *Physical Review D* 64.2 (2001), [arXiv: hep-ph/0012346].
- [7] Daniel Boyanovsky, Héctor J. de Vega, and Richard Holman, “Erice Lectures on Inflationary Reheating”, in: (1997), URL: <http://arxiv.org/abs/hep-ph/9701304> (visited on 03/21/2017).
- [8] Szabolcs Borsanyi and Mark Hindmarsh, “Semiclassical Decay of Topological Defects”, in: *Physical Review D* 77.4 (2008), [arXiv: 0712.0300 [hep-ph]].
- [9] Daniel Boyanovsky and Héctor J. de Vega, “Quantum Rolling Down out of Equilibrium”, in: *Physical Review D* 47.6 (1993), [arXiv: hep-th/9211044].
- [10] Daniel Boyanovsky, Da-Shin Lee, and Anupam Singh, “Phase Transitions out of Equilibrium: Domain Formation and Growth”, in: *Physical Review D* 48.2 (1993), [arXiv: hep-th/9212083].
- [11] Daniel Boyanovsky et al., “Dissipation via Particle Production in Scalar Field Theories”, in: *Physical Review D* 51.8 (1995), [arXiv: hep-ph/9408214].

-
- [12] Daniel Boyanovsky, Héctor J. de Vega, and Richard Holman, “Can Disordered Chiral Condensates Form? A Dynamical Perspective”, in: *Physical Review D* 51.2 (1995), [arXiv: hep-ph/9401308].
- [13] Anders Tranberg and David J. Weir, “On the Quantum Stability of Q-balls”, in: *Journal of High Energy Physics* 2014.04 (2014), arXiv: 1310.7487.
- [14] Michael C. Cross and Pierre C. Hohenberg, “Pattern Formation Outside of Equilibrium”, in: *Reviews of Modern Physics* 65.3 (1993).
- [15] Nadav M. Shnerb et al., “The Importance of Being Discrete - Life Always Wins on the Surface”, in: *Proceedings of the National Academy of Sciences* 97.19 (2000).
- [16] Tanmay Vachaspati, *Kinks and Domain Walls: An Introduction to Classical and Quantum Solitons (1st Edition)*, Cambridge University Press, 2010, ISBN: 978-05-211-4191-8.
- [17] Sebastian E. Larsson, Subir Sarkar, and Peter L. White, “Evading the Cosmological Domain Wall Problem”, in: *Physical Review D* 55.8 (1997), [arXiv: hep-ph/9608319].
- [18] Theodore Garagounis and Mark Hindmarsh, “Scaling in Numerical Simulations of Domain Walls”, in: *Physical Review D* 68.10 (2003), [arXiv: hep-ph/0212359].
- [19] Marcelo Gleiser and Rafael C. Howell, “Resonant Emergence of Global and Local Spatiotemporal Order in a Nonlinear Field Model”, in: *Physical Review E* 68.6 (2003), [arXiv: hep-ph/0209176].
- [20] Marcelo Gleiser and Rafael C. Howell, “Resonant Nucleation of Spatio-Temporal Order via Parametric Modal Amplification”, in: *Physical Review E* 68 (2003), [arXiv: cond-mat/0310157].
- [21] Marcelo Gleiser and Rafael Howell, “Resonant Nucleation”, in: *Physical Review Letters* 94.15 (2005), [arXiv: hep-ph/0409179].
- [22] Marcelo Gleiser, “Oscillons in Scalar Field Theories: Applications in Higher Dimensions and Inflation”, in: *International Journal of Modern Physics D* 16.02n03 (2007), [arXiv: hep-th/0602187].
- [23] Alexander Vilenkin, “Cosmic Strings and Domain Walls”, in: *Physics Reports* 121.5 (1985).
- [24] Alexander Kusenko, “Solitons in the Supersymmetric Extensions of the Standard Model”, in: *Physics Letters B* 405.1-2 (1997).
- [25] Alexander Kusenko and Mikhail Shaposhnikov, “Supersymmetric Q-balls as Dark Matter”, in: *Physics Letters B* 418 (1998), [arXiv: hep-ph/9709492].

-
- [26] Kari Enqvist and John McDonald, “Q-Balls and Baryogenesis in the MSSM”, in: *Physics Letters B* 425 (1998), [arXiv: hep-ph/9711514].
- [27] Uros Seljak, Ue-Li Pen, and Neil Turok, “Polarization of the Microwave Background in Defect Models”, in: *Physical Review Letters* 79.9 (1997), [arXiv: astro-ph/9704231].
- [28] Michel Remoissenet, *Waves Called Solitons: Concepts and Experiments (2nd Revision and Enlarged Edition)*, Springer, 1996, ISBN: 978-35-406-0502-7.
- [29] Malcolm R. Anderson, *The Mathematical Theory of Cosmic Strings: Cosmic Strings in the Wire Approximation*, CRC Press, 2015, ISBN: 978-1-4200-3336-6.
- [30] Daren Austin, Edmund J. Copeland, and Thomas W. B. Kibble, “Characteristics of Cosmic String Scaling Configurations”, in: *Physical Review D* 51.6 (1994), [arXiv: hep-ph/9406379].
- [31] Mark B. Hindmarsh and Thomas W. B. Kibble, “Cosmic Strings”, in: *Reports on Progress in Physics* 58.5 (1995), [arXiv: hep-ph/9411342].
- [32] Alexander Vilenkin and Edward Paul S. Shellard, *Cosmic Strings and Other Topological Defects*, Cambridge University Press, July 2000, ISBN: 978-0-521-65476-0.
- [33] Sidney Coleman, “Q-balls”, in: *Nuclear Physics B* 262.2 (1985).
- [34] Mitsuo I. Tsumagari, Edmund J. Copeland, and Paul M. Saffin, “Some Stationary Properties of a Q -ball in Arbitrary Space Dimensions”, in: *Physical Review D* 78.6 (2008), [arXiv: 0805.3233 [hep-th]].
- [35] Tsung-Dao. Lee and Yang Pang, “Nontopological Solitons”, in: *Physics Reports* 221.5 (1992).
- [36] Edmund J. Copeland, Marcelo Gleiser, and Hans-Reinhard Müller, “Oscillons: Resonant Configurations During Bubble Collapse”, in: *Physical Review D* 52.4 (1995), [arXiv: hep-ph/9503217].
- [37] Ethan P. Honda and Matthew W. Choptuik, “Fine Structure of Oscillons in the Spherically Symmetric ϕ^4 Klein-Gordon Model”, in: *Physical Review D* 65.8 (2002), [arXiv: hep-ph/0110065].
- [38] Gyula Fodor et al., “Oscillons and Quasi-Breathers in the ϕ^4 Klein-Gordon Model”, in: *Physical Review D* 74.12 (2006), [arXiv: hep-th/0609023].
- [39] Marcelo Gleiser, “Pseudo-Stable Bubbles”, in: *Physical Review D* 49.6 (1994), [arXiv: hep-ph/9308279].
- [40] Marcelo Gleiser, “D-Dimensional Oscillating Scalar Field Lumps and the Dimensionality of Space”, in: *Physics Letters B* 600.1-2 (2004), [arXiv: hep-th/0408221], (visited on 12/29/2015).

-
- [41] Paul M. Saffin and Anders Tranberg, “Oscillons and Quasi-Breathers in D+1 Dimensions”, in: *Journal of High Energy Physics* 2007.01 (2007), [arXiv: hep-th/0610191].
- [42] Erik Alexander Andersen and Anders Tranberg, “Four Results on Φ^4 Oscillons in D+1 dimensions”, in: *Journal of High Energy Physics* 2012.12 (2012), [arXiv: 1210.2227 [hep-ph]].
- [43] Mark Hindmarsh and Petja Salmi, “Numerical Investigations of Oscillons in 2 Dimensions”, in: *Physical Review D* 74.10 (2006), [arXiv: hep-th/0606016].
- [44] Petja Salmi and Mark Hindmarsh, “Radiation and Relaxation of Oscillons”, in: *Physical Review D* 85.8 (2012), [arXiv: 1201.1934 [hep-th]].
- [45] Mark Hindmarsh and Petja Salmi, “Oscillons and Domain Walls”, in: *Physical Review D* 77.10 (2008), [arXiv: 0712.0614 [hep-th]].
- [46] Artur B. Adib, Marcelo Gleiser, and Carlos A. S. Almeida, “Long-Lived Oscillons from Asymmetric Bubbles”, in: *Physical Review D* 66.8 (2002), [arXiv: hep-th/0203072].
- [47] Marcelo Gleiser and Joel Thorarinson, “A Phase Transition in U(1) Configuration Space: Oscillons as Remnants of Vortex-Antivortex Annihilation”, in: *Physical Review D* 76.4 (2007), [arXiv: hep-th/0701294].
- [48] Marcelo Gleiser and Noah Graham, “Transition To Order After Hilltop Inflation”, in: *Physical Review D* 89.8 (2014), [arXiv: 1401.6225].
- [49] Mustafa A. Amin, Richard Easther, and Hal Finkel, “Inflaton Fragmentation and Oscillon Formation in Three Dimensions”, in: *Journal of Cosmology and Astroparticle Physics* 2010.12 (2010), [arXiv: 1009.2505 [astro-ph]].
- [50] Mustafa A. Amin, “Inflaton Fragmentation: Emergence of Pseudo-Stable Inflaton Lumps (Oscillons) after Inflation”, in: (2010), URL: <http://arxiv.org/abs/1006.3075> (visited on 08/26/2014).
- [51] Mustafa A. Amin et al., “Oscillons After Inflation”, in: *Physical Review Letters* 108.24 (2012), [arXiv: 1106.3335 [astro-ph]].
- [52] Marcelo Gleiser and Andrew Sornborger, “Long-Lived Localized Field Configurations in Small Lattices: Application to Oscillons”, in: *Physical Review E* 62.1 (2000), [arXiv: ptt-sol/9909002].
- [53] Edward Farhi et al., “Emergence of Oscillons in an Expanding Background”, in: *Physical Review D* 77.8 (2008), [arXiv: 0712.3034 [hep-th]].
- [54] Marcelo Gleiser and Joel Thorarinson, “A Class of Nonperturbative Configurations in Abelian-Higgs Models: Complexity from Dynamical Symmetry Breaking”, in: *Physical Review D* 79.2 (2009), [arXiv: 0808.0514 [hep-th]].

-
- [55] Edward Farhi et al., “An Oscillon in the SU(2) Gauged Higgs Model”, in: *Physical Review D* 72.10 (2005), arXiv: hep-th/0505273.
- [56] Noah Graham, “An Electroweak Oscillon”, in: *Physical Review Letters* 98.18 (2007).
- [57] Noah Graham, “Numerical Simulation of an Electroweak Oscillon”, in: *Physical Review D* 76.8 (2007), [arXiv: 0706.4125 [hep-th]].
- [58] Evangelos I. Sfakianakis, *Analysis of Oscillons in the SU(2) Gauged Higgs Model*, 2012, URL: <http://arxiv.org/abs/1210.7568> (visited on 03/20/2017).
- [59] Pedro P. Avelino et al., “Cosmic-String-Seeded Structure Formation”, in: *Physical Review Letters* 81.10 (1998), [arXiv: astro-ph/9712008].
- [60] Edmund J. Copeland, Joao Magueijo, and Danièle A. Steer, “Cosmological Parameter Dependence in Local String Theories of Structure Formation”, in: *Physical Review D* 61.6 (2000), [arXiv: astro-ph/9903174].
- [61] Uros Seljak and Anze Slosar, “B Polarization of Cosmic Microwave Background as a Tracer of Strings”, in: *Physical Review D* 74.6 (2006), [arXiv: astro-ph/0604143].
- [62] Neil Bevis et al., “CMB Polarization Power Spectra Contributions from a Network of Cosmic Strings”, in: *Physical Review D* 76.4 (2007), [arXiv: 0704.3800 [astro-ph]].
- [63] Levon Pogosian and Mark Wyman, “B-modes from Cosmic Strings”, in: *Physical Review D* 77.8 (2008), [arXiv: 0711.0747 [astro-ph]].
- [64] Benjamin Shlaer, Alexander Vilenkin, and Abraham Loeb, “Early Structure Formation from Cosmic String Loops”, in: *Journal of Cosmology and Astroparticle Physics* 2012.05 (2012), [arXiv: 1202.1346 [astro-ph]].
- [65] Sidney Coleman, “Fate of the False Vacuum: Semiclassical Theory”, in: *Physical Review D* 15.10 (1977).
- [66] Curtis G. Callan and Sidney Coleman, “Fate of the False Vacuum. II. First Quantum Corrections”, in: *Physical Review D* 16.6 (1977).
- [67] Shuang-Yong Zhou et al., “Gravitational Waves from Oscillon Preheating”, in: *Journal of High Energy Physics* 2013.10 (2013), [arXiv: 1304.6094 [astro-ph]].
- [68] Marcelo Gleiser and David Sicilia, “Analytical Characterization of Oscillon Energy and Lifetime”, in: *Physical Review Letters* 101 (2008), [arXiv: 0804.0791 [hep-th]].
- [69] Marcelo Gleiser and David Sicilia, “A General Theory of Oscillon Dynamics”, in: *Physical Review D* 80.12 (2009), [arXiv: 0910.5922 [hep-th]].
- [70] Mark P. Hertzberg, “Quantum Radiation of Oscillons”, in: *Physical Review D* 82.4 (2010), [arXiv: 1003.3459 [hep-th]].

-
- [71] Gyula Fodor et al., “Radiation of Scalar Oscillons in 2 and 3 Dimensions”, in: *Physics Letters B* 674.4-5 (2009), [arXiv: 0903.0953 [hep-th]].
- [72] Mustafa A. Amin and David Shirokoff, “Flat-Top Oscillons in an Expanding Universe”, in: *Physical Review D* 81.8 (2010), [arXiv: 1002.3380 [astro-ph]].
- [73] Makoto Matsumoto and Takuji Nishimura, “Mersenne Twister: A 623-Dimensionally Equidistributed Uniform Pseudo-Random Number Generator”, in: *ACM Transactions on Modeling and Computer Simulation* 8.1 (1998).
- [74] Paul M. Saffin and Anders Tranberg, “Dynamical Simulations of Electroweak Baryogenesis with Fermions”, in: *Journal of High Energy Physics* 2012.02 (2012), [arXiv: 1111.7136 [hep-ph]].
- [75] Michael E. Peskin and Daniel V. Schröder, *An Introduction to Quantum Field Theory*, Springer Science & Business Media, 1995, ISBN: 978-02-015-0397-5.
- [76] Zong-Gang Mou, “Fermions in Electroweak Baryogenesis”, PhD thesis, University of Nottingham, 2015.
- [77] Paul A. M. Dirac, “The Quantum Theory of the Electron”, in: *Proceedings of the Royal Society of London A: Mathematical, Physical and Engineering Sciences* 117.778 (1928).
- [78] Paul A. M. Dirac, “A Theory of Electrons and Protons”, in: *Proceedings of the Royal Society of London A: Mathematical, Physical and Engineering Sciences* 126.801 (1930).
- [79] Gert Aarts and Jan Smit, “Real-Time Dynamics with Fermions on a Lattice”, in: *Nuclear Physics B* 555.1-2 (1999), [arXiv: hep-ph/9812413].
- [80] Szabolcs Borsanyi and Mark Hindmarsh, “Low-Cost Fermions in Classical Field Simulations”, in: *Physical Review D* 79.6 (2009), [arXiv: 0809.4711 [hep-ph]].
- [81] Paul M. Saffin and Anders Tranberg, “Real-time Fermions for Baryogenesis Simulations”, in: *Journal of High Energy Physics* 2011.07 (2011), [arXiv: 1105.5546 [hep-ph]].
- [82] Kenneth G. Wilson, “Quarks and Strings on a Lattice”, in: *13th International School of Subnuclear Physics: New Phenomena in Subnuclear Physics Erice, Italy, July 11-August 1, 1975* (1975).
- [83] Leonard Susskind, “Lattice Fermions”, in: *Physical Review D* 16.10 (1977).
- [84] Heinz J. Rothe, *Lattice Gauge Theories: An Introduction*, World Scientific, 2005, ISBN: 978-981-256-062-9.
- [85] Paul H. Ginsparg and Kenneth G. Wilson, “A remnant of chiral symmetry on the lattice”, in: *Physical Review D* 25.10 (1982).

-
- [86] Jan Smit, *Introduction to Quantum Fields on a Lattice*, Cambridge University Press, 2002, ISBN: 978-0-521-89051-9.
- [87] Guy Blaylock, *Introduction to High Energy Physics, Lecture Notes*, 2010, URL: <https://www.physics.umass.edu/sites/physics/files/admupld/Tunneling-UMass-12Feb10.pdf> (visited on 03/16/2017).
- [88] George Gamow, “Zur Quantentheorie des Atomkernes”, in: *Zeitschrift für Physik* 51.204 (1928).
- [89] University of Colorado, *Application of Quantum Tunneling: Radioactive Decay, Lecture Notes*, 2011, URL: http://www.colorado.edu/physics/phys2130/phys2130_fa11/lecture_pdfs/pclass35.pdf (visited on 03/16/2017).
- [90] Midlands Physics Alliance Graduate School, *STM-Scanning Tunneling Microscope*, URL: <https://www2.warwick.ac.uk/fac/sci/physics/current/postgraduate/regs/mpags/ex5/techniques/electronic/microscopy/> (visited on 03/16/2017).
- [91] Rino Micheloni, Luca Crippa, and Alessia Marelli, *Inside NAND Flash Memories*, Springer Science & Business Media, 2010, ISBN: 978-90-481-9431-5.
- [92] Maurizio Gasperini, “Axion Production by Electromagnetic Fields”, in: *Physical Review Letters* 59.4 (1987).
- [93] Cecile Robilliard et al., “No Light Shining Through a Wall : New Results from a Photoregeneration Experiment”, in: *Physical Review Letters* 99.19 (2007), [arXiv: 0707.1296 [hep-ex]].
- [94] Markus Ahlers et al., “Light from the Hidden Sector”, in: *Physical Review D* 76.11 (2007), [arXiv: 0706.2836 [hep-ph]].
- [95] Markus Ahlers et al., “Laser Experiments Explore the Hidden Sector”, in: *Physical Review D* 77.9 (2008), [arXiv: 0711.4991 [hep-ph]].
- [96] Simon A. Gardiner et al., “Tunneling of the 3rd Kind: A Test of the Effective Non-locality of Quantum Field Theory”, in: *EPL (Europhysics Letters)* 101.6 (2013), [arXiv: 1204.4802 [quant-ph]].
- [97] Babette Döbrich et al., “Magnetically Amplified Tunneling of the 3rd Kind as a Probe of Minicharged Particles”, in: *Physical Review Letters* 109.13 (2012), [arXiv: 1203.2533 [hep-ph]].
- [98] Holger Gies and Joerg Jaeckel, “Tunneling of the 3rd Kind”, in: *Journal of High Energy Physics* 2009.08 (2009), [arXiv: 0904.0609 [hep-ph]].
- [99] Steven Weinberg, *The Quantum Theory of Fields: Modern Applications, Volume II*, Cambridge University Press, 2013, ISBN: 978-11-396-3247-8.
- [100] David Tong, “Lectures on the Quantum Hall Effect”, in: (2016), URL: <http://arxiv.org/abs/1606.06687> (visited on 03/31/2017).

-
- [101] Paul M. Saffin, “Recrudescence of Massive Fermion Production by Oscillons”, in: (2016), URL: <http://arxiv.org/abs/1612.02014> (visited on 03/29/2017).